INVESTIGATING FRESHWATER LENS GEOMETRY AND GROUNDWATER DYNAMICS ON SHACKLEFORD BANKS, NORTH CAROLINA: IMPLICATIONS FOR FRESHWATER RESOURCES ON BARRIER ISLANDS

By: Jackson W. Rizzolo

May, 2026

Director of Thesis: Matthew Sirianni, PhD

Major Department: Earth, Environment, and Planning

Abstract

Freshwater resources on barrier islands are highly vulnerable to saltwater intrusion (SWI) driven by sea level rise, storm surge, and coastal flooding. This study examines freshwater lens geometry and salinity dynamics on Shackleford Banks, and undeveloped island located in the Cape Lookout National Seashore in North Carolina. Using analytical freshwater lens modeling, groundwater-level and electrical conductivity monitoring, frequency-domain electromagnetic induction (FD-EMI) surveys, and geospatial analysis, this research establishes baseline spatial and temporal patterns of subsurface salinity across geomorphic settings during a one-year observation period. Results indicate that island geomorphology (particularly island width) is the primary control on freshwater lens thickness and storage. Freshwater lenses systematically decrease in thickness from the wide, dune-dominated western portion of the island to the narrow, inlet-adjacent eastern segment. Seasonal precipitation drives short-term groundwater-level variability but does not override geomorphologically controlled spatial variability patterns. FD-EMI surveys reveal persistent organization of near-surface conductivity aligned with geomorphic units: interior dune systems consistently exhibit low conductivity indicative of fresh groundwater, whereas sound-side and ocean-adjacent environments display elevated salinity. Time-series and spectral analyses show that groundwater levels are predominantly recharge-driven, while salinity dynamics reflect localized marine influence near coastal boundaries. These findings support a model where geomorphology establishes a structural framework for freshwater availability, and climatic forcing governs temporal variability within that framework. The study provides a critical baseline for detecting future change under continued sea level rise and demonstrates the value of integrating hydrological and geophysical methods to assess freshwater vulnerability in barrier island systems.

Investigating Freshwater Lens Geometry and Groundwater Dynamics on Shackleford Banks, North Carolina: Implications for Freshwater Resources on Barrier Islands

A Thesis

Presented to the Faculty of the Department of Earth, Environment, and Planning

East Carolina University

in Partial Fulfillment of the Requirements for Degree of

Masters of Geological Sciences

By

Jackson W. Rizzolo

May, 2026

Committee Members

Director – Matt Sirianni, PhD (*Geophysics*)

Member – Mike O'Driscoll, PhD (*Hydrology*)

Member – Hannah Sirianni, PhD (*Geospatial*)

Member – Sean Charles, PhD (*Ecology/Geospatial*)

Acknowledgements

Firstly, I would like to thank my family, without your encouragement and support I would never have made it this far in my academic career. I would like to thank my advisor, Dr. Matthew Sirianni, for his guidance and expertise on this project. I would like to thank my committee members, Dr. Michael O’Driscoll, Dr. Hannah Sirianni, and Dr. Sean Charles, for sharing their valuable input. Finally, I must extend my gratitude to the people who helped along the way: Asher Jacobik, Blake King, Dr. Sue Stuska, Kyleigh Kowalski, Lucia Wall, and ECU Water Corps; from collecting data and installing infrastructure to writing advice, this project wouldn’t have been possible without your assistance.

Table of Contents

List of Tables vii

Table of Figures viii

List of Symbols and Abbreviations xv

1. Introduction 1

2. Study Area 6

2.1. Regional Setting 6

2.2 Examined Transects 8

3. Methodological Background 14

3.1 Hydrological Methods 14

3.1.1 Time-Series Analysis of Groundwater Dynamics 14

3.1.2 Freshwater Lens Geometry and Volume Estimates 15

3.1.3 Sedimentological Controls on Hydraulic Properties 18

3.2 Geophysical Methods 19

3.2.1 Frequency-Domain Electromagnetic Induction 19

3.3 Geospatial and Statistical Methods 20

3.3.1 LiDAR-Derived Topography 20

3.3.2 Non-Parametric and Robust Statistical Approaches 21

3.3.3 High-Precision Elevation Control 22

4. Experimental Setup 23

4.1 Methods Supporting Objective 1: Freshwater Lens Dimensions 23

4.1.1 Groundwater Recharge Estimation 23

4.1.2 Analytical Estimation of Freshwater Lens Geometry 24

4.1.3 Sediment Sampling and Hydraulic Conductivity Estimation 24

4.2 Methods Supporting Objective 2: Spatial Variability of Electrical Conductivity 25

4.2.1 FD-EMI Data Collection 25

4.2.2 Elevation and Geomorphic Attribute Extraction 28

4.2.3 Statistical Integration of Geophysical and Geospatial Data 28

4.3 Methods Supporting Objective 3: Temporal Groundwater Dynamics 29

4.3.1 Hydrological Monitoring 29

4.3.2 Time- and Frequency-Domain Analysis 30

4.4 Summary of Experimental Design 30

5. Results **31**
5.1 Objective 1: Spatial and Temporal Variability of Freshwater Lens Dimensions 31
5.1.1 Precipitation and Climate Context 31
5.1.2 Groundwater Recharge Estimates 35
5.1.3 Sediment Texture and Organic Matter Content 36
5.1.4 Hydraulic Conductivity Estimates 37
5.1.5 Analytical Freshwater Lens Thickness 38
5.1.6 Freshwater Lens Volume 40
5.1.7 Objective 1 Summary 41
5.2 Objective 2: Spatial Variability of Electrical Conductivity Across Geomorphic and Topographic Gradients 41
5.2.1 Spatial and Seasonal Patterns in Apparent Electrical Conductivity 42
5.2.2 Relationships Between ECa and Topographic Gradients 49
5.2.3 Multivariate Controls on Conductivity Patterns 52
5.2.4 Objective 2 Summary 53
5.3 Objective 3: Temporal Dynamics in Groundwater Levels and Salinity 53
5.3.2 Temporal Variability in Electrical Conductivity 57
5.3.3 Comparison of Temporal Dynamics Across Geomorphic Scales 62
5.3.4 Frequency-Domain Analysis of Groundwater and Conductivity Time Series 63
5.3.5 Objective 3 Summary 68
6. Discussion **69**
6.1 Geomorphic Control on Freshwater Storage and Lens Geometry 69
6.2 Validity and Utility of FD-EMI for Mapping Salinity Patterns 70
6.3 Temporal Groundwater Dynamics and Dominant Forcing Mechanisms 71
6.4 Integrated Conceptual Model of Salinity Dynamics 72
6.5 Implications for Sea-Level Rise and Coastal Change 73
6.6 Study Limitations and Future Monitoring Considerations 75
7. Conclusion **77**
References **80**
Appendices **90**
Appendix A). Average ECa reading for each geomorphic unit and season by frequency band. 90

Appendix B). Recharge from RISE, MCR, and MCR-BOTH methods from 07/2024-07/2025 93
Table B2) Recharge from RISE, MCR, and MCR-BOTH methods from 7.23.24-8.12.25 94
Appendix C). Table of samples, median grain size, % organic material if applicable, and K. .95
Appendix D). Induction numbers for the maximum and minimum ECa value of each frequency............97
Appendix E). Seasonal transect FD-EMI data across all frequency bands..............................98

List of Tables

Table 1). Mean, median, standard deviation, skewness, and kurtosis of each numerical variable across all datasets 42

Table 2). Mean temperature corrected ECa by season & geomorphic unit 48

Table 3). Spearman ranked test for continuous variables (elevation, slope, and curvature) for each frequency. 50

Table 4). Kruskal-Wallis H Test Between ECa by frequency band and both Geomorphic Units and season. 50

Table 5). Dunn's Post-Hoc Test on ECa and Geomorphic Unit. 51

Table 6). Robust linear model (Huber loss) coefficients relating ECa to geomorphic, seasonal, and topographic predictors across FD-EMI frequency bands. 53

Table 7). Average Conductivity & Water Level in Wells and Associated Geomorphic Unit. 63

Table 8). Dominant Water Level and Electrical Conductivity Periods in Each Well. 68

Table of Figures

Figure 1). Conceptual model of how sea level rise driven saltwater intrusion destroys freshwater resources on a barrier island. Image from (University of Maryland Center for Environmental Science). 3

Figure 2). Map showing Shackleford Banks, individual study sites are demarcated by red squares. 7

Figure 3). Map of Shackleford Banks with geomorphic units demarcated. Unit boundaries were sourced from Riggs (2015). Individual site locations (Sites 1, 2, and 3) are bounded within black boundaries. 9

Figure 4). Map of Transect 1. Transect 1 is the longest transect located in Site 1 on the eastern side of the island. Wells 1F, 1C, and 1D are proximal to Transect 1and are marked by triangles. The notable surficial water body in this site (Mullet Pond) is marked by a blue circle. 10

Figure 5). Map of examined Transect 2. Transect 2 is located in Site 2 in the middle of the island. Wells 2A, 2B, and 2C are proximal to Transect 2 and are marked by triangles. The notable surficial water body in this site (Ibis Pond) is marked by a blue circle. 11

Figure 6). Map of Transect 3. Transect 3 is the shortest transect located in Site 3 on the western side of the island. Wells 3E, 3C, and 3D are proximal to Transect 3 and are marked by triangles. 12

Figure 7). Simplified illustration of FD-EM data collection process. A) Example of typical FD-EMI data collection procedure following Transect 1 (Photo credit, Matthew Sirianni). B) Conceptual model of FD-EMI function. Figure edited from (Viberg, 2012). 19

Figure 8). Skin depth nomogram used to determine the depth of investigation using average site electrical conductivity and frequency range. Upper and lower bounds of this study are marked by the red lines. Nomogram obtained from Geophex Ltd. (2015) 26

Figure 9). Daily precipitation in millimeters on Shackleford Banks. Precipitation monitoring starts on June 1, 2024, and terminates on December 31, 2025. Readings are taken from the Michael J. Smith Airfield, approximately 4 km to the North of Shackleford Banks. There is a noticeable decrease in precipitation during the late fall and winter months (November - February). Red Bars denote dates of FD-EMI surveys. 32

Figure 10). Verified sea-level readings from Beaufort, NC. Records begin June 2024 and end December 2025. Red bars denote dates of FD-EMI surveys. 32

Figure 11). Sea level records overlain on precipitation records. Black line are relative sea level records from Beaufort, NC and are represented on the left axis. The light blue line is precipitation records, represented on the right axis. Red dots represent dates of FD-EMI surveys. 33

Figure 12). Drought index for Carteret County. Drought monitoring starts June 1, 2024, and terminates December 30, 2025. Drought conditions refer to the severity of the drought with D0 - Abnormally Dry, D1 - Moderate Drought, D2 - Severe Drought, D3 - Extreme Drought, D4 - Exceptional Drought. Area Affected refers to the amount of Carteret County affected by the indicated drought conditions. Black Bars denote dates of FD-EMI surveys. 34

Figure 13). Estimate evapotranspiration measurements from the Pamlico Aquaculture Research laboratory beginning in Jue 2024 and terminating in December 2025. Red bars denote FD-EMI survey dates. 35

Figure 14). Stratigraphic columns of sediments samples taken from monitoring well installation. Stratigraphic columns were collected in a local datum and transformed into NAVD88 using sea level as a common baseline. Refer to Figures 4-6 for well locations. 37

Figure 15). A cross section of Transect 1 including both elevation of examined transects and predicted aquifer shape. The surface of the island has been colored to demarcated geomorphic units. Wells proximal to transect have been marked by arrows and show approximate depth.. ...38

Figure 16). A cross section of Transect 2 including both elevation of examined transects and predicted aquifer shape. The surface of the island has been colored to demarcated geomorphic units. Wells proximal to transect have been marked by arrows and show approximate depth. 39

Figure 17). A cross section of Transect 3 including both elevation of examined transects and predicted aquifer shape. The surface of the island has been colored to demarcated geomorphic units. Wells proximal to transect have been marked by arrows and show approximate depth. 40

Figure 18). FD-EMI results from Transect 1 from the 63030Hz frequency band Winter FD-EMI survey conducted 02/12/2025. 43

Figure 19). FD-EMI results from Transect 1 from the 63030Hz frequency band Spring FD-EMI survey conducted 05/12/2025 43

Figure 20). FD-EMI results from Transect 1 from the 63030Hz frequency band Summer FD-EMI survey conducted 09/01/2025. Survey Transects show distinct changes in ECa readings across different geomorphic units. 44

Figure 21). FD-EMI results from Transect 2 from the 63030Hz frequency band Winter FD-EMI survey conducted 02/12/2025 45

Figure 22). FD-EMI results from Transect 2 from the 63030Hz frequency band Spring FD-EMI survey conducted 05/12/2025. 45

Figure 23). FD-EMI results from Transect 2 from the 63030Hz frequency band Summer FD-EMI survey conducted 09/01/2025. Survey Transects show distinct changes in ECa readings across different geomorphic units. 46

Figure 24). FD-EMI results from Transect 3 from the 63030Hz frequency band Winter FD-EMI survey conducted 02/12/2025. 47

Figure 25).FD-EMI results from Transect 3 from the 63030Hz frequency band Spring FD-EMI survey conducted 05/12/2025. 47

Figure 26). FD-EMI results from Transect 3 from the 63030Hz frequency band. A) Winter FD-EMI survey conducted 02/12/2025. B) Spring FD-EMI survey conducted 05/12/2025. D) Summer FD-EMI survey conducted 09/01/2025. Survey Transects show distinct changes in ECa readings across different geomorphic units. 48

Figure 27). Average groundwater levels of each Well proximal to Transect 1 over the course of the study. Water levels are recorded in meters above sea level in reference to NAVD88. Refer to Figures 4-6 for well locations. 55

Figure 28). Average groundwater levels of each Well proximal to Transect 2 over the course of the study. Water levels are recorded in meters above sea level in reference to NAVD88. Refer to Figures 4-6 for well locations. 56

Figure 29). Average groundwater levels of each Well proximal to Transect 3 over the course of the study. Water levels are recorded in meters above sea level in reference to NAVD88. Refer to Figures 4-6 for well locations. 56

Figure 30). Average specific conductivity measurement (µS/cm) of each well proximal to Transect 1 over the course of the study. Note: The three data series are plotted using separate y-axes with different scales to allow for clearer comparison of trends among wells. Refer to Figures 4-6 for well locations. 58

Figure 31). Average specific conductivity measurement (µS/cm) of each well proximal to Transect 2 over the course of the study. Note: The three data series are plotted using separate y-axes with different scales to allow for clearer comparison of trends among wells. Refer to Figures 4-6 for well locations. 58

Figure 32). Average specific conductivity measurement (µS/cm) of each well proximal to Transect 3 over the course of the study. Note: The three data series are plotted using separate y-axes with different scales to allow for clearer comparison of trends among wells. Refer to Figures 4-6 for well locations. 59

Figure 33). Log of electrical conductivity and water level of an interior (1C) and coastal (1D) wells along Transect 1 during the month of March, 2025. Precipitation during this period (two notable precipitation events) is marked by grey bars. Water level in well 1C was too low to record a conductivity reading until March 10-11, where a precipitation event occurred. Note: The three data series are plotted using separate y-axes with different scales to allow for clearer comparison of trends among wells. Refer to Figures 4-6 for well locations...............................60

Figure 34). Log of electrical conductivity and water level of an interior (2B) and coastal (2C) wells along Transect 2 during the month of March, 2025. Precipitation during this period (two notable precipitation events) is marked by grey bars. Note: The three data series are plotted using separate y-axes with different scales to allow for clearer comparison of trends among wells. Refer to Figures 4-6 for well locations...61

Figure 35). Log of electrical conductivity and water level of an interior (3C) and coastal (3E) wells along Transect 3 during the month of March 2025. Precipitation (mm) during this period (two notable precipitation events) is marked by grey bars. Note: The three data series are plotted using separate y-axes with different scales to allow for clearer comparison of trends among wells. Refer to Figures 4-6 for well locations...62

Figure 36). Results of frequency domain (Fourier) analysis (spectral density vs. period) of water levels from wells located along Transect 1. Refer to Figures 4-6 for well locations....................64

Figure 37). Results of frequency domain (Fourier) analysis (spectral density vs. period) of water levels from wells located along Transect 2. Refer to Figures 4-6 for well locations....................64

Figure 38). Results of frequency domain (Fourier) analysis (spectral density vs. period) of water levels from wells located along Transect 3. Refer to Figures 4-6 for well locations....................65

Figure 39). Results of frequency domain (Fourier) analysis (spectral density vs. period) of conductivity readings from wells located along Transect 1. Refer to Figures 4-6 for well locations..66

Figure 40). Results of frequency domain (Fourier) analysis (spectral density vs. period) of conductivity readings from wells located along Transect 2. Refer to Figures 4-6 for well locations..66

Figure 41). Results of frequency domain (Fourier) analysis (spectral density vs. period) of conductivity readings from wells located along Transect 3. Refer to Figures 4-6 for well locations..67

Figure 42). Conceptual model of the hydrogeology of Shackleford Banks. **A)** A generalized model of the Shackleford Bank's freshwater lens at its widest point. **B)** A generalized model of how sea level rise and coastal erosion will affect freshwater lens thickness and volume at the island's widest point. **C)** A generalized mode of Shackleford Bank's freshwater lens at its narrowest point. **D)** A generalized model of how sea level rise and coastal erosion will affect freshwater lens thickness and volume at its narrowest point..73

Figure 43). Relative sea level change scenarios through the end of the century at Beaufort NC (NOAA, 2017). 74

Figure 44). Modeled shoreline change projections overlayed onto maps of western Shackleford Banks. Figure altered from Thomas (2024)..75

List of Symbols and Abbreviations

Symbol	**Definition**
SWI	Saltwater Intrusion
ρ_s	Density of Saltwater
ρ_f	Density of Freshwater
FD-EMI	Frequency-Domain Electromagnetic Induction
ECa	Apparent Electrical Conductivity
β	Induction number
σ	Recorded electrical conductivity
EC_{25}	Electrical conductivity at 25°C
ECt	Apparent electrical conductivity at temperature t

1. Introduction

Freshwater resources on barrier islands are increasingly vulnerable to salinization because of rising sea levels, increased storm intensity, and more frequent coastal flooding (Masterson, 2014; NOAA, 2022; Fiori, 2022; Mariotti et al., 2022; Cantelon et al., 2024). These low-lying coastal systems typically host thin, precipitation-dependent freshwater lenses that are highly sensitive to changes in sea level, recharge, and storm-driven inundation. As sea levels continue to rise, saltwater intrusion (SWI) poses a growing threat to both human and ecological water demands in barrier island environments worldwide.

Shackleford Banks, a remote barrier island within Cape Lookout National Seashore along the Outer Banks of North Carolina, represents an important case study for examining SWI processes on barrier islands. Unlike many developed barrier islands, Shackleford Banks remains largely undeveloped and supports relatively intact coastal ecosystems, including a well-known population of feral horses managed by the National Park Service (NPS). The Shackleford horses (otherwise known as Banker horses) are a long-established population of feral horses believed to be descendants of Spanish colonial horses that arrived on the island several centuries ago. These horses, along with other island fauna and vegetation communities, depend on shallow freshwater resources such as ponds, seeps, and near-surface groundwater accessed through shallow excavations (“horse-holes”). In recent decades, concerns related to climate change, sea level rise, and increased storm exposure have prompted the NPS to seek improved understanding of the island’s freshwater availability and vulnerability to salinization. However, due to the island’s remote location and limited long-term monitoring infrastructure, there is relatively little historical hydrogeological data available to inform management decisions.

Barrier islands are uniquely susceptible to saltwater intrusion due to their geomorphic, geological, and hydrological characteristics. These systems are typically composed of unconsolidated, sandy sediments with high permeability, allowing rapid exchange between surface water, groundwater, and seawater (Panthi, 2024). Freshwater lenses form within the surficial aquifer as precipitation-derived freshwater floats above denser saline groundwater. The thickness and persistence of these lenses are controlled by island elevation and width, recharge rates, sediment properties, tidal forcing, storm surge, and evapotranspiration (Werner et al., 2013; Housego et al., 2021; Paldor et al., 2022). Disruptions to these controls, such as prolonged drought, increased inundation, storm surge, or sea level rise, can reduce freshwater storage and increase salinity, thereby degrading groundwater quality and ecosystem function.

Saltwater intrusion into barrier island aquifers occurs through both lateral and vertical mechanisms (Figure 1). Lateral intrusion is driven by rising sea levels, which increase hydraulic heads at the coastline and shift the freshwater-saltwater interface landward until a new equilibrium is established (Kooi, 2000). Vertical intrusion occurs during storm surge and overwash events, when saline water infiltrates the land surface and percolates downward into the surficial aquifer. This vertical salinization can compress the freshwater lens from above while lateral intrusion advances from below, producing a “pinch” effect that accelerates freshwater degradation (Cantelon, 2022). In addition to direct saline infiltration during overwash events, storm-driven flooding may promote longer-term salinization through evaporative concentration of surface water remaining in low-relief depressions and shallow ponds following inundation. As floodwaters evaporate, dissolved salts can accumulate in near-surface sediments and subsequently leach downward during later recharge events, contributing to delayed increases in groundwater salinity. These processes are particularly important in low-gradient coastal environments such as eastern

North Carolina, where projected sea level rise (approximately 0.45 to 2.01m by 2100). Rising sea levels, increasing intensity of coastal storms, and increasing storm surge is expected to intensify saltwater intrusion across barrier island systems (NOAA, 2022).

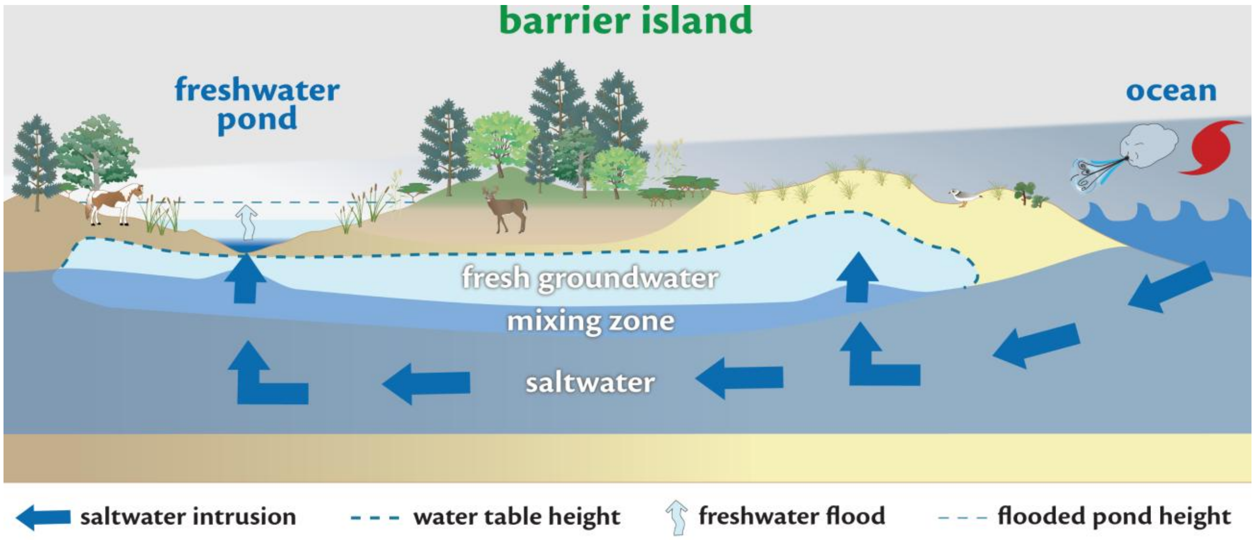

Figure 1). *Conceptual model of how sea level rise driven saltwater intrusion destroys freshwater resources on a barrier island. Image from (University of Maryland Center for Environmental Science).*

Saltwater intrusion has wide-ranging consequences for barrier island ecosystems. Increased groundwater salinity can alter hydrologic regimes, soil chemistry, vegetation composition, and habitat suitability (NOAA, 2017). Even modest changes in sea level and groundwater elevation have been shown to drive substantial shifts in vegetation assemblages and wetland distribution (Agular, 2012; O'Connell, 2012; Masterson, 2014). On Shackleford Banks, degradation of shallow freshwater resources has direct implications for the island's feral horse population, which relies on surface water bodies and shallow groundwater access for drinking water and to sustain freshwater-dependent vegetation that contributes to their forage supply. Continued salinization of these resources could therefore impact both ecological integrity and wildlife management within the park.

Traditional monitoring of saltwater intrusion relies on hydrological and meteorological data collected from monitoring wells, surface water observations, and weather stations. Commonly measured parameters include groundwater and surface water levels, electrical conductivity, precipitation, evapotranspiration, soil moisture, and atmospheric conditions (Hiscock, 2021; Werner et al., 2013). While these measurements provide critical time-series information at discrete locations, they offer limited spatial resolution and may fail to capture heterogeneity across complex barrier island landscapes.

To address this limitation, geophysical methods have increasingly been integrated with hydrological monitoring to characterize subsurface conditions between observation points, particularly in coastal environments (Nielsen, 2009; Parsekian et al., 2015; Cantelon, 2023; Abdelrehim, 2025). Electromagnetic geophysical methods are especially well suited for saltwater intrusion studies due to their sensitivity to bulk electrical conductivity, which serves as a proxy for subsurface salinity (McNeill, 1994; Boaga, 2017). Frequency-domain electromagnetic induction (FD-EMI) methods enable rapid, non-invasive mapping of near-surface conductivity across large areas and have been successfully applied to investigate salinity patterns, freshwater lens structure, and geomorphic controls in barrier island and coastal wetland settings. It is important to note, however, that conductivity responses may also be influenced by factors such as sediment texture, moisture content, and organic material, requiring careful interpretation in conjunction with hydrological and geomorphic data (Parsekian et al., 2015).

This thesis utilizes hydrological monitoring, electromagnetic geophysical surveys, and geospatial analysis to investigate subsurface salinity dynamics on Shackleford Banks over a one-year study period. The primary goal is to establish baseline spatial and temporal patterns in freshwater lens geometry and salinity distribution across contrasting geomorphic settings on an undeveloped barrier island. Specifically, this work addresses the following objectives: **(1)** quantify spatial variability in freshwater lens thickness and volume along representative cross-island transects; **(2)** characterize seasonal and geomorphological patterns in near-surface subsurface electrical conductivity using frequency-domain electromagnetic induction surveys; and **(3)** evaluate temporal groundwater-level and salinity dynamics in relation to precipitation, tidal forcing, and seasonal hydrologic conditions. Together, these analyses provide a foundation for understanding freshwater vulnerability on Shackleford Banks and offer context for future monitoring and management under continued sea level rise.

2. Study Area

2.1. Regional Setting

Shackleford Banks is a barrier island within Cape Lookout National Seashore along the Outer Banks of North Carolina, located in Carteret County near the town of Beaufort (Figure 2). The island is approximately 14.5 km long and ranges in width from ~180 m at its narrowest point to ~1.2 km at its widest. Unlike many Outer Banks barrier islands that trend north-to-south or northeast-to-southwest, Shackleford Banks is oriented northwest-to-southeast. This orientation reduces exposure to high-energy wave conditions originating from the northeast and has influenced the island's long-term geomorphic evolution (Heron, 1984).

Shackleford Banks formed as ridge-and-swale deposits migrated westward from Cape Lookout beginning approximately 2,500 years ago, with subsequent deposition events extending across the modern island roughly 500 years ago (Riggs, 2016). The island remained connected to Cape Lookout until 1933, when a hurricane opened Barden Inlet, permanently separating Shackleford Banks from the mainland barrier system (Susman, 1979). Barden Inlet remains open and continues to influence sediment transport and hydrodynamic conditions along the eastern portion of the island.

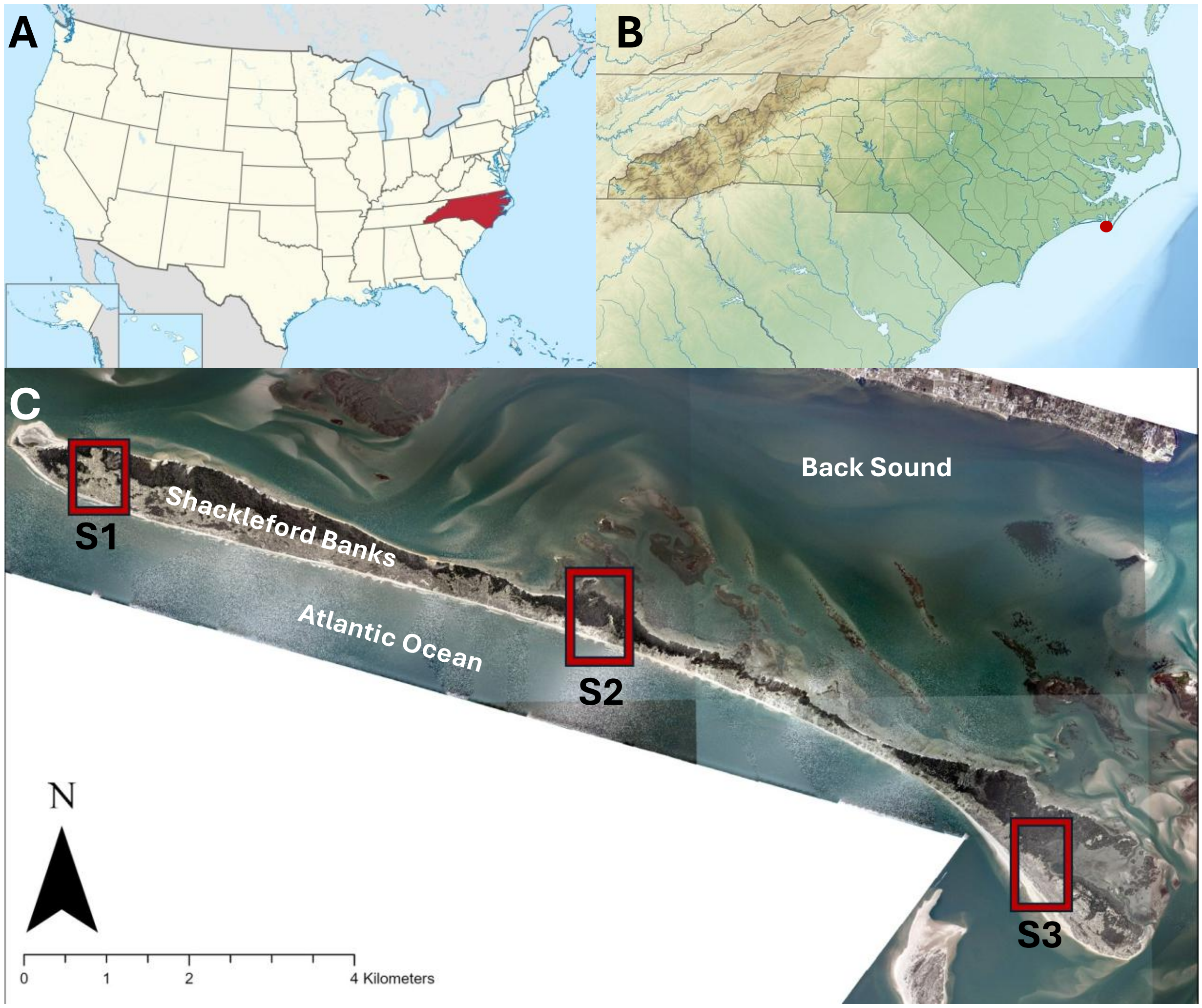

Figure 2). *Map showing Shackleford Banks, individual study sites are demarcated by red squares.*

The island is predominantly wave-dominated (although the sound side of the island is primarily tidally dominated) and characterized by parallel and recurved beach ridges, extensive interior dune fields, back-barrier lagoons partially infilled with salt marsh and tidal flat sediments, and a prominent tidal delta associated with Barden Inlet (Moslow, 1989). Elevation and geomorphic variability are pronounced across the island, with higher-elevation dune systems dominating the western portion reaching a maximum elevation of approximately 11m above sea level. Lower-elevation marsh and tidal environments becoming increasingly prevalent toward the eastern end.

Wetland vegetation communities on Shackleford Banks include freshwater forested and shrub wetlands as well as estuarine and marine wetlands. Two persistent surface freshwater bodies, Mullet Pond and Ibis Pond, are located in the western and central portions of the island, respectively (Figure 4). These ponds represent critical freshwater resources for island wildlife, including the resident feral horse population, which frequently congregates at these locations for drinking water.

Shackleford Banks experiences a humid subtropical climate characterized by warm summers, mild winters, and year-round precipitation. Annual precipitation is on the order of 130-150 cm, distributed seasonally throughout the year but punctuated by episodic high-intensity rainfall associated with tropical systems during the Atlantic hurricane season (June–November) (North Carolina State Climate Office, NC State University, 2024). The local tidal regime is semidiurnal with a typical range of approximately 0.8–1.2 m near Beaufort Inlet, producing regular marine boundary forcing along the island margins (NOAA, 2022). These combined hydroclimatic and tidal conditions strongly influence groundwater recharge, salinity dynamics, and surface-water persistence across the island landscape.

2.2 Examined Transects

To capture spatial variability in geomorphology, vegetation, and hydrologic conditions, the island was divided into three primary study areas corresponding to the western, central, and eastern portions of Shackleford Banks (Sites 1, 2, and 3; Figure 3). These sites were selected in consultation with the National Park Service and through targeted field reconnaissance to represent distinct geomorphic and ecological settings across the island. Each study area encompasses approximately 0.5 km² and includes cross-island transects extending from the sound-side environments toward the ocean-facing shoreline.

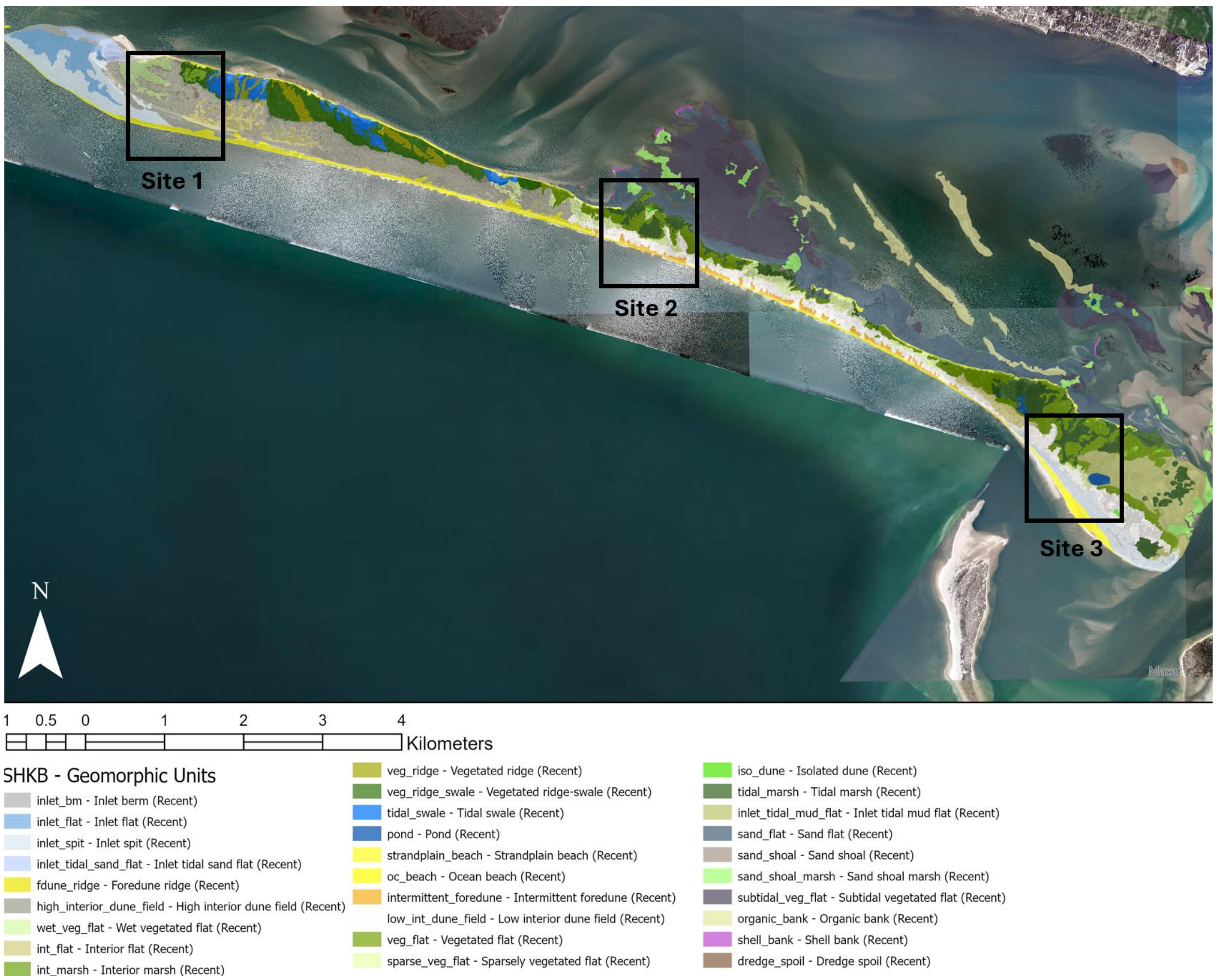

Figure 3). *Map of Shackleford Banks with geomorphic units demarcated. Unit boundaries were sourced from Riggs (2015). Individual site locations (Sites 1, 2, and 3) are bounded within black boundaries.*

Figure 4)*. Map of Transect 1. Transect 1 is the longest transect located in Site 1 on the eastern side of the island. Wells 1F, 1C, and 1D are proximal to Transect 1and are marked by triangles. The notable surficial water body in this site (Mullet Pond) is marked by a blue circle.*

Figure 5)*. Map of examined Transect 2. Transect 2 is located in Site 2 in the middle of the island. Wells 2A, 2B, and 2C are proximal to Transect 2 and are marked by triangles. The notable surficial water body in this site (Ibis Pond) is marked by a blue circle.*

Figure 6). *Map of Transect 3. Transect 3 is the shortest transect located in Site 3 on the western side of the island. Wells 3E, 3C, and 3D are proximal to Transect 3 and are marked by triangles.*

Transect 1 (Figure 4) is located within Site 1 on the western portion of Shackleford Banks. This transect spans wet vegetated flats, high interior dune fields, and the ocean beach geomorphic units defined by Riggs (2015). Vegetation in the wet flats consists primarily of dense shrub-scrub communities, including *Juniperus virginiana* (eastern red cedar), *Spartina patens* (salt meadow hay), and *Smilax* spp. (cat brier). Interior dune fields are dominated by grass species such as *Uniola paniculata* (sea oats) and *Hydrocotyle bonariensis* (pennywort) (Schupp, 2017). Mullet Pond is the primary surface freshwater feature in this area, with intermittent standing water present in interdune depressions following major precipitation events. Groundwater monitoring wells 1F, 1C, and 1D are located proximal to this transect.

Transect 2 (Figure 5), located in the central portion of the island (Site 2), traverses the transitional zone between the higher-elevation dune systems of the western island and the lower-elevation environments toward the east. The transect follows a major NPS-maintained horse trail and intersects vegetated flats, sparsely vegetated flats, isolated dunes, low interior dune fields, intermittent foredunes, and the ocean beach geomorphic units (Riggs, 2015). Vegetation transitions from dense shrub-scrub communities to more sparsely vegetated grass-dominated environments, including *Uniola paniculata* and *Hydrocotyle bonariensis*, interspersed with thickets of *Ilex vomitoria* (yaupon holly), *Myrica cerifera* (bayberry), and *Juniperus virginiana* (Schupp, 2017). Ibis Pond, the largest surface freshwater body on the island, is located near this transect and serves as a significant water source for wildlife. Monitoring wells 2A, 2C, and 2D are situated near Transect 2.

Transect 3 (Figure 6) is located within Site 3 in the eastern portion of Shackleford Banks near Barden Inlet. This transect begins at a known groundwater seep that provides an important freshwater source for horses and extends across inlet tidal mudflats, sparsely vegetated flats, low interior dune fields, the inlet spit, and the ocean beach geomorphic units (Riggs, 2015). Vegetation in this area includes salt-tolerant species such as *Spartina alterniflora* (smooth cordgrass) and *Juncus roemerianus* (black needlerush), transitioning landward to sparse shrub-scrub communities (Schupp, 2017). Groundwater monitoring wells 3E, 3D, and 3C are located adjacent to this transect.

3. Methodological Background

3.1 Hydrological Methods

3.1.1 Time-Series Analysis of Groundwater Dynamics

Time-series analysis is fundamental to understanding hydrologic processes that vary over time, including groundwater level fluctuations, salinity dynamics, and tidal influence. In coastal and barrier island environments, these signals commonly reflect the combined effects of precipitation-driven recharge, evapotranspiration, and marine tidal forcing, which may operate across overlapping temporal scales (E.g. Storms and surge compared to salt-spray).

Hydrometeorological and tidal data used in this study were obtained from monitoring stations proximal to Shackleford Banks. Mean sea level and tidal data was measured from the Duke Marine Research Lab, located approximately 4km to the northwest of the island. Precipitation data was collected from the Michael J. Smith Airfield, located approximately 5 km north of the island. Evapotranspiration data were sourced from the Pamlico Aquaculture Field Laboratory, located approximately 75 km north of the island, representing the closest long-term regional dataset available for this parameter (North Carolina State Climate Office, 2024).

Frequency-domain techniques such as the Fast Fourier Transform (FFT) provide a means of decomposing time-series data into constituent periodic components, enabling identification of dominant cycles associated with tidal, diurnal, or seasonal processes (Sneddon, 1951; Bracewell, 2000). In coastal aquifer studies, FFT-based approaches have been used to evaluate the relative influence of tidal forcing on groundwater levels and salinity, as well as to assess groundwater-surface water interactions (Stringer et al., 2010; Haehnel, 2024). These techniques offer a useful framework for distinguishing short-term marine signals from longer-term recharge-driven trends in groundwater systems.

3.1.2 Freshwater Lens Geometry and Volume Estimates

Freshwater resources on barrier islands are commonly conceptualized as thin freshwater lenses floating above denser saline groundwater within unconfined sandy aquifers. First-order estimates of freshwater lens thickness can be obtained using analytical sharp-interface models that relate freshwater head above sea level to the depth of the freshwater-saltwater interface based on density contrasts (Ghyben, 1888; Herzberg, 1901). The Ghyben-Herzberg equation is defined as:

Eq (1): $$z = \frac{\rho_f}{\rho_s - \rho_f} h$$

Where z is the thickness of the freshwater zone below sea level, h is the thickness of the freshwater zone above sea level, ρ_s is the density of saltwater, and ρ_f is the density of freshwater.

Building on this conceptual foundation, analytical solutions developed by Fetter (1972) incorporate additional controls such as recharge, island width, and hydraulic conductivity to estimate freshwater lens geometry under steady-state conditions. the Fetter (1972) analytical solution (Eq 2) approximates freshwater lens dimensions based on several additional parameters to Eq (1),

Eq (2): $$h^2 = \frac{R(a^2 - x^2)}{K\left\{1 + \left[\frac{\rho_f}{\rho_s - \rho_f}\right]\right\}}$$

Where *R* is average daily recharge to aquifer, K is hydraulic conductivity, *x* is island width, *a* is the half width of the island, *h* is the vertical distance from mean sea level to the saltwater interface, ρ_s is the density of saltwater, and ρ_f is the density of freshwater.

Extensions of these models allow estimation of freshwater lens volume per unit island length, providing a useful metric for comparing freshwater storage capacity across barrier island settings (Chesnaux, 2016). To estimate the total volume of the freshwater lens for a unit length of an island, an additional equation from Chesnaux (2016) can be used. In this equation (Eq 3), V_t is the volume of the lens per unit length of the island at time t, L_t is the half-width of the island at time t, ρ_s is the density of saltwater, ρ_f is the density of freshwater, K is hydraulic conductivity, W is recharge, and n_e is effective porosity.

Eq (3): $$V_t = \left(\frac{\pi n_e}{2}\right)\sqrt{\frac{W}{K}\left(1 + \frac{p_f}{p_s - p_f}\right) * L_t^2}$$

Although these analytical approaches rely on simplifying assumptions, including homogeneous aquifer properties, steady recharge, and a sharp freshwater-saltwater interface (which disregards drivers of salinization such as tides, waves, storms, salt spray). These equations have been widely applied in coastal and island environments to provide first-order estimates of freshwater availability and vulnerability to sea level rise (Chesnaux, 2021; Yan et al., 2024; Kurylyk, 2024). In this study, analytical lens models are used to contextualize observed groundwater salinity patterns and to compare freshwater storage potential across contrasting geomorphic settings on Shackleford Banks.

Recharge represents the volume of water entering the aquifer at the water table and is a critical control on freshwater lens development and persistence (Freeze and Cherry, 1979). In unconfined coastal aquifers, recharge is primarily derived from precipitation and is modulated by evapotranspiration, surface runoff, and groundwater discharge to adjacent marine environments.

Effective porosity values for coarse-to-medium-grained sands typically range from approximately 0.16 to 0.46 based on compilations of unconsolidated sediment hydraulic properties

(Woessner, 2020), and values within this range are consistent with commonly reported effective porosities for intergranular aquifers (Freeze and Cherry, 1979).

The water-table fluctuation (WTF) method provides a widely used framework for estimating recharge by relating observed rises in groundwater level to aquifer storage properties (Healy, 2002; Healy, 2010). Recharge is calculated using the following equation from Healy (2002)

Eq (4): $$R = S_y * \Delta h/\Delta t$$

Where S_y is specific yield, h is the height of the water table, and t is time. Specific yield was estimated from Morris (1967) to be approximately 0.25-0.30 based off of sediment grain size, which was consistently sandy soil across the majority of the study location.

While the WTF approach offers a practical means of estimating recharge from monitoring well data, the resulting recharge estimates may be influenced by uncertainties in concurrent groundwater discharge and drainage processes. To address this limitation, recharge estimates may be adjusted using recession-based approaches that account for water-table decline in the absence of recharge (Nimmo et al., 2015; Eaton, 2020).

In barrier island settings where long-term recharge estimates are scarce, regional studies can provide useful first-order constraints. Previous work in coastal North Carolina suggests that groundwater recharge can be estimated between ~36% and ~70% of annual precipitation in similar geomorphic and hydrogeologic settings (Heath, 1994; Sisco, 2013). In this study, recharge estimation methods are applied to evaluate seasonal and spatial variability in freshwater lens recharge on Shackleford Banks.

3.1.3 Sedimentological Controls on Hydraulic Properties

Sediment texture and composition exert a strong influence on groundwater flow and freshwater lens development by controlling hydraulic conductivity and storage properties. Grain-size distribution provides a fundamental descriptor of sediment permeability and has been widely used to estimate hydraulic conductivity in unconsolidated sandy aquifers (Freeze and Cherry, 1979).

Empirical relationships linking hydraulic conductivity to characteristic grain sizes, such as the Hazen equation, offer a practical means of estimating conductivity where direct hydraulic testing is limited (Hazen, 1892; Devlin, 2015). These approaches are particularly appropriate in barrier island environments dominated by well-sorted sands, where grain-size characteristics fall within the validity range of such empirical formulations. The Hazen equation can be described as

Eq (5): $$K = Ad_{10}^2$$

Where K is hydraulic conductivity in cm/s and A is a coefficient equal to 1.0. The Hazen equation was originally derived for use in uniformly graded sands $(0.01cm < d_{10} < 0.3cm,\ U < 5)$, where U is d_{60}/d_{10} (Devlin, 2015). As the majority of sediments examined on Shackleford Banks fall within this range, the Hazen equation is a sound methodology for this study's purposes.

Organic matter content can further influence hydraulic and geophysical properties by modifying porosity, moisture retention, and electrical conductivity (Rawls, 2004; Friedman, 2005). Loss-on-ignition (LOI) techniques provide a standard method for quantifying sediment organic matter and are commonly used to contextualize variations in hydrologic and geophysical responses across coastal landscapes (Dean, 1974; Heiri et al., 2001).

3.2 Geophysical Methods

3.2.1 Frequency-Domain Electromagnetic Induction

Frequency-domain electromagnetic induction (FD-EMI) is a non-invasive geophysical method widely used to characterize near-surface subsurface electrical conductivity. FD-EMI instruments operate by continuously emitting a time-varying electromagnetic signal that propagates into the subsurface. As shown in Figure 7, when this primary electromagnetic field encounters a subsurface conductor, eddy currents are generated, and a secondary electromagnetic field is produced. This secondary electromagnetic field can be detected by a receiver at the surface and contains information that can be used to derive the apparent conductivity (ECa) of the subsurface when compared to the primary field. (McNeill, 1994; Boaga, 2017).

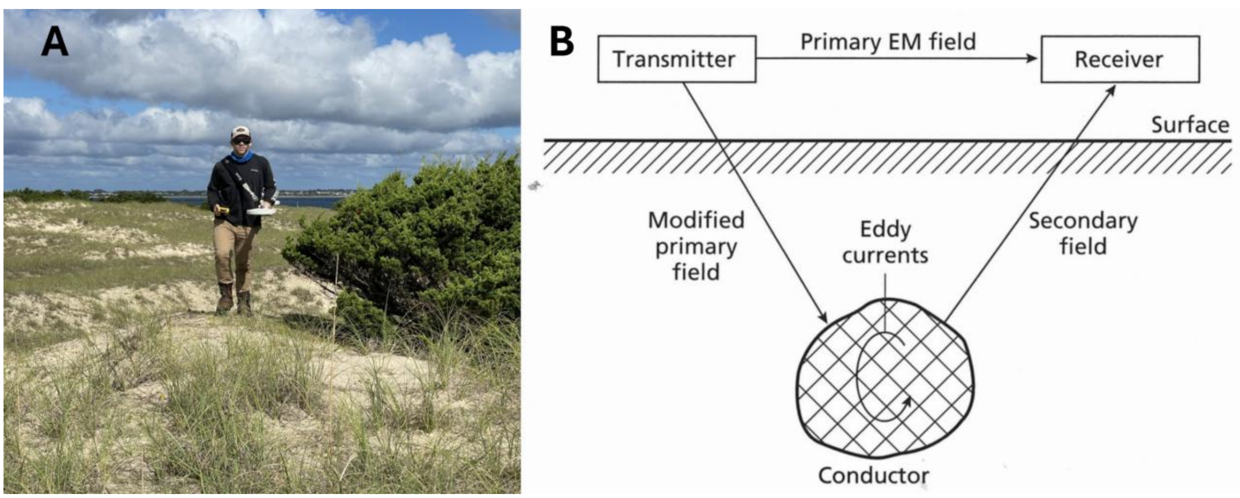

Figure 7). *Simplified illustration of FD-EM data collection process. A) Example of typical FD-EMI data collection procedure following Transect 1 (Photo credit, Matthew Sirianni). B) Conceptual model of FD-EMI function. Figure edited from (Viberg, 2012).*

Raw FD-EMI data from the instrument is collected in the form of apparent electrical conductivity (ECa), the bulk conductivity of the soil profile, and must undergo a series of processing steps to ensure data quality and reliability. In coastal and barrier island environments, ECa variations are commonly associated with changes in pore-water salinity, moisture content, sediment texture, and organic matter. FD-EMI surveys enable rapid spatial characterization of these properties across heterogeneous landscapes, providing coverage between discrete monitoring points. While elevated conductivity often reflects increased salinity, interpretation must account for confounding influences such as soil texture and water content (Corwin, 2005; Parsekian et al., 2015).

Previous studies have successfully applied FD-EMI methods to investigate salinity distribution, freshwater lens structure, and geomorphic controls in barrier island systems (Paine et al., 2005; McKinney et al., 2019; Cantelon et al., 2024). In this study, FD-EMI provides spatial context for groundwater observations and supports interpretation of salinity patterns across contrasting geomorphic environments.

3.3 Geospatial and Statistical Methods

3.3.1 LiDAR-Derived Topography

Light Detection and Ranging (LiDAR) provides high-resolution elevation data critical for analyzing barrier island morphology, freshwater lens geometry, and surface-subsurface hydrologic relationships. Airborne LiDAR datasets enable generation of digital elevation models (DEMs) that capture fine-scale topographic variability across duness, and coastal environments (Brock et al., 2004).

LiDAR-derived elevation products support estimation of island width, surface gradients, and geomorphic features that influence freshwater lens development and vulnerability to saltwater intrusion. Integration of LiDAR with geophysical and hydrological data has proven effective in linking elevation, salinity, and groundwater processes in barrier island settings (Paine et al., 2005; Brock et al. 2004).

3.3.2 Non-Parametric and Robust Statistical Approaches

Environmental and geophysical datasets commonly exhibit non-normal distributions, nonlinear relationships, and extreme values associated with episodic disturbance processes. Apparent electrical conductivity data in coastal environments often display skewness and heavy tails that violate assumptions of parametric statistical methods.

To address these characteristics, non-parametric statistical approaches are well suited for evaluating monotonic and group-wise relationships without imposing distributional assumptions. Rank-based correlation and hypothesis-testing methods provide robust tools for comparing conductivity patterns across geomorphic and vegetation classes.

Spearman rank correlation was used to quantify monotonic associations between ECa and continuous environmental variables (elevation, slope, and curvature). Unlike Pearson correlation, Spearman's ρ does not assume linearity or normality and is robust to skewed distributions and outliers. This makes it appropriate for evaluating the strength and direction of terrain-conductivity relationships across multiple FD-EMI frequency bands with differing effective depths of investigation.

Differences in ECa among categorical geomorphic and vegetation units were assessed using the Kruskal-Wallis test, a rank-based alternative to one-way ANOVA. When statistically significant differences were detected, Dunn's post-hoc tests with multiple-comparison correction were applied to identify pairwise contrasts among geomorphic units. This framework allows for rigorous comparison of conductivity distributions across dune, flat, and coastal environments while accommodating non-normal data.

Robust regression techniques further enable evaluation of relationships between environmental variables while reducing sensitivity to outliers and heteroscedasticity (Huber, 2009;

Maronna et al., 2019). These approaches are particularly valuable for identifying dominant physical controls on salinity and conductivity gradients in heterogeneous coastal landscapes.

3.3.3 High-Precision Elevation Control

Real-time kinematic global navigation satellite systems (RTK-GNSS) provide centimeter-scale positioning accuracy necessary for precise elevation control in low-relief coastal environments (El-Mowafy, 2012). High-accuracy elevation measurements support correlation of groundwater observations, geophysical data, and geomorphic features within a consistent vertical datum. In this study, RTK-GNSS measurements were used to establish consistent vertical control across monitoring wells, geophysical survey transects, and geomorphic units, allowing groundwater-level observations and apparent electrical conductivity data to be compared within a common elevation framework. RTK-GNSS is widely used in coastal and wetland studies to validate remote sensing products and to resolve subtle elevation differences that influence hydrologic processes (Rogers, 2016; Correll, 2019).

4. Experimental Setup

This study utilizes hydrological monitoring, geophysical surveying, and geospatial analysis to address the objectives outlined in Section 1: **(1)** quantify spatial and temporal variability in freshwater lens dimensions, **(2)** characterize spatial patterns in subsurface electrical conductivity across geomorphic and vegetation zones, and **(3)** evaluate temporal groundwater level and salinity dynamics under varying hydrologic forcing.

Field visits were conducted approximately bi-monthly between September 2024 and December 2025. Geophysical surveys and hydrological data downloads were performed during alternating site visits to ensure consistent temporal coverage while minimizing disturbance to monitoring installations.

4.1 Methods Supporting Objective 1: Freshwater Lens Dimensions

4.1.1 Groundwater Recharge Estimation

Recharge was estimated from groundwater level time-series using the Water Table Fluctuation (WTF) method implemented in the open-source Python package GWTFpy (Collenteur, 2025). Fixed-interval groundwater level data were used to derive three recharge estimates: (1) net recharge using the RISE method, (2) gross recharge using a master recession curve applied to rising water-level segments (MRC-Rise), and (3) gross recharge using a master recession curve applied across both rising and falling segments (MRC-Both).

The MRC-Rise approach estimates recharge by comparing observed water-level rises to the expected recession in the absence of recharge. The MRC-Both method evaluates recharge continuously across the full hydrograph, capturing diffuse or sustained recharge during recession periods but with greater sensitivity to recession-curve calibration. Together, these approaches provide a framework for comparing net and gross recharge estimates and evaluating uncertainty associated with recession-curve assumptions, which are known to influence WTF-based recharge calculations in coastal and shallow unconfined aquifers (Hepper, 2005; Crosbie et al., 2005). Applying multiple WTF implementations therefore allows assessment of method sensitivity and produces a more conservative range of recharge estimates rather than relying on a single method.

4.1.2 Analytical Estimation of Freshwater Lens Geometry

Recharge estimates derived from GWTFpy were combined with sedimentological and geomorphic parameters to estimate freshwater lens thickness and volume using analytical sharp-interface models. Freshwater lens geometry was calculated using the formulation of Fetter (1972), which relates freshwater head, recharge, hydraulic conductivity, and island width to interface depth.

Freshwater lens volume per unit island length was estimated following Chesnaux (2016), incorporating recharge, hydraulic conductivity, effective porosity, and island half-width. Island geometry parameters were extracted from LiDAR-derived elevation data. All model inputs were site-specific and evaluated independently for each transect location.

4.1.3 Sediment Sampling and Hydraulic Conductivity Estimation

Sediment samples were collected during monitoring well installation at approximately 0.3-m vertical intervals from the surface to total well depth. Grain-size distributions were determined through dry-sieving following standard sedimentological procedures. Samples exhibiting visible organic enrichment were analyzed using loss-on-ignition to quantify organic matter content.

Hydraulic conductivity was estimated from grain-size data using the Hazen equation, implemented through the HydroGeoSieveXL tool (Devlin, 2015). While grain-size-based estimates may not fully capture aquifer heterogeneity, they provide consistent first-order estimates suitable for analytical freshwater lens modeling in sandy barrier island environments.

4.2 Methods Supporting Objective 2: Spatial Variability of Electrical Conductivity

4.2.1 FD-EMI Data Collection

Frequency-domain electromagnetic induction (FD-EMI) data were collected seasonally (summer, winter, and spring) along each cross-island transect and in the vicinity of monitoring wells using a Geophex GEM-2 instrument. Measurements were acquired at five operating frequencies (450, 1,530, 5,310, 18,220, and 63,030 Hz) with a fixed coil separation of 1.66 m. Surveys were conducted in horizontal coplanar mode with the instrument maintained approximately 1 m above the ground surface, yielding effective depths of investigation ranging from approximately 0.5 to 5 m (Figure 8).

Induction numbers are dimensionless values that describes if the measured EM response is linear with respect to ground conductivity. Calculating induction numbers helps ensure that the survey operated within the low-induction regime ($\beta \ll 1$), where apparent conductivity data are reliable and suitable for interpretation. The induction number is calculated as:

Eq (6): $$\beta = s\sqrt{\frac{(\omega\,\mu\,\sigma)}{2}}$$

where β represents the dimensionless induction number, s is the FD-EMI sensor coil spacing, ω is the angular frequency ($\omega = 2\pi f$), f is the operating frequency in hertz, μ is the magnetic permeability of free space ($4\pi \times 10^{-7}$ H/m), and σ is the recorded electrical conductivity S/m.

Induction numbers calculated for the maximum and minimum apparent conductivity values for each frequency. The results demonstrate that the survey operated primarily within the low-induction number regime (β ≪ 1) (Appendix D). This indicates that the measured electromagnetic response remained approximately linear with respect to subsurface conductivity, supporting the reliability of the apparent conductivity data for hydrogeologic interpretation.

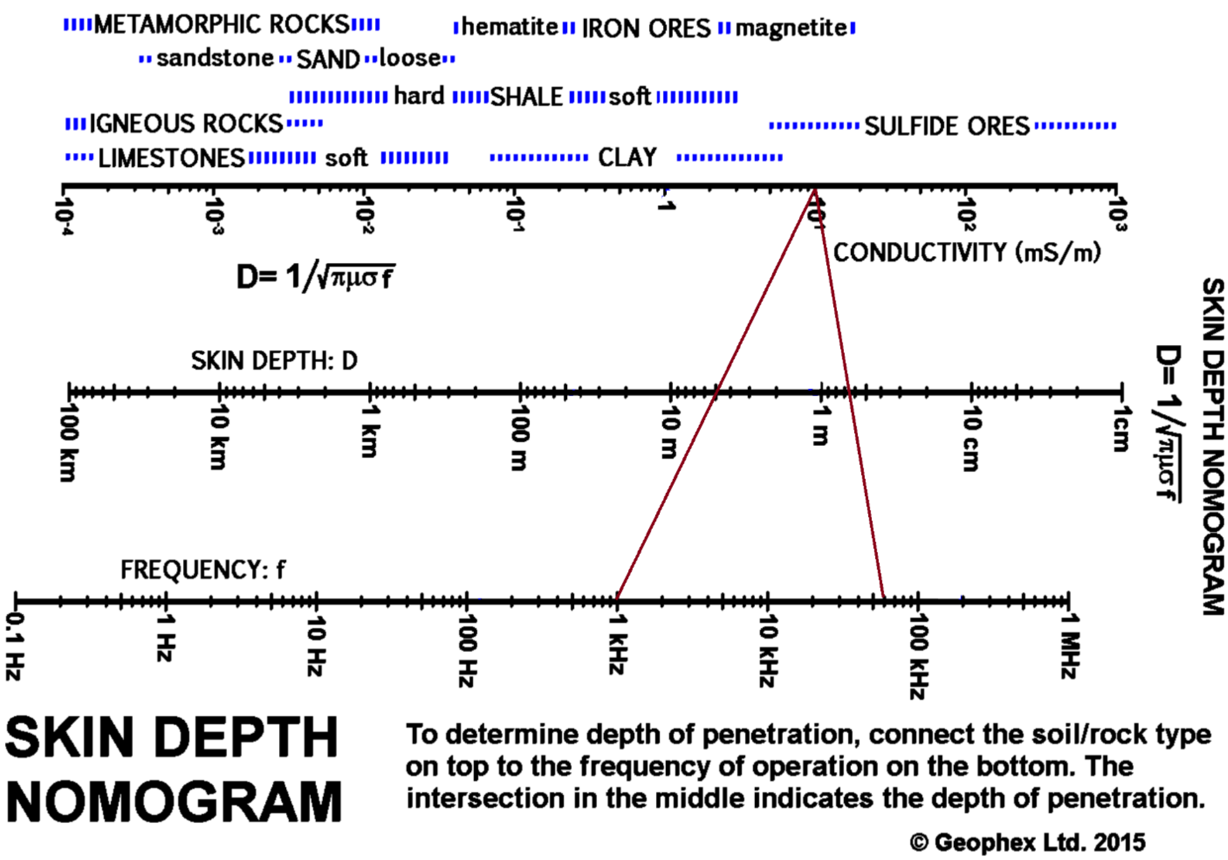

Figure 8). *Skin depth nomogram used to determine the depth of investigation using average site electrical conductivity and frequency range. Upper and lower bounds of this study are marked by the red lines. Nomogram obtained from Geophex Ltd. (2015)*

Duplicate transects were collected in opposing directions during each survey to assess data consistency. At monitoring well locations, two 20-m orthogonal transects intersecting at the well were surveyed to capture localized conductivity variability. Apparent electrical conductivity (ECa) values were temperature-corrected and georeferenced prior to analysis.

Temperature correction (to remove temperature influencing conductivity results) was conducted using the methodology described in Corwin (2005), which offers the following temperature correction equation derived from U.S. Salinity Laboratory (1954):

EQ (7): $$EC_{25} = f_t * EC_t$$

Where EC_{25} is the electrical conductivity at 25°C, f_t is the temperature correction factor for temperature t, and EC_t is the apparent electrical conductivity at temperature t. The temperature correction factor is calculated using an equation derived from Sheets and Hendrickx (1995):

Eq (8): $$f_t = 0.04470 + 1.4034e^{-t/26.815}$$

Where t is the ground temperature when the conductivity data was collected.

This methodology has been used in several previous studies. For example, Paine et al (2005) investigated a barrier island (Mustang Island, Texas) and combined ground-based FD-EMI measurements of apparent conductivity with LiDAR and vegetation surveys along transects, linking ECa with salinity, geomorphology, and hydrologic regime in a barrier island environment. Another example is McKinney et al (2019) where FD-EMI was used to rapidly map apparent conductivity of salt-marsh sediments, cataloging changes in salinization over time. These studies show the efficacy of using FD-EMI to quickly and accurately examine shallow apparent conductivity across large areas, enabling efficient mapping of spatial salinity variability and temporal change, and supporting interpretation of relationships between groundwater observations, geomorphic units, and hydrologic forcing in dynamic barrier-island environments.

4.2.2 Elevation and Geomorphic Attribute Extraction

Elevation data for each transect were obtained from LiDAR-derived digital elevation models sourced from NC OneMap. The most recent dataset (April 2023) has a horizontal resolution of 0.9 m and a vertical accuracy of approximately 0.1 m (95% confidence). The DEM was derived from LiDAR collected by the NC Floodplain Mapping Program and processed by NC Department of Public Safety - Division of Emergency Management (NC OneMap, 2019).. Elevation values were converted to the NAVD88 vertical datum using VDatum (Office of Coast Survey, 2025).

Geomorphic classifications were assigned using the barrier island geomorphic map developed by Riggs (2015). Elevation, slope, curvature, island width, and vegetation class were extracted along transects to support spatial comparison with FD-EMI measurements.

4.2.3 Statistical Integration of Geophysical and Geospatial Data

FD-EMI data were aggregated to raster grids matching the spatial resolution of the LiDAR-derived DEM. Mean ECa values were calculated within each raster cell for each frequency band and spatially aligned with elevation-derived terrain metrics.

Relationships between ECa and continuous topographic variables (elevation, slope, curvature) were evaluated using Spearman rank correlation to accommodate non-normal distributions and nonlinear relationships. Differences in ECa among geomorphic and vegetation classes were assessed using Kruskal-Wallis tests, followed by Dunn’s post-hoc comparisons where statistically significant differences were detected.

Robust regression analysis was applied to evaluate multivariate relationships among ECa, elevation, geomorphic class, and seasonal timing. These analyses enabled identification of dominant environmental gradients (such as transitions from high-elevation dune ridges with low conductivity to low-lying swales with elevated ECa values) controlling subsurface conductivity patterns across the island.

4.3 Methods Supporting Objective 3: Temporal Groundwater Dynamics

4.3.1 Hydrological Monitoring

Groundwater level and electrical conductivity time-series were collected from 9 monitoring wells located near Transects 1-3 using Onset HOBO pressure and conductivity loggers recording at 15-minute intervals. Monitoring wells were constructed from 1.75in diameter PVC pipe with a screened interval covering the bottom 3ft of the well. Wells were constructed so the entirety of the screened interval was below the water table, resulting in well depths ranging from approximately 3ft to 10ft below the land's surface. A bentonite seal was installed at the of each well, to prevent surficial runoff from entering the well. Loggers were suspended at the base of each well and corrected for atmospheric pressure using a co-located barometric pressure logger. Water levels were referenced to NAVD88 using RTK-GNSS surveyed wellhead elevations.

Manual water-level and conductivity measurements were collected during each site visit using handheld meters to validate logger performance and correct for instrument drift. Freshwater conditions were defined as electrical conductivity <2,000 µS/cm, seawater conditions as approximately >55,000 µS/cm, and intermediate values classified as brackish.

Hydrometeorological and tidal data including precipitation, temperature, humidity, and atmospheric pressure were obtained from the North Carolina State Climate Office's Cardinal Data Retrieval System (North Carolina State Climate Office, 2024). These data supported interpretation of groundwater responses to recharge and marine forcing.

4.3.2 Time- and Frequency-Domain Analysis

Time-domain analyses were used to identify long-term trends in groundwater level and conductivity. Frequency-domain analyses were conducted using Fast Fourier Transforms (FFT) to isolate dominant periodicities associated with tidal, diurnal, and seasonal signals. These analyses enabled evaluation of temporal drivers influencing groundwater behavior across contrasting geomorphic settings.

4.4 Summary of Experimental Design

The experimental framework utilizes hydrological monitoring, geophysical surveying, and geospatial analysis to characterize both spatial heterogeneity and temporal variability in subsurface salinity and freshwater lens structure on Shackleford Banks. By combining site-specific field measurements with analytical modeling and statistical analysis, this approach supports multi-scale evaluation of the controls governing freshwater availability and vulnerability in an undeveloped barrier island system.

5. Results

5.1 Objective 1: Spatial and Temporal Variability of Freshwater Lens Dimensions

This objective evaluates the size, thickness, and volumetric capacity of the freshwater lens on Shackleford Banks using precipitation records, groundwater recharge estimates, sedimentological properties, and analytical freshwater lens models. Results are presented to highlight spatial contrasts across the island and the relative influence of seasonal recharge variability.

5.1.1 Precipitation and Climate Context

During the monitoring period (July 2024–August 2025), Shackleford Banks received approximately 1.46 m of precipitation, with pronounced seasonal variability (Figure 9). Fall accounted for the largest share of annual precipitation (0.48 m), followed by summer (0.41 m), spring (0.34 m), and winter (0.13 m). Two major precipitation events dominated the record: 1) a storm associated with Potential Tropical Cyclone #8 in September 2024 and 2) a strong early spring storm in March 2025 (Figure 9). Sea level played an important role in understanding salinization characteristics of Shackleford Banks. Sea level was at its peak in late summer (averaging approximately 1m) and early fall and lowest during winter months (averaging approximately 0.6m) (Figure 10). These peaks correspond to large precipitation events where high winds drive high relative sea levels and storm surge (Figure 11).

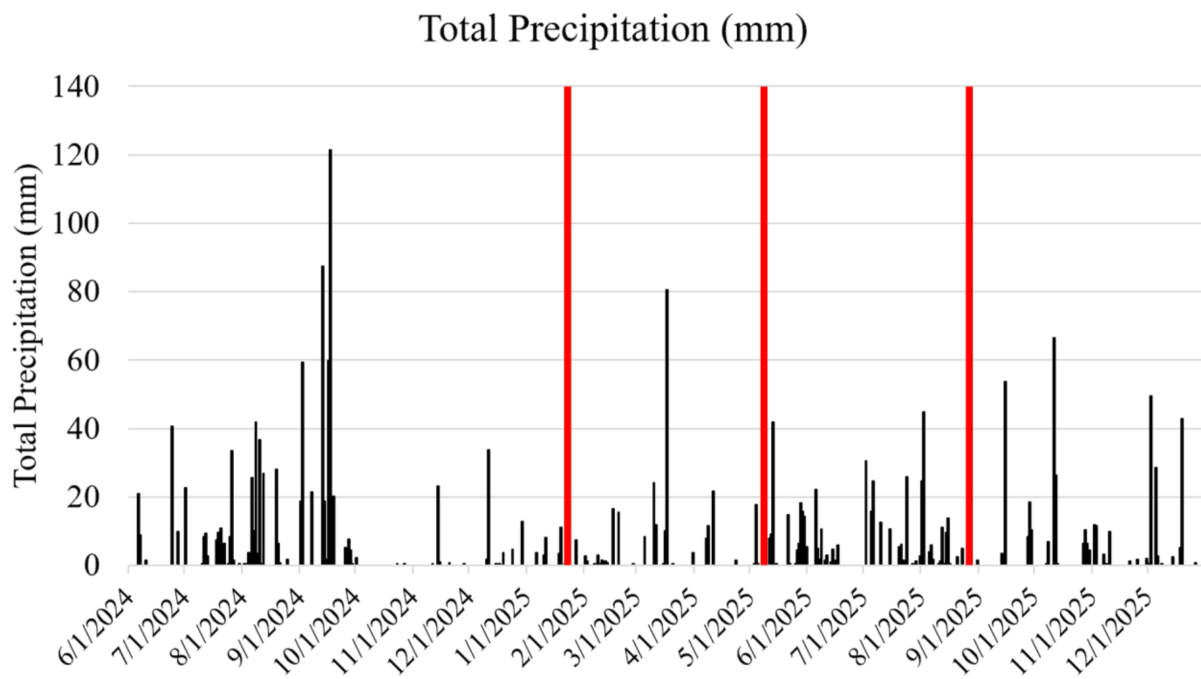

Figure 9). *Daily precipitation in millimeters on Shackleford Banks. Precipitation monitoring starts on June 1, 2024, and terminates on December 31, 2025. Readings are taken from the Michael J. Smith Airfield, approximately 4 km to the North of Shackleford Banks. There is a noticeable decrease in precipitation during the late fall and winter months (November - February). Red Bars denote dates of FD-EMI surveys.*

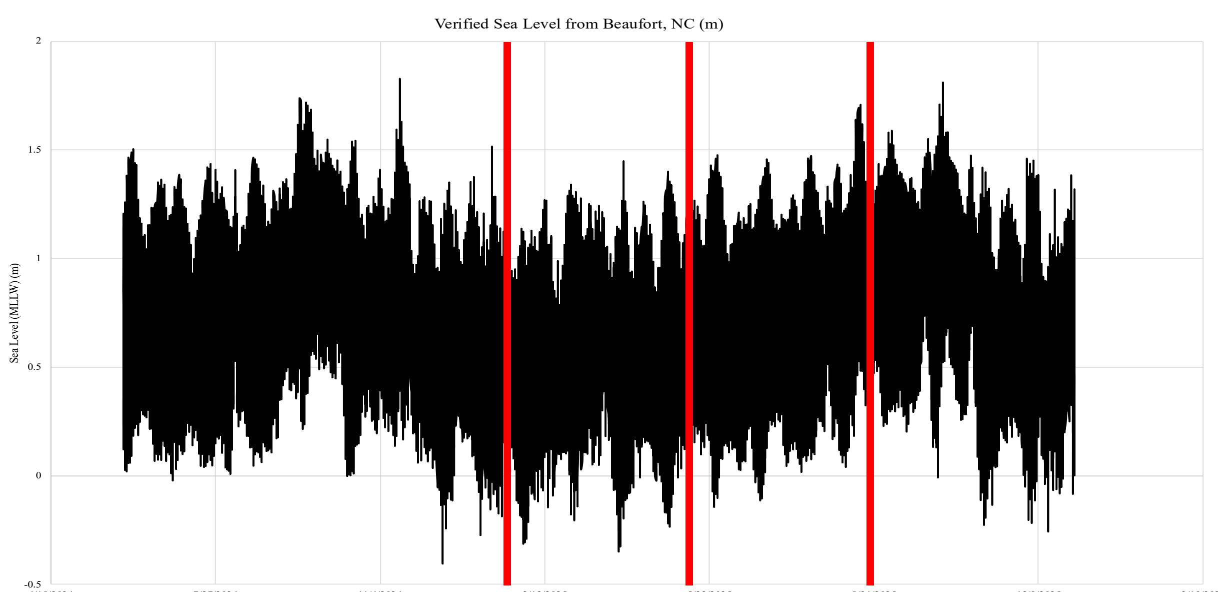

Figure 10). *Verified sea-level readings from Beaufort, NC. Records begin June 2024 and end December 2025. Red bars denote dates of FD-EMI surveys.*

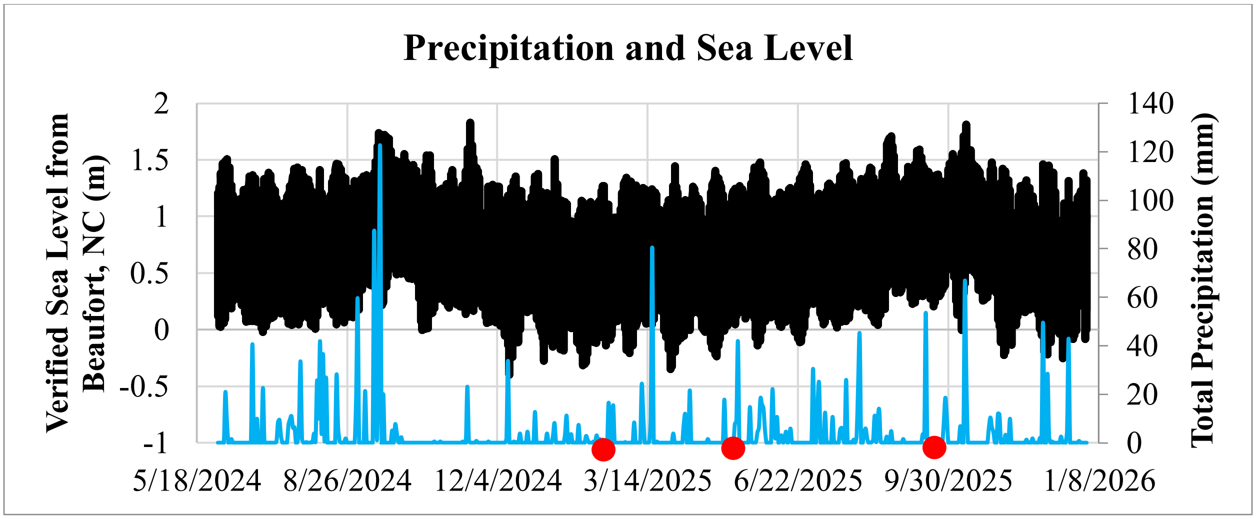

Figure 11). *Sea level records overlain on precipitation records. Black line are relative sea level records from Beaufort, NC and are represented on the left axis. The light blue line is precipitation records, represented on the right axis. Red dots represent dates of FD-EMI surveys.*

Winter 2024-2025 coincided with moderate to severe drought conditions across Carteret County (D1-D2 classification), persisting into early spring before abating in April (Figure 12). These conditions provide important context for interpreting groundwater recharge efficiency and seasonal freshwater lens response.

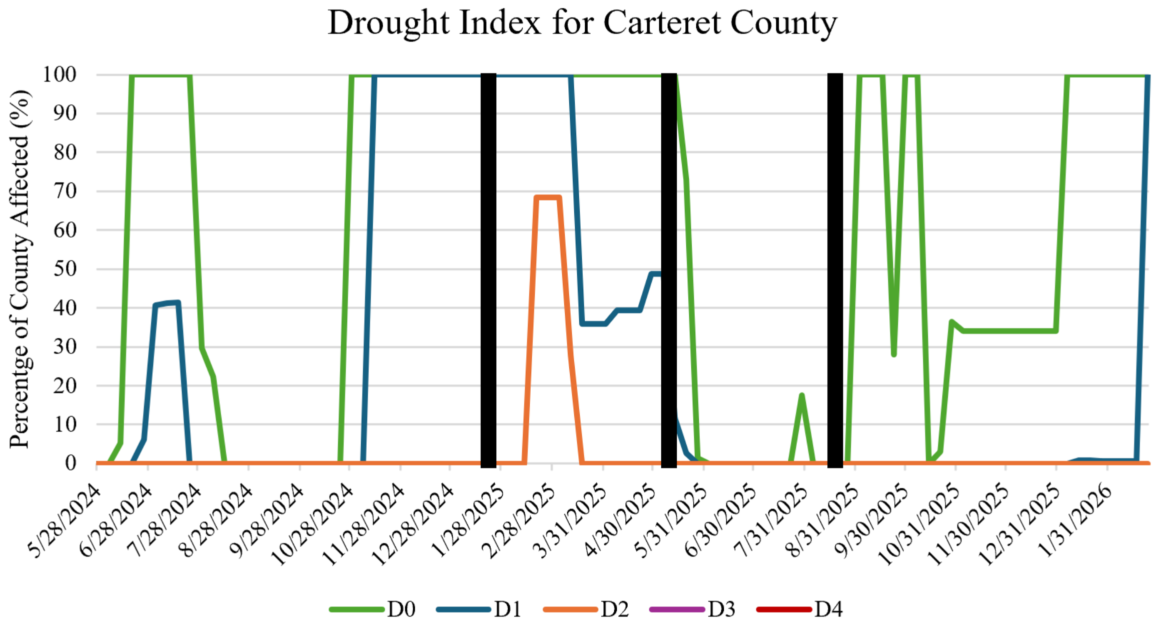

Figure 12). *Drought index for Carteret County. Drought monitoring starts June 1, 2024, and terminates December 30, 2025. Drought conditions refer to the severity of the drought with D0 - Abnormally Dry, D1 - Moderate Drought, D2 - Severe Drought, D3 - Extreme Drought, D4 - Exceptional Drought. Area Affected refers to the amount of Carteret County affected by the indicated drought conditions. Black Bars denote dates of FD-EMI surveys.*

Evapotranspiration (ET) records showed strong seasonal differences across the study period. ET was highest during summer months, peaking at approximately during June of 2024 and 2025. Winter months saw the lowest ET measurements, with the lowest records occurring during late December and Early January (Figure 13).

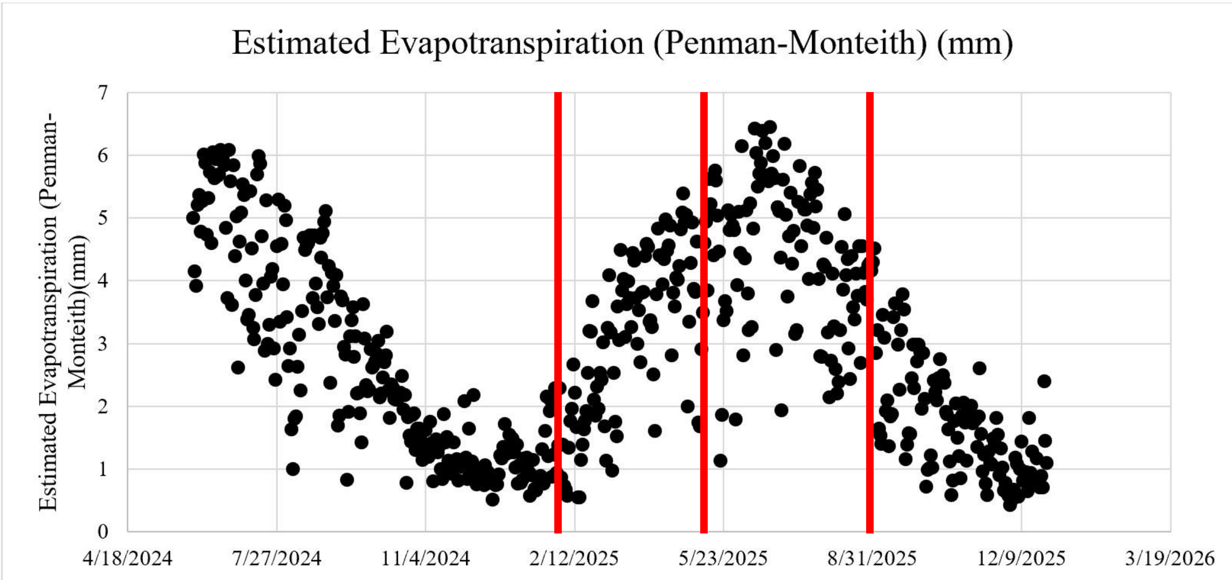

Figure 13). *Estimate evapotranspiration measurements from the Pamlico Aquaculture Research laboratory beginning in Jue 2024 and terminating in December 2025. Red bars denote FD-EMI survey dates.*

5.1.2 Groundwater Recharge Estimates

Recharge estimates derived using the RISE, MRC-Rise, and MRC-Both methods show consistent spatial patterns across all sites, despite differences in absolute magnitude among methods (Appendix B). Across all recharge estimation approaches: Site 1) consistently exhibited the lowest recharge efficiency, with recharge comprising 34–40% of precipitation; Site 2) exhibited the highest recharge efficiency, with recharge accounting for approximately 59–66% of precipitation; and Site 3) showed intermediate recharge, representing 52–58% of precipitation. All values except for the RISE estimation for stie 1 (34%) fall within the 36-70% range estimated in similar geomorphic and hydrogeologic settings (Heath, 1994; Sisco, 2013).

Applying the percentage of precipitation as recharge estimates to the collected precipitation data, it is estimated that the island receives between 49.6cm/yr and 96.3cm/yr of recharge across the island. These results exceed estimates for coastal sandy settings, estimated in Heath (1994) to be 32 cm/yr and in Mew et al. (2002) to be 26 cm/yr. This discrepancy is likely due to a lack of infrastructure and vegetation on the island when compared to other coastal regions encouraging recharge.

Although absolute recharge values varied by method, the relative ranking among sites was preserved, indicating that spatial variability in recharge efficiency is robust to methodological choice. Seasonal precipitation variability modulated recharge magnitude but did not alter the spatial hierarchy among sites.

5.1.3 Sediment Texture and Organic Matter Content

Sediment samples collected during monitoring well installation indicate that subsurface materials across Shackleford Banks are dominated by well-sorted sands, with average grain sizes ranging between 1.4 and 2.1 phi (Appendix C). A subtle coarsening trend is observed from west to east, with the coarsest sediments occurring at Well 3D, where average grain size approaches 0.8 phi (Figure 14).

Organic matter content ranged from approximately 1–13%, with the highest concentrations observed at Site 1, particularly in shallow samples from Wells 1B and 1E. Organic content generally decreased with depth across all sites, with the exception of a localized peat layer intercepted at approximately 3.5 ft depth in Well 1B located near well 1C at Site 1 (Appendix C). Sites 2 and 3 exhibited consistently lower organic matter content, averaging 1.2% and 2.3%, respectively.

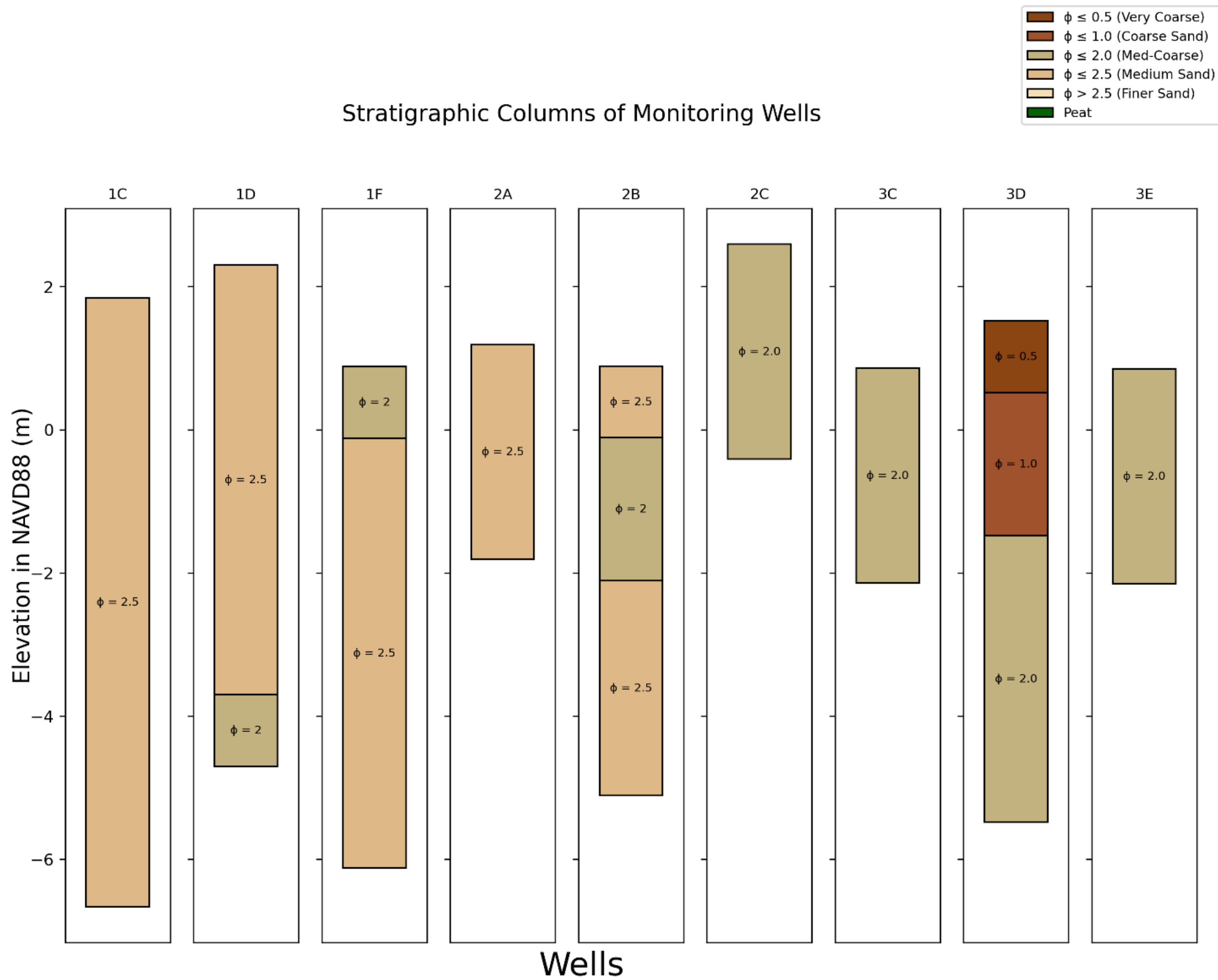

Figure 14). *Stratigraphic columns of sediments samples taken from monitoring well installation. Stratigraphic columns were collected in a local datum and transformed into NAVD88 using sea level as a common baseline. Refer to Figures 4-6 for well locations.*

5.1.4 Hydraulic Conductivity Estimates

Hydraulic conductivity estimates derived from grain-size data range from approximately 3.0×10^{-2} to 1.2×10^{-1} cm/s across all samples (Appendix C) which fall in the range reported for well sorted sands (Fetter, 2001). The highest conductivity values were associated with ocean-facing dune environments, particularly at Wells 1D, 2C, and 3D. The estimated specific yield for the island sediments is approximately 0.32, consistent with prior studies of sandy coastal aquifers (Morris and Johnson, 1967).

5.1.5 Analytical Freshwater Lens Thickness

Analytical modeling indicates a systematic decrease in freshwater lens thickness from west to east across Shackleford Banks (Figures 15–17). The thickest freshwater lens was modeled at Site 1, where maximum lens thickness reached approximately 14 m near Well 1C (Figure 15). At this site, the water table was generally positioned 0–0.5 m above mean sea level, corresponding to depths of 1.5–4 m below the land surface, depending on local topography.

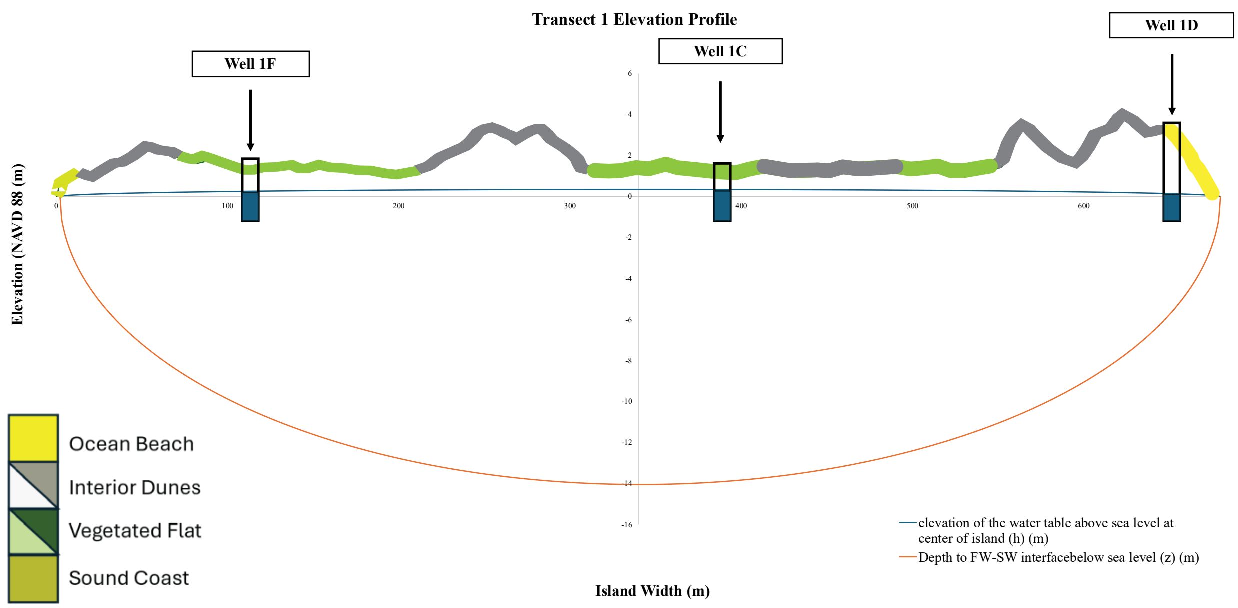

Figure 15). *A cross section of Transect 1 including both elevation of examined transects and predicted aquifer shape. The surface of the island has been colored to demarcated geomorphic units. Wells proximal to transect have been marked by arrows and show approximate depth..*

At Site 2, maximum freshwater lens thickness decreased to approximately 11.7 m (Figure 16). The relatively flat topography along this transect (ranging from -0.09m to 1.3m above sea level) resulted in shallow water-table depths, typically 0–2 m below the surface, with portions of the modeled water table intersecting the land surface near the center of the transect.

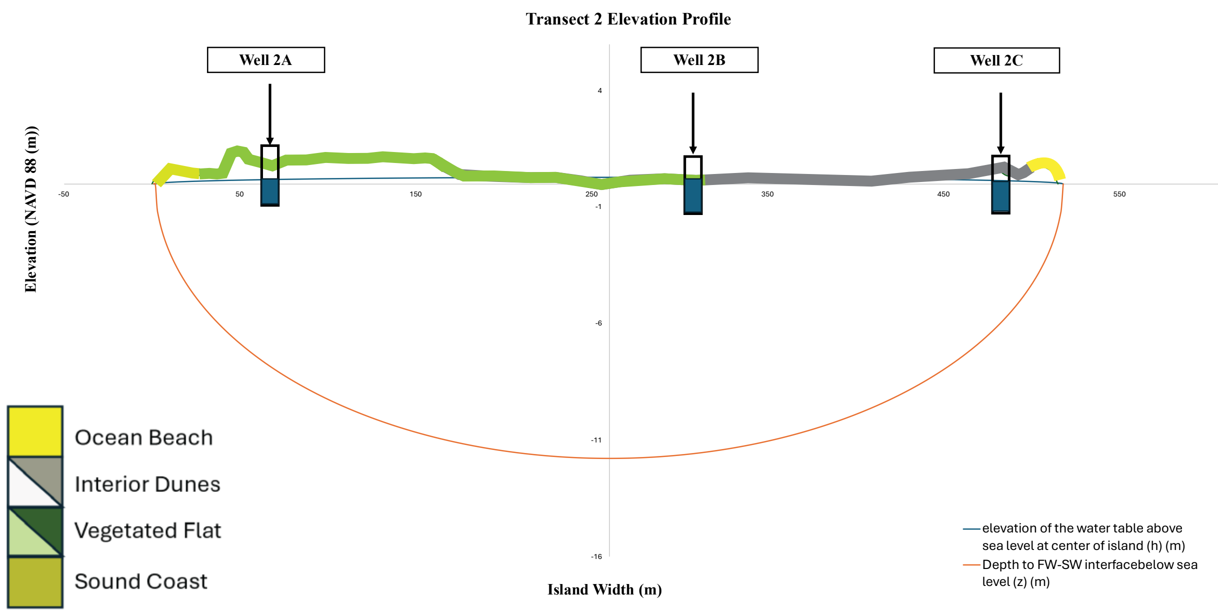

Figure 16). *A cross section of Transect 2 including both elevation of examined transects and predicted aquifer shape. The surface of the island has been colored to demarcated geomorphic units. Wells proximal to transect have been marked by arrows and show approximate depth.*

The thinnest freshwater lens occurred at Site 3, where maximum thickness was approximately 8 m (Figure 17). Water-table depths ranged from 0.5–4 m below the surface, reflecting reduced island width and proximity to Barden Inlet.

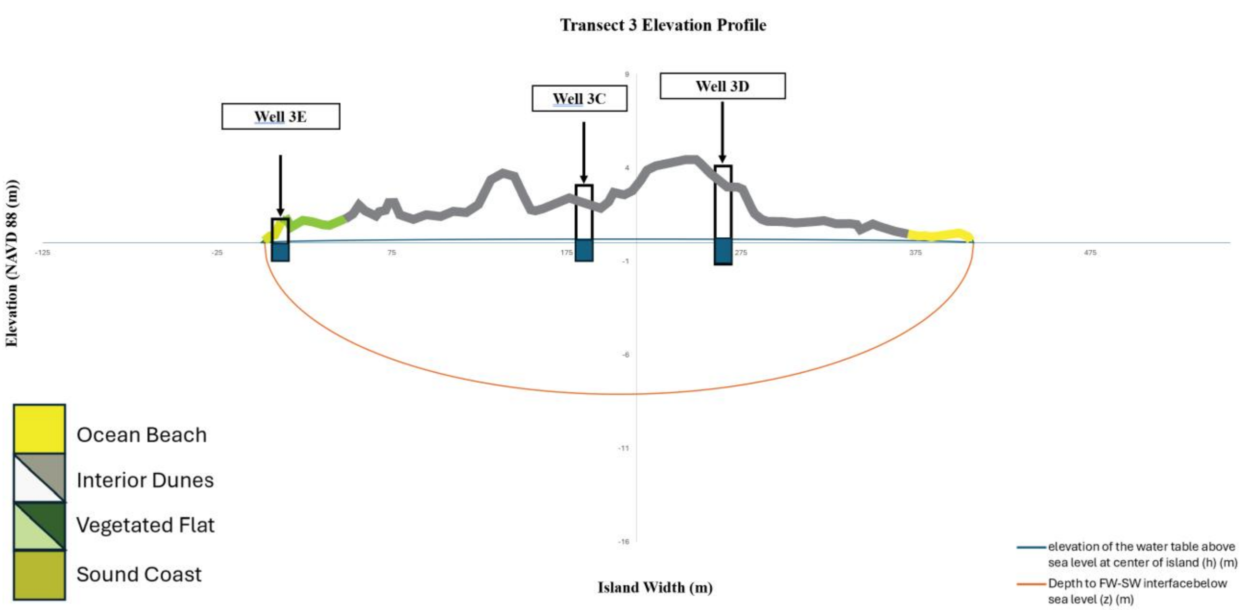

Figure 17). *A cross section of Transect 3 including both elevation of examined transects and predicted aquifer shape. The surface of the island has been colored to demarcated geomorphic units. Wells proximal to transect have been marked by arrows and show approximate depth.*

5.1.6 Freshwater Lens Volume

Freshwater lens volume estimates further reinforce the west-east spatial gradient in freshwater storage capacity. Estimated freshwater volume per meter of island length was approximately: 1) 677.5 m^3/m at Site 1, 2) 568.9 m^3/m at Site 2, and 3) 391.2 m^3/m at Site 3. These values were then multiplied by approximate island length (4,180 m) and averaged to yield a total freshwater lens volume of approximately 2.28×10^6 m^3. This estimate assumes the three study sites capture the dominant west–east variability in freshwater-lens thickness and that alongshore variability is secondary at the island scale.

This estimated freshwater-lens volume is consistent with the expected order of magnitude for barrier-island aquifers. For comparison, a freshwater-lens volume of approximately 31×10^6 m^3 was estimated for Savary Island, British Columbia using a similar analytical freshwater-lens model (Chesnaux, 2021). Differences in storage magnitude between islands reflect variations in island width, recharge rate, and freshwater-lens thickness, but this comparison supports the interpretation that the freshwater lens beneath the study area represents a relatively small but hydrologically significant freshwater reservoir typical of narrow Atlantic barrier-island systems.

5.1.7 Objective 1 Summary

Results from precipitation monitoring, recharge estimation, sediment analysis, and analytical modeling collectively indicate that freshwater lens thickness and storage capacity decrease systematically from west to east across Shackleford Banks. While seasonal precipitation variability influences recharge magnitude, geomorphology and contiguous island width exert the dominant control on freshwater lens dimensions, producing persistent spatial patterns that are consistent across multiple estimation methods.

5.2 Objective 2: Spatial Variability of Electrical Conductivity Across Geomorphic and Topographic Gradients

This objective evaluates how near-surface apparent electrical conductivity (ECa), used as a proxy for salinity, varies across geomorphic units, elevation gradients, and seasons on Shackleford Banks. Results are presented to emphasize persistent spatial structure and the relative influence of geomorphology, topography, and seasonal forcing.

Mean and median ECa appeared to have an inverse relationship with frequency, with the highest ECa readings being observed in the 450Hz frequency band. Standard deviation follows a similar trend, with lower frequency bands exhibiting larger standard deviations (Table 1). Collected FD-EMI and topographic data exhibited a strong positive skew for all numeric variables excluding elevation, which exhibited a slight-to-moderate negative skew. Skewness appeared to have a direct relationship with frequency, with higher frequencies exhibiting a more extreme positive skew (Table 1).

Table 1). *Mean, median, standard deviation, skewness, and kurtosis of each numerical variable across all datasets*

ECa Frequency Band	Mean	Median	StdDev	Skewness	Kurtosis
450Hz (mS/m)	151.485	90.722	183.096	3.056	22.416
1530Hz (mS/m)	57.677	26.562	96.576	5.414	47.133
5010Hz (mS/m)	57.232	28.172	95.453	5.716	51.841
18210Hz (mS/m)	53.597	24.237	96.03	6.198	59.686
63030Hz (mS/m)	43.942	15.03	91.822	6.663	67.763
Topographic Variable	**Mean**	**Median**	**StdDev**	**Skewness**	**Kurtosis**
elevation	4.276	3.696	4.345	-0.379	5.389
slope	4.656	2.707	4.914	1.898	4.599
curvature	0.701	0.248	4.827	0.62	2.733

5.2.1 Spatial and Seasonal Patterns in Apparent Electrical Conductivity

FD-EMI surveys revealed strong and repeatable spatial contrasts in ECa across all transects and survey seasons (Table 2). Across all frequencies, interior dune environments consistently exhibited the lowest ECa values, while sound-side coastal environments exhibited the highest conductivity, followed by ocean-facing coasts and vegetated flats. Summer surveys consistently exhibited higher ECa values than spring and winter across all geomorphic units, indicating seasonal enhancement of near-surface salinity (Figures 18-26; Table 2).

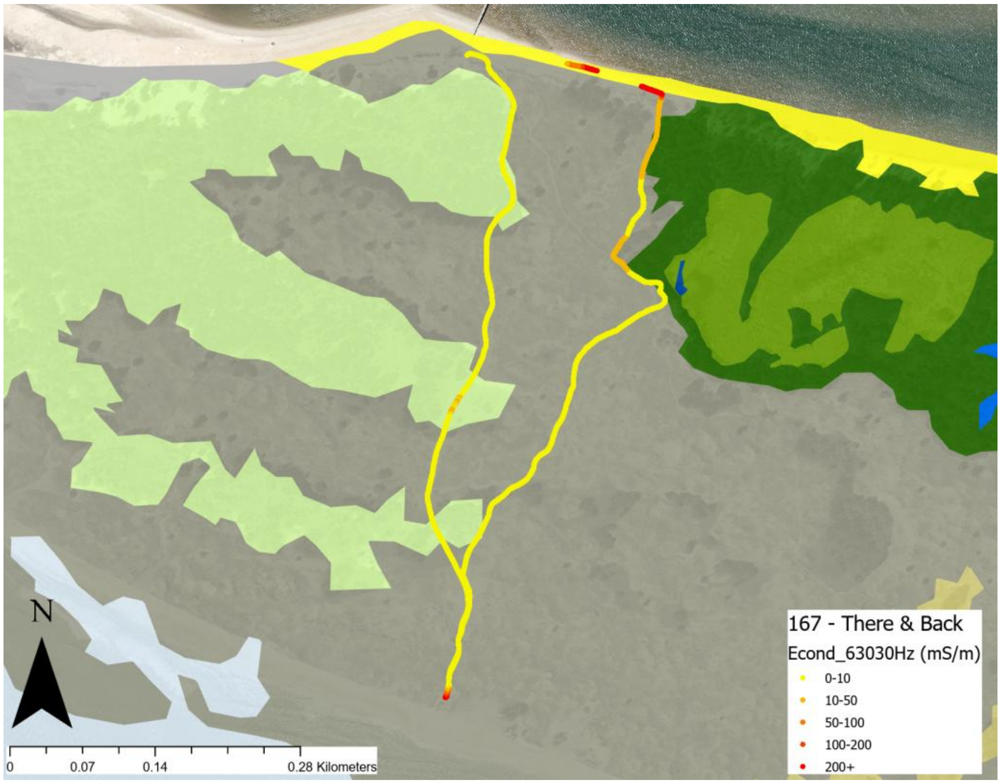

Figure 18). *FD-EMI results from Transect 1 from the 63030Hz frequency band Winter FD-EMI survey conducted 02/12/2025.*

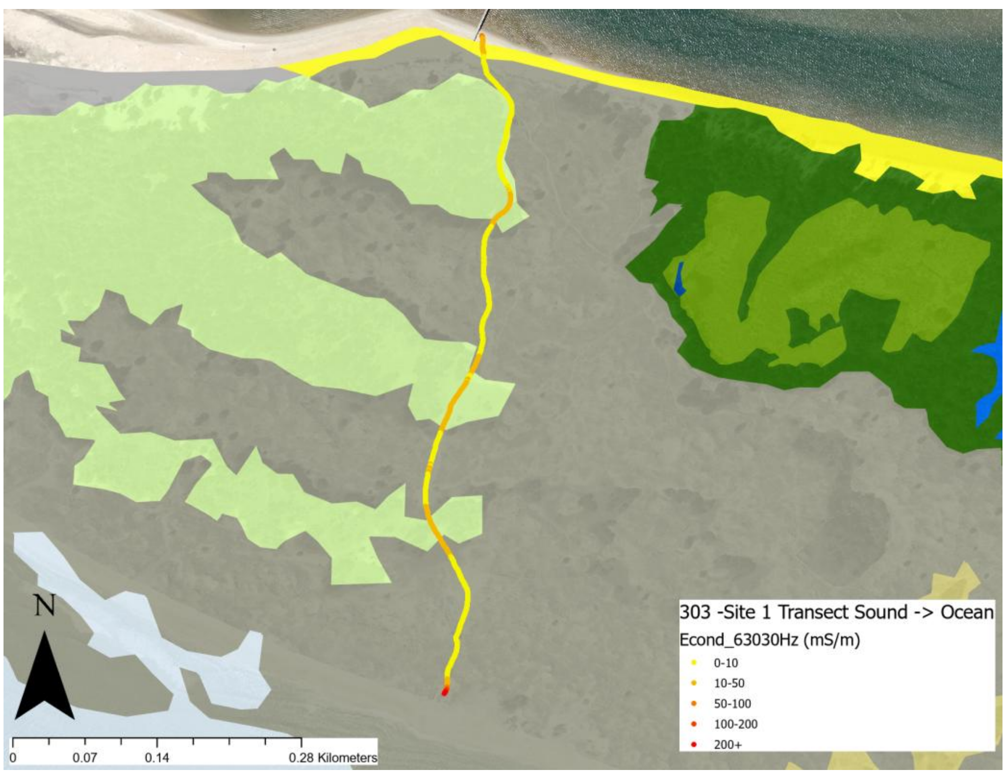

Figure 19). *FD-EMI results from Transect 1 from the 63030Hz frequency band Spring FD-EMI survey conducted 05/12/2025*

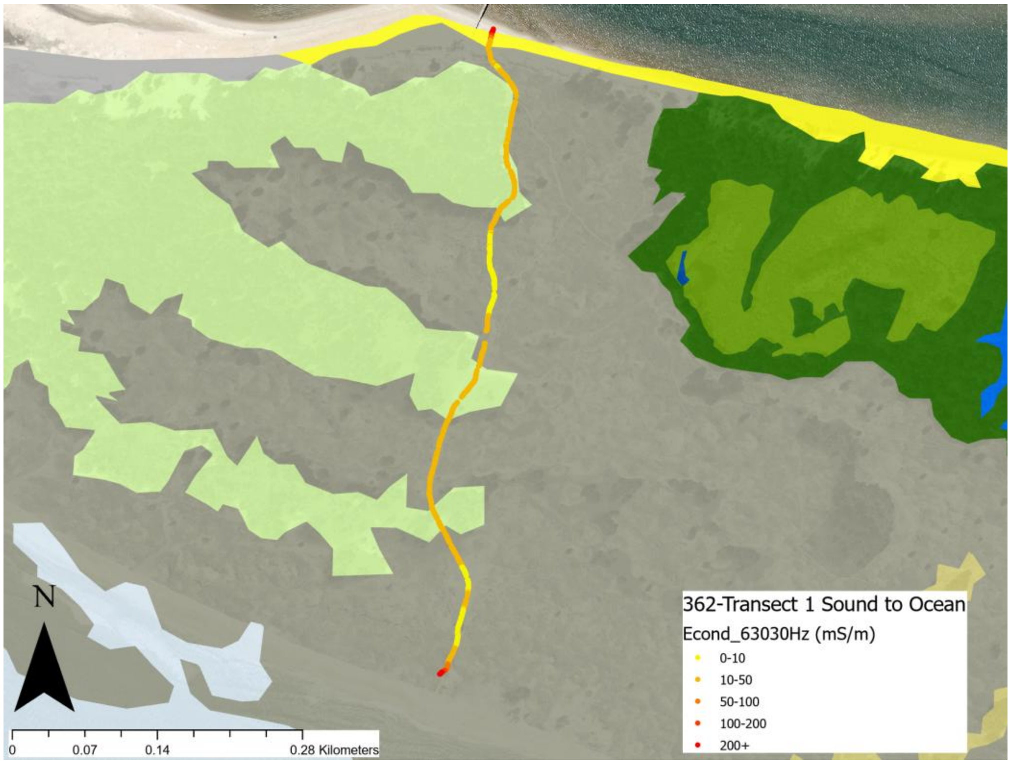

Figure 20). *FD-EMI results from Transect 1 from the 63030Hz frequency band Summer FD-EMI survey conducted 09/01/2025. Survey Transects show distinct changes in ECa readings across different geomorphic units.*

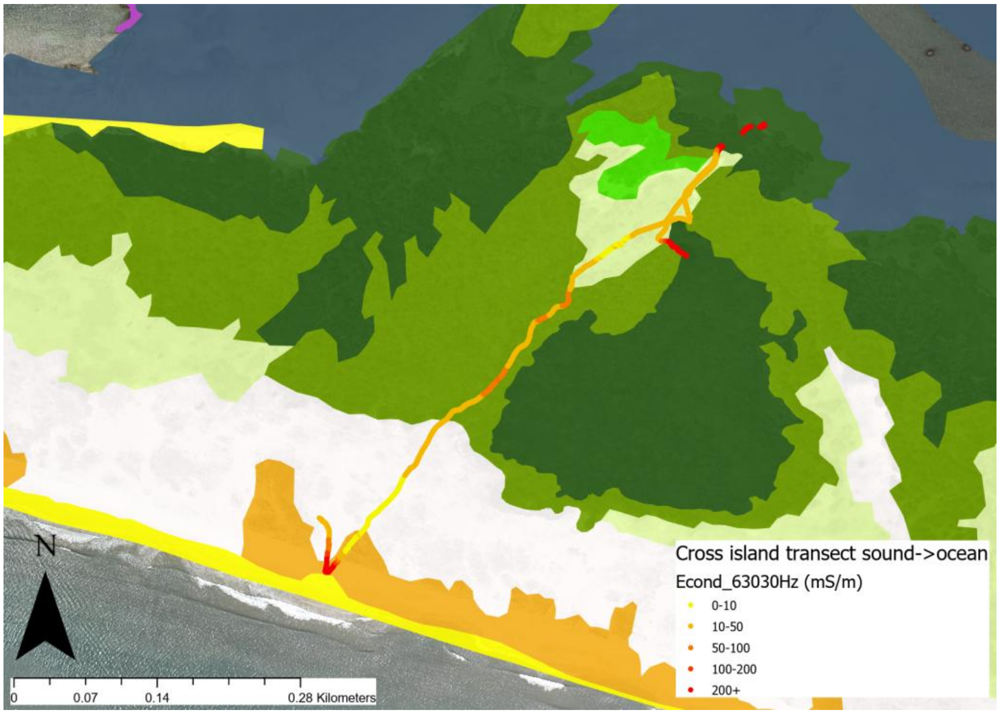

Figure 21). *FD-EMI results from Transect 2 from the 63030Hz frequency band Winter FD-EMI survey conducted 02/12/2025*

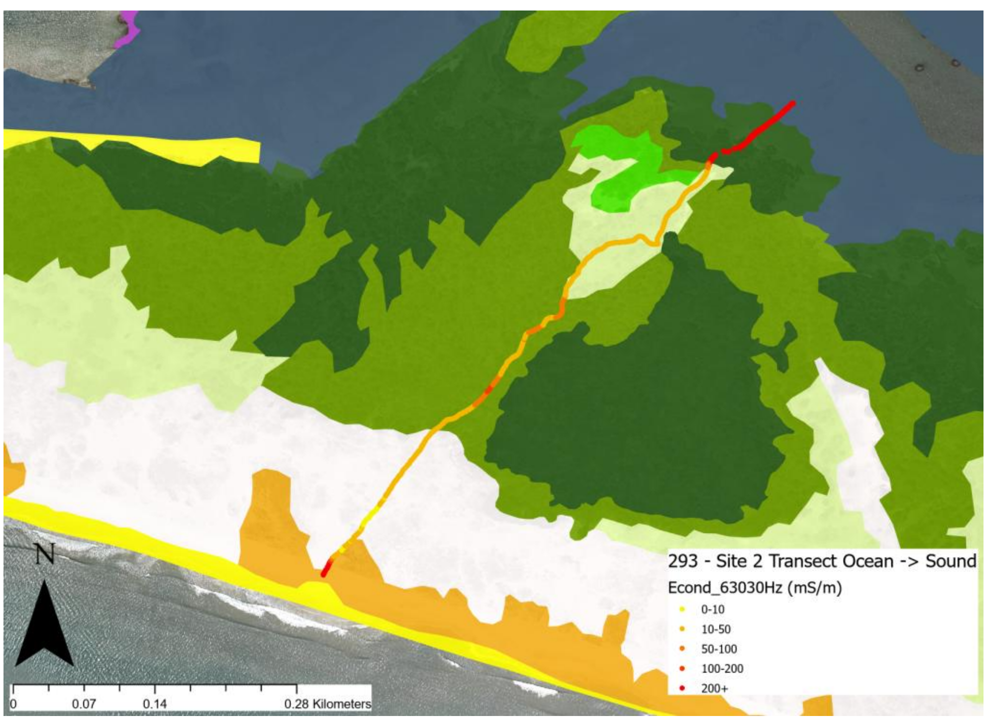

Figure 22). *FD-EMI results from Transect 2 from the 63030Hz frequency band Spring FD-EMI survey conducted 05/12/2025.*

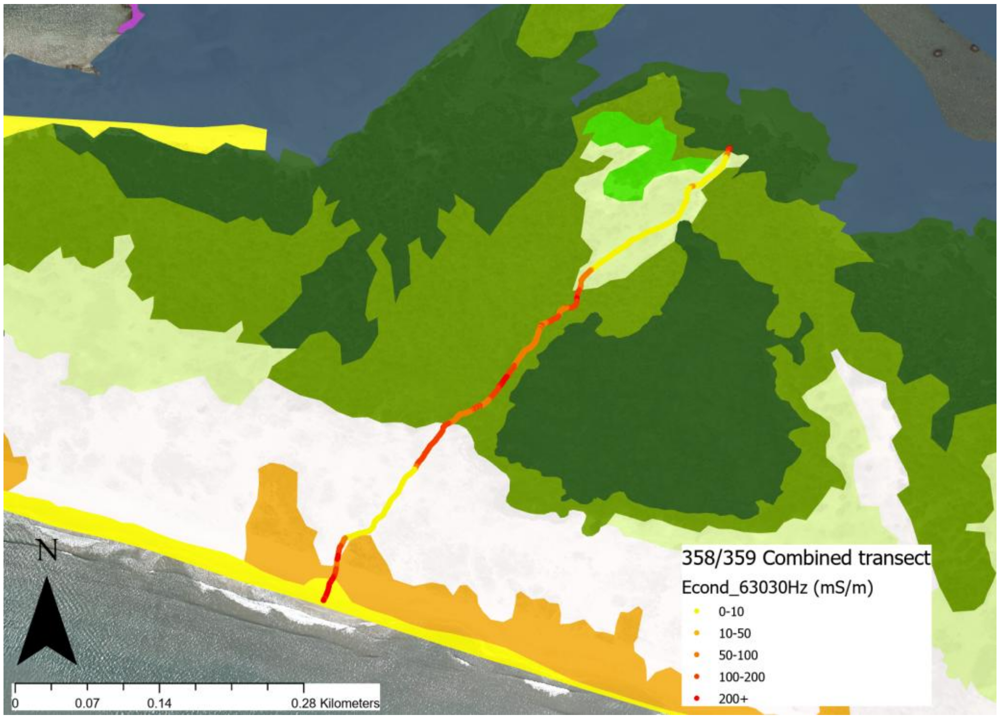

Figure 23). FD-EMI results from Transect 2 from the 63030Hz frequency band Summer FD-EMI survey conducted 09/01/2025. Survey Transects show distinct changes in ECa readings across different geomorphic units.

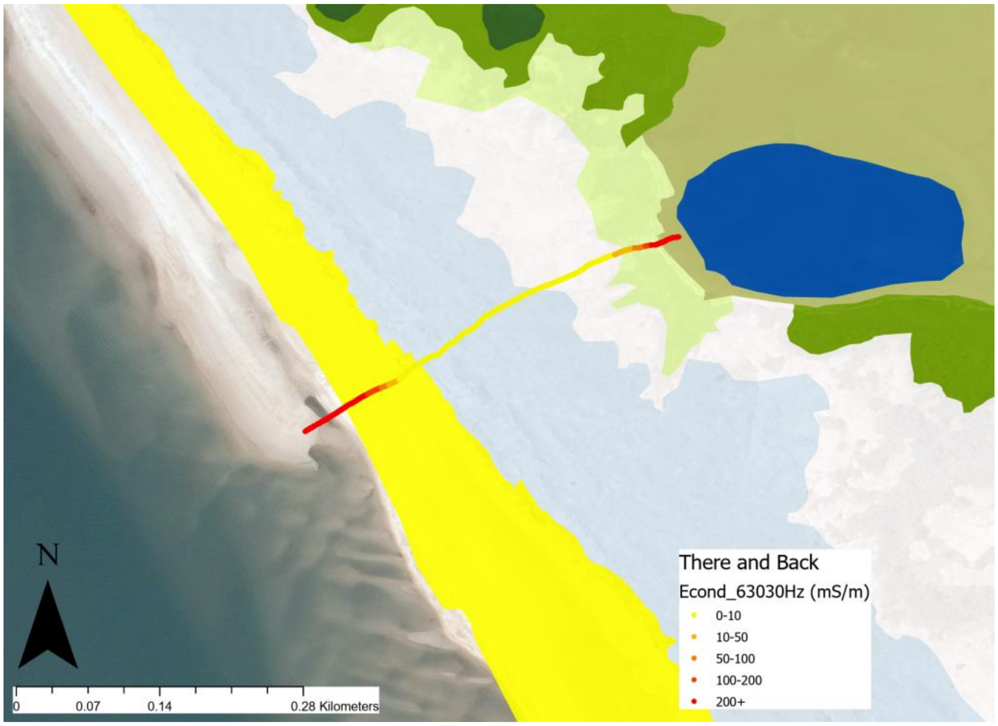

Figure 24). *FD-EMI results from Transect 3 from the 63030Hz frequency band Winter FD-EMI survey conducted 02/12/2025.*

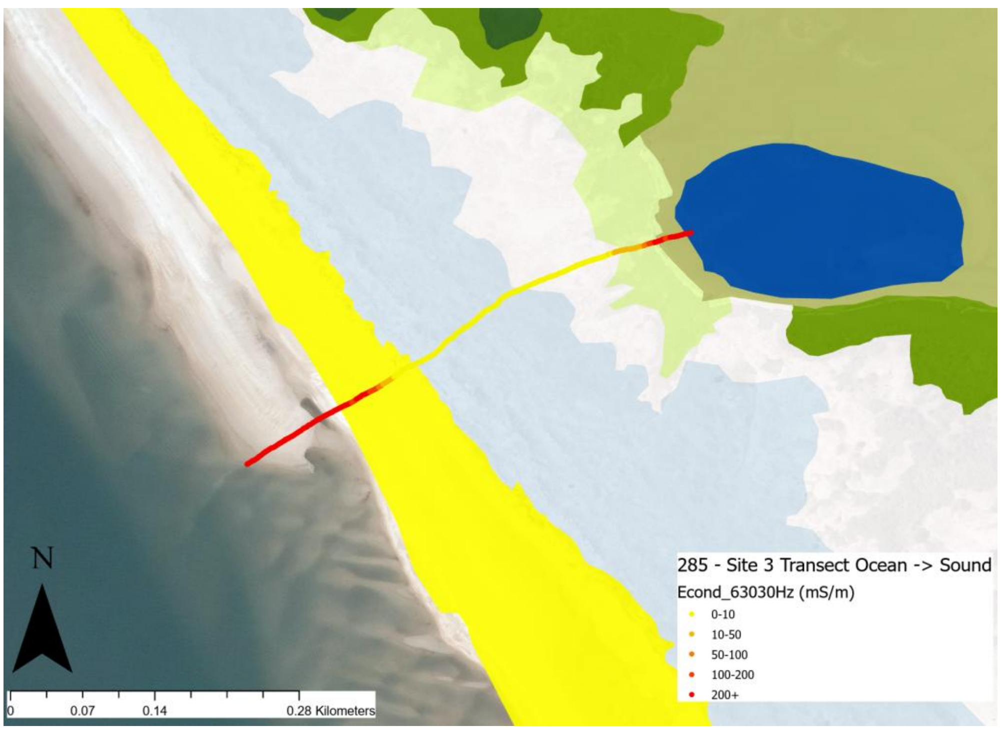

Figure 25).*FD-EMI results from Transect 3 from the 63030Hz frequency band Spring FD-EMI survey conducted 05/12/2025.*

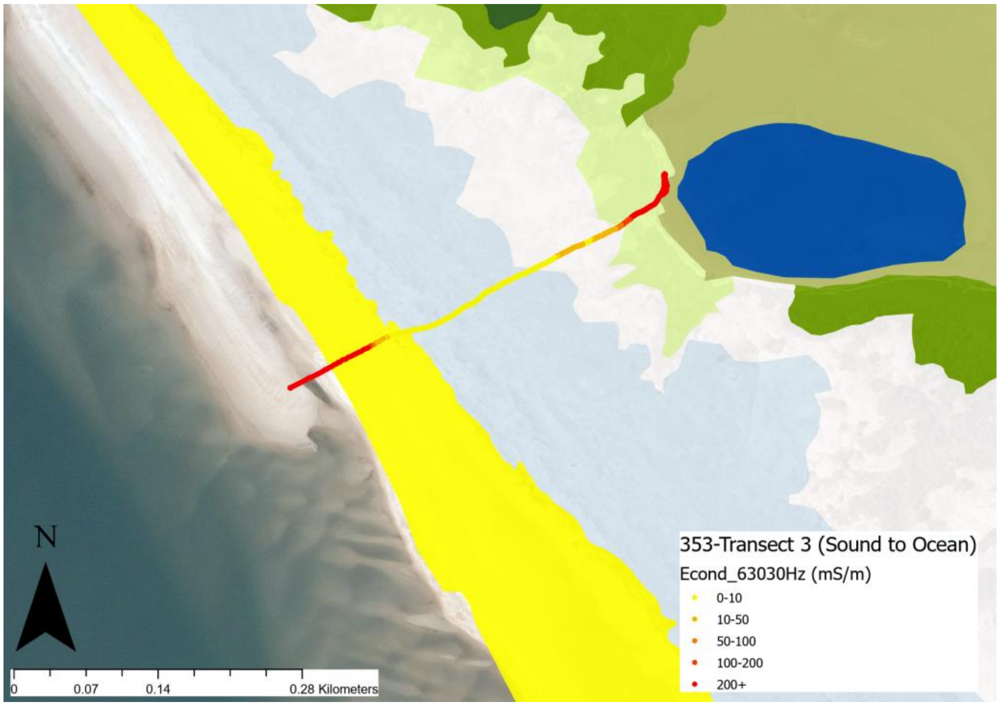

Figure 26). *FD-EMI results from Transect 3 from the 63030Hz frequency band. A) Winter FD-EMI survey conducted 02/12/2025. B) Spring FD-EMI survey conducted 05/12/2025. D) Summer FD-EMI survey conducted 09/01/2025. Survey Transects show distinct changes in ECa readings across different geomorphic units.*

Table 2). *Mean temperature corrected ECa by season & geomorphic unit*

Geomorphic Unit	Season	Mean	StdDev
Dunes	spring	8.144	6.896
Dunes	summer	21.434	32.270
Dunes	winter	6.218	8.548
Ocean Coast	spring	87.626	100.096
Ocean Coast	summer	113.032	96.124
Ocean Coast	winter	98.295	107.787
Sound Coast	spring	137.211	114.085
Sound Coast	summer	336.488	341.703
Sound Coast	winter	225.257	142.485
Vegetated Flat	spring	29.549	20.747
Vegetated Flat	summer	62.909	54.204
Vegetated Flat	winter	29.656	21.683

The lowest mean ECa value (6.22 mS/m) was recorded within interior dunes during winter at the highest operating frequency (63,030 Hz), while the highest mean value (413.04 mS/m) occurred in sound-side environments during summer at the lowest frequency (450 Hz) (Appendix A). The sound coast was also observed to have the highest standard deviation across all seasons, followed by the ocean coast, vegetated flats, and interior dunes.

Despite this seasonal variability, the relative ranking of geomorphic units remained consistent across all seasons and frequencies, indicating that spatial structure dominates over temporal variability. Interior dunes remained distinct from coastal and low-lying environments regardless of season.

5.2.2 Relationships Between ECa and Topographic Gradients

ECa exhibited strong, statistically significant negative relationships with elevation and slope across all FD-EMI frequencies (Spearman ρ, $p \ll 0.001$; Table 3). The strength of these relationships increased systematically with frequency, indicating that shallow subsurface conductivity is more tightly coupled to topography than deeper-sensing measurements.

Elevation-ECa correlations strengthened from weak relationships at 450 Hz ($\rho \approx -0.12$) to moderate relationships at 63,030 Hz ($\rho \approx -0.50$), while slope showed a similar frequency-dependent increase in correlation strength (Table 3).

Curvature exhibited weak and inconsistent correlations with ECa, suggesting limited influence on conductivity patterns relative to elevation and slope.

Table 3). *Spearman ranked test for continuous variables (elevation, slope, and curvature) for each frequency.*

Frequency	Predictor	rho	p_value
450	Elevation	-0.1268	$p \ll 0.001$
450	Slope	-0.1306	$p \ll 0.001$
450	Curvature	-0.038	$p \ll 0.001$
1530	Elevation	-0.2398	$p \ll 0.001$
1530	Slope	-0.3501	$p \ll 0.001$
1530	Curvature	-0.1488	$p \ll 0.001$
5010	Elevation	-0.3684	$p \ll 0.001$
5010	Slope	-0.4265	$p \ll 0.001$
5010	Curvature	-0.0594	$p \ll 0.001$
18210	Elevation	-0.4314	$p \ll 0.001$
18210	Slope	-0.4494	$p \ll 0.001$
18210	Curvature	-0.0289	$p \ll 0.001$
63030	Elevation	-0.5052	$p \ll 0.001$
63030	Slope	-0.4757	$p \ll 0.001$
63030	Curvature	-0.0025	5.28E-01

Kruskal-Wallis tests further confirmed statistically significant differences in ECa among geomorphic units for all five frequencies ($p < 0.001$; Table 4). Test statistics increased with frequency, reinforcing that near-surface conductivity exhibits the strongest geomorphic differentiation which decreases as depth increases. Seasonal Kruskal-Wallis tests also showed significant differences among seasons for all frequencies ($p < 0.001$; Table 4), although these effects were secondary to geomorphic controls.

Table 4). *Kruskal-Wallis H Test Between ECa by frequency band and both Geomorphic Units and season.*

Frequency	Frequency and Geomorphic Unit H_Stat	Frequency and Season H_Stat
450	5374.33	1749.94
1530	19038.97	784.465
5010	24527.78	2604.57
18210	25625.11	3671.856
63030	25863.06	5096.604

Post hoc Dunn's tests demonstrated that interior dunes were statistically distinct from all other geomorphic units across all frequencies (Table 5). Coastal environments (ocean and sound coast) were consistently distinct from one another, with the sound coast having a higher conductivity across all seasons and frequencies. The only exception was vegetated flats, which exhibited partial convergence with coastal units at the shallowest depths, particularly at 63,030 Hz (Table 5).

Table 5). *Dunn's Post-Hoc Test on ECa and Geomorphic Unit.*

Frequency (Hz)	Geomorphic Unit	Dunes	Ocean Coast	Sound Coast	Vegetated Flat
450	Dunes	1	0	0	0
450	Ocean Coast	-	1	0	0
450	Sound Coast	-	-	1	0
450	Vegetated Flat	-	-	-	1
1530	Dunes	1	0	0	0
1530	Ocean Coast	-	1	0	0
1530	Sound Coast	-	-	1	0
1530	Vegetated Flat	-	-	-	1
5010	Dunes	1	0	0	0
5010	Ocean Coast	-	1	0	0
5010	Sound Coast	-	-	1	0
5010	Vegetated Flat	-	-	-	1
18210	Dunes	1	0	0	0
18210	Ocean Coast	-	1	0	0
18210	Sound Coast	-	-	1	0
18210	Vegetated Flat	-	-	-	1
63030	Dunes	1	0	0	0
63030	Ocean Coast	-	1	0	3.46E-03
63030	Sound Coast	-	-	1	0
63030	Vegetated Flat	-	-	-	1

5.2.3 Multivariate Controls on Conductivity Patterns

Robust regression analysis confirms that geomorphic unit is the dominant predictor of ECa across all frequencies (Table 6). Relative to interior dunes, sound-side environments exhibited the largest positive conductivity offsets, followed by ocean-facing coasts and vegetated flats. These offsets persisted across all depths of investigation, indicating that geomorphology exerts a first-order control on shallow subsurface conductivity patterns.

Seasonal effects were present but smaller in magnitude. Summer was consistently associated with positive ECa offsets across all frequencies, while winter effects diminished or reversed at higher frequencies, indicating reduced near-surface salinity during cooler months (Table 6).

Topographic predictors (elevation, slope, curvature) exhibited comparatively small coefficients relative to geomorphic class, further supporting the conclusion that mapped geomorphic environments integrate multiple controlling factors influencing salinity, including elevation, hydrologic connectivity, and exposure to marine processes.

Table 6). *Robust linear model (Huber loss) coefficients relating ECa to geomorphic, seasonal, and topographic predictors across FD-EMI frequency bands.*

Predictor	**ECa 450 Hz**	**ECa 1530 Hz**	**ECa 5010 Hz**	**ECa 18210 Hz**	**ECa 63030 Hz**
Intercept	34.06	7.19	21.40	19.84	12.54
Geomorphic Unit (ref = Dunes)					
Ocean Coast	159.46	129.38	118.29	84.86	49.65
Sound Coast	170.79	202.55	206.11	214.73	208.60
Vegetated Flat	34.02	26.39	26.17	23.12	18.10
Season (ref = Spring)					
Summer	81.04	26.53	14.20	12.66	10.76
Winter	44.26	16.95	-1.35	-2.46	-0.86
Topography					
Elevation	1.31	0.50	0.16	0.07	-0.07
Slope	-1.45	-1.45	-1.37	-1.25	-1.02
Curvature	-0.70	-0.50	-0.22	-0.12	-0.09

5.2.4 Objective 2 Summary

Results from FD-EMI surveys, terrain analysis, and statistical modeling demonstrate that near-surface electrical conductivity on Shackleford Banks is spatially structured by geomorphology and elevation, with persistent contrasts among dunes, flats, and coastal environments. While seasonal variability modulates conductivity magnitude, the spatial organization of salinity patterns remains stable across seasons and depths of investigation, with the strongest differentiation occurring in the shallow subsurface.

5.3 Objective 3: Temporal Dynamics in Groundwater Levels and Salinity

This objective characterizes temporal variability in groundwater levels and electrical conductivity across Shackleford Banks and evaluates the relative influence of precipitation-driven recharge and marine forcing on groundwater behavior.

Precipitation influence was evaluated by identifying longer-period seasonal recharge signals, whereas marine forcing was assessed by examining short-period fluctuations associated with tidal cycles and salinity variability. Differences in response timing and dominant periodicities between groundwater levels and conductivity were used to distinguish recharge-driven variability from marine-controlled processes.

5.3.1 Groundwater-Level Variability

Groundwater levels across all monitoring sites exhibited coherent temporal responses characterized by rapid rises following major precipitation events and gradual recessions during dry periods (Figures 27-29). Prominent water-level increases occurred during September 2024 (when a subtropical cyclone passed over the island) and March 2025 (large low-pressure system passed over the island), corresponded to the largest recorded precipitation events during the study period.

Average groundwater elevations across the island ranged from approximately 0.3 to 1.5 m above mean sea level (Figures 27-29). Site 2 exhibited the highest mean groundwater levels (0.59 m asl), followed closely by Site 1 (0.59 m asl). This similarity between Sites 1 and 2 despite the differences in island width and freshwater lens thickness are likely driven by storm activity/surge increasing water levels in wells proximal to the ocean coast (1D and 2C), which are elevated compared to the other wells in their respective sites. while Site 3 consistently recorded the lowest groundwater levels (0.42 m asl), reflecting its lower elevation and proximity to Barden Inlet (Figure 29).

At the individual well scale, the highest average groundwater level was recorded at Well 1C (0.77 m asl), located within the interior dune system, while the lowest average groundwater level occurred at Well 3E (0.17 m asl) within a sound-side geomorphic unit (Figures 27-29). These patterns mirror the spatial groundwater gradients inferred from analytical freshwater lens modeling.

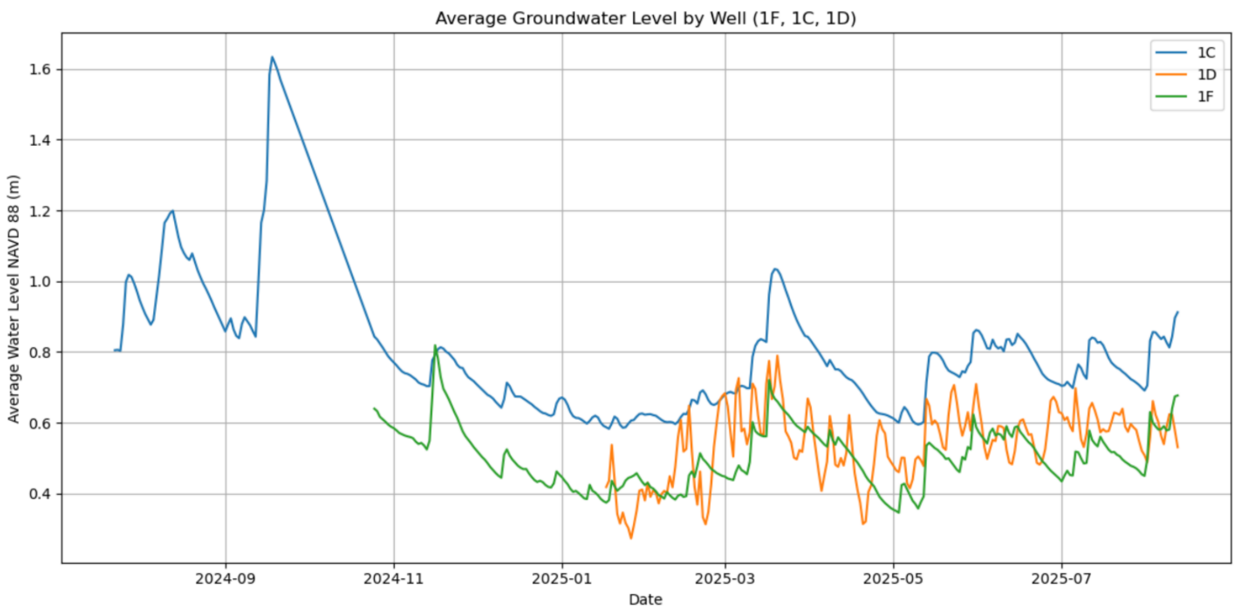

Figure 27). *Average groundwater levels of each Well proximal to Transect 1 over the course of the study. Water levels are recorded in meters above sea level in reference to NAVD88. Refer to* Figures 4-6 *for well locations.*

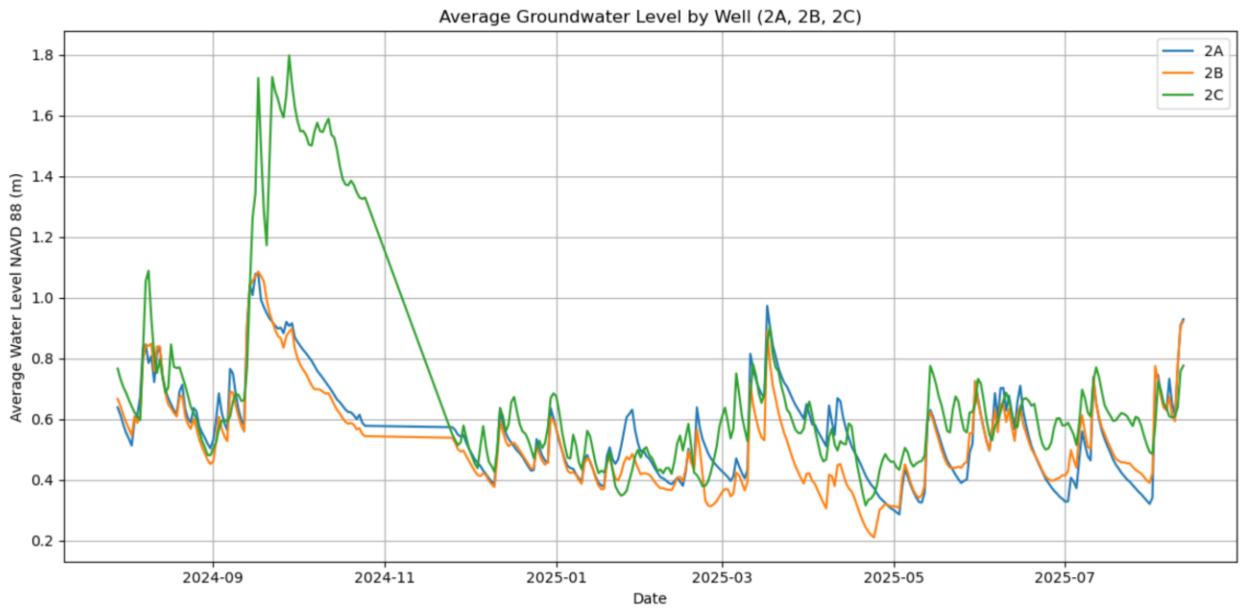

Figure 28). *Average groundwater levels of each Well proximal to Transect 2 over the course of the study. Water levels are recorded in meters above sea level in reference to NAVD88. Refer to* Figures 4-6 *for well locations.*

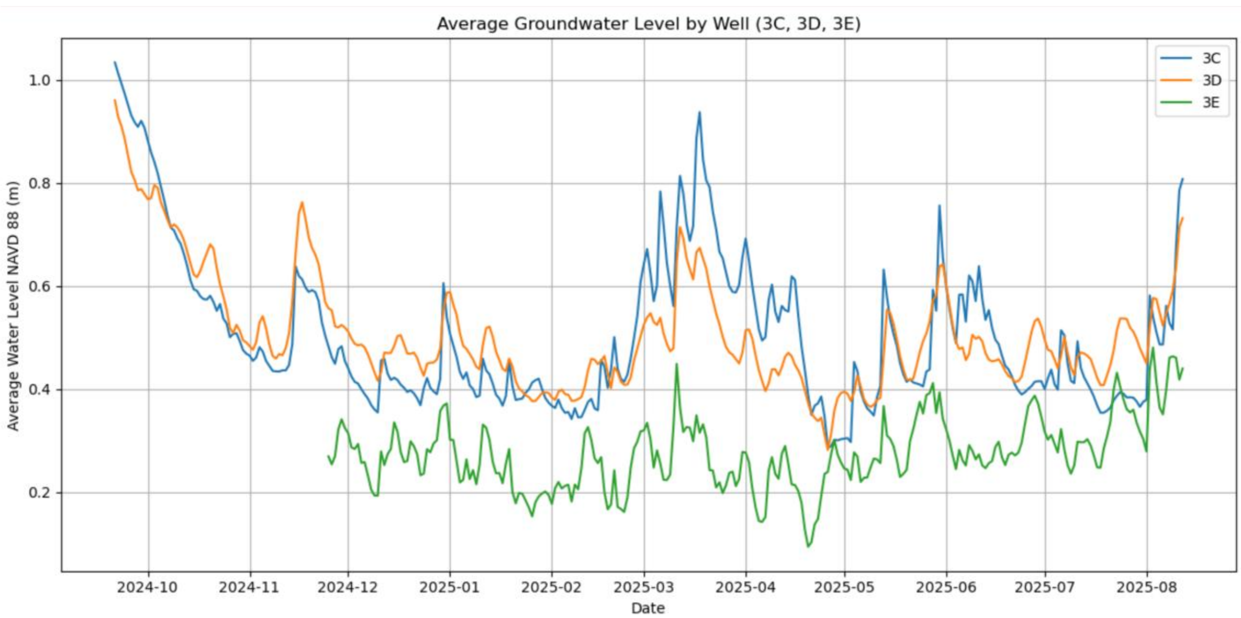

Figure 29). *Average groundwater levels of each Well proximal to Transect 3 over the course of the study. Water levels are recorded in meters above sea level in reference to NAVD88. Refer to Figures 4-6 for well locations.*

Across all sites, water level values generally increased following major precipitation events, particularly at interior and central locations, indicating these locations procure most of their water through recharge. In contrast, coastal and inlet-proximal wells exhibited water levels persistently linked with tidal responses, suggesting limited freshwater accumulation in these environments (Figures 27-29).

5.3.2 Temporal Variability in Electrical Conductivity

Groundwater specific conductivity exhibited substantial temporal and spatial variability, with values ranging from near-freshwater conditions to brackish concentrations exceeding 27,000 µS/cm (or 16.5 ppt salinity) (Figures 30-32). Periods of zero conductivity correspond to intervals when wells were temporarily dry and are excluded from interpretation.

Site 3 consistently exhibited the highest average conductivity, followed by Site 1 and Site 2 (Figures 30-32). At the well scale, the highest mean conductivities were observed at Wells 1F (Mullet Pond) and 3E (intertidal zone), all located within coastal or sound-side geomorphic units (Figures 30 & 32), while Well 1C exhibited the lowest average conductivity (1240 µS/cm), consistent with its interior dune setting (Figure 30).

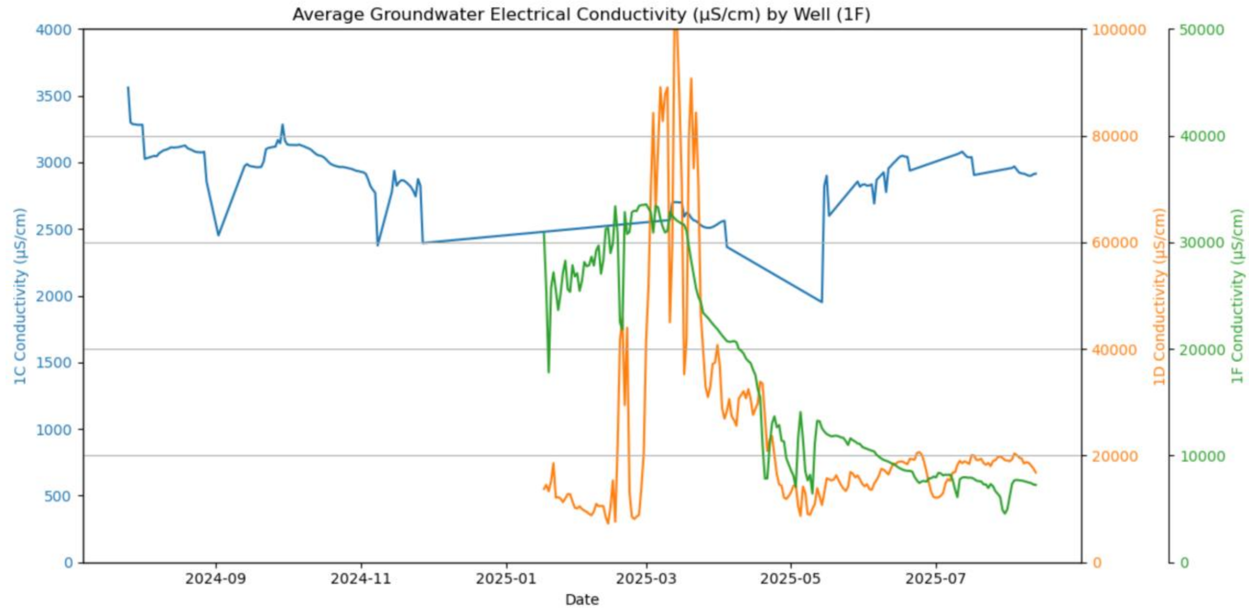

Figure 30). *Average specific conductivity measurement (µS/cm) of each well proximal to Transect 1 over the course of the study. Note: The three data series are plotted using separate y-axes with different scales to allow for clearer comparison of trends among wells. Refer to Figures 4-6 for well locations.*

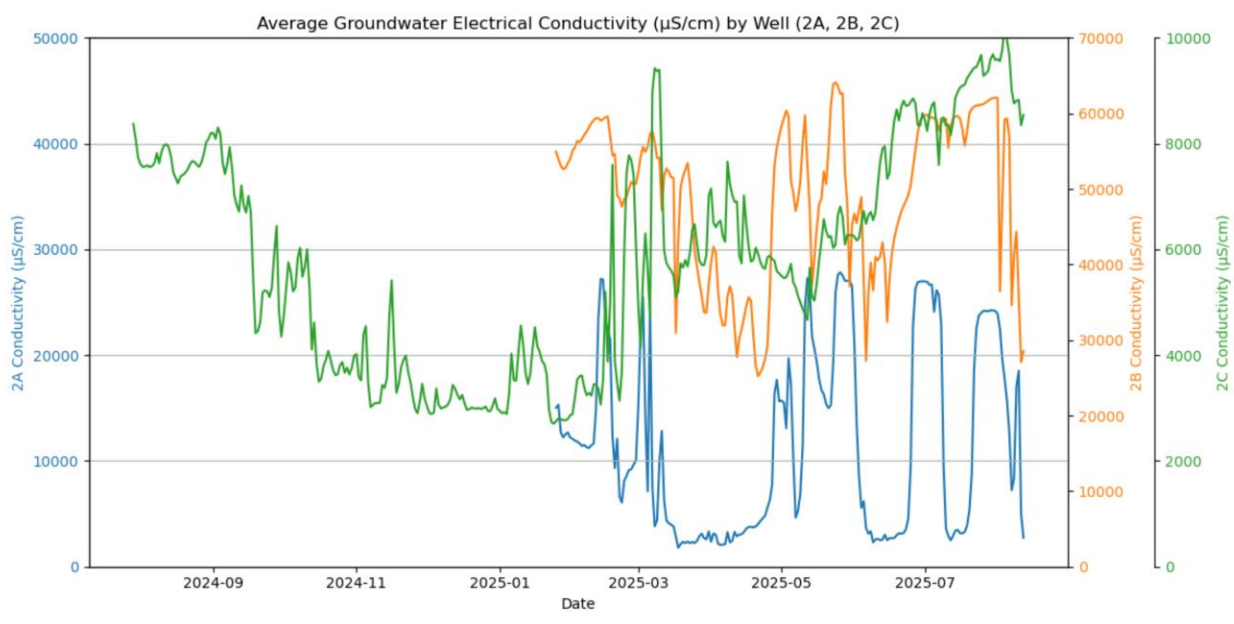

Figure 31). *Average specific conductivity measurement (µS/cm) of each well proximal to Transect 2 over the course of the study. Note: The three data series are plotted using separate y-axes with different scales to allow for clearer comparison of trends among wells. Refer to* Figures 4-6 *for well locations.*

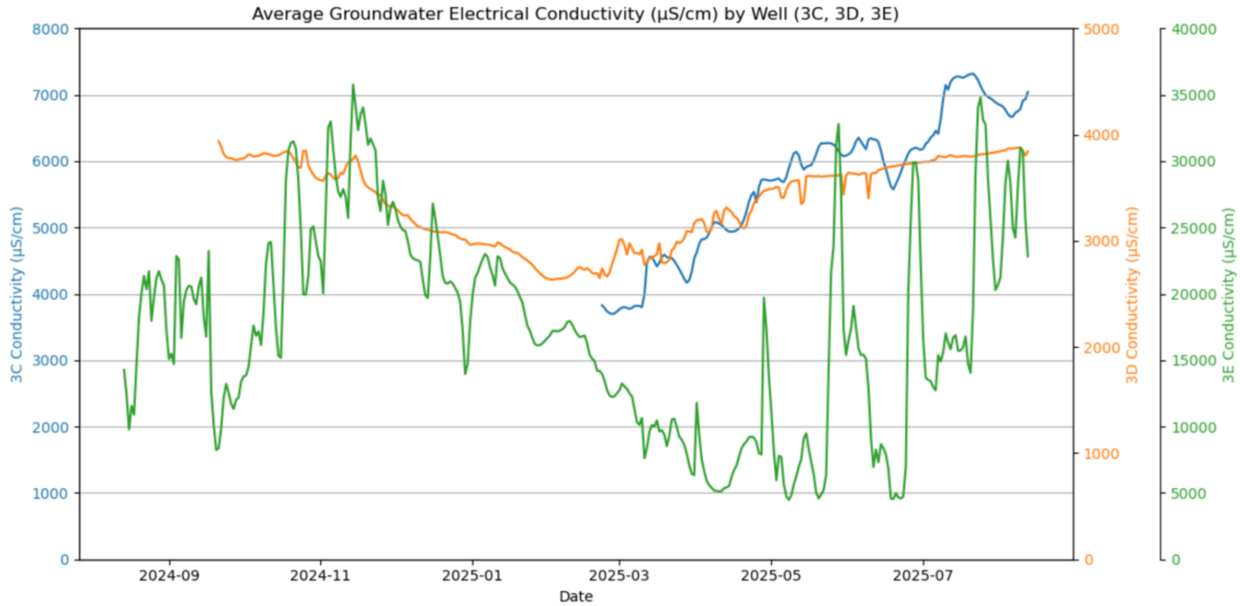

Figure 32). *Average specific conductivity measurement (µS/cm) of each well proximal to Transect 3 over the course of the study. Note: The three data series are plotted using separate y-axes with different scales to allow for clearer comparison of trends among wells. Refer to Figures 4-6 for well locations.*

Across all sites, electrical conductivity values generally decreased following major precipitation events, particularly at interior and central locations, indicating dilution of saline pore waters during recharge. In contrast, coastal and inlet-proximal wells exhibited persistently elevated conductivity with muted dilution responses, suggesting limited freshwater flushing in these environments (Figures 33-35).

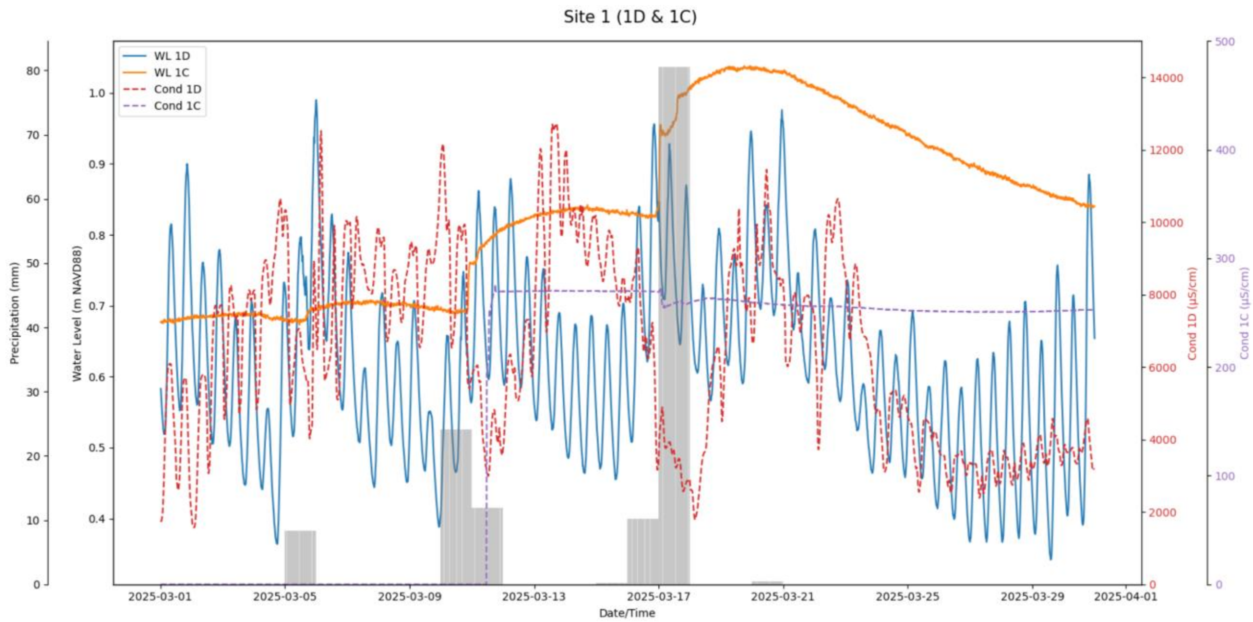

Figure 33). *Log of electrical conductivity and water level of an interior (1C) and coastal (1D) wells along Transect 1 during the month of March, 2025. Precipitation during this period (two notable precipitation events) is marked by grey bars. Water level in well 1C was too low to record a conductivity reading until March 10-11, where a precipitation event occurred. Note: The three data series are plotted using separate y-axes with different scales to allow for clearer comparison of trends among wells. Refer to Figures 4-6 for well locations.*

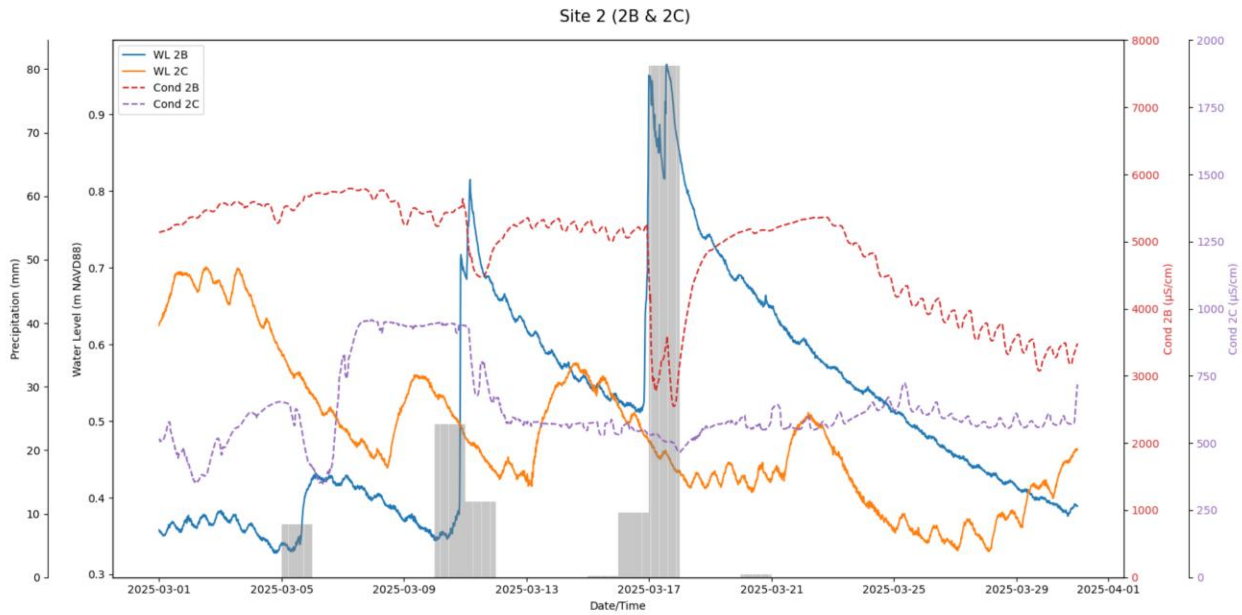

Figure 34). *Log of electrical conductivity and water level of an interior (2B) and coastal (2C) wells along Transect 2 during the month of March, 2025. Precipitation during this period (two notable precipitation events) is marked by grey bars. Note: The three data series are plotted using separate y-axes with different scales to allow for clearer comparison of trends among wells. Refer to Figures 4-6 for well locations.*

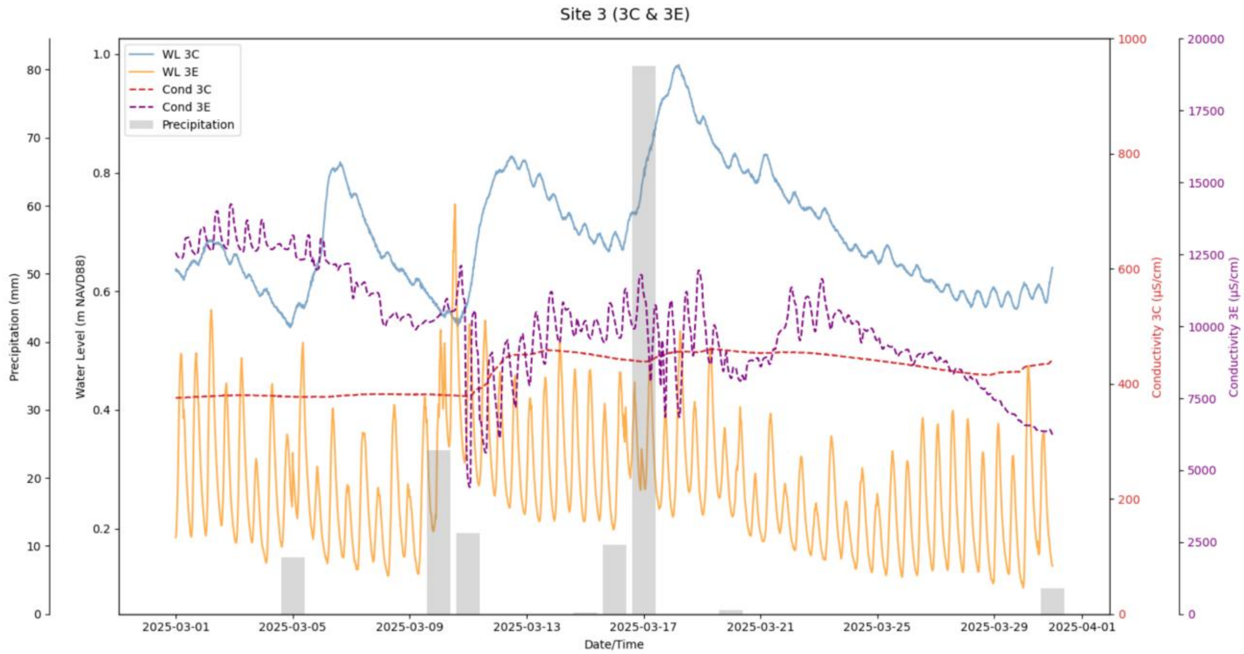

Figure 35). *Log of electrical conductivity and water level of an interior (3C) and coastal (3E) wells along Transect 3 during the month of March 2025. Precipitation (mm) during this period (two notable precipitation events) is marked by grey bars. Note: The three data series are plotted using separate y-axes with different scales to allow for clearer comparison of trends among wells. Refer to Figures 4-6 for well locations.*

5.3.3 Comparison of Temporal Dynamics Across Geomorphic Scales

Comparisons among wells grouped by geomorphic unit reveal a consistent inverse relationship between groundwater elevation and electrical conductivity (Table 7). Interior dune environments exhibited the highest groundwater elevations and lowest conductivity, while sound-side environments recorded the lowest groundwater elevations and highest conductivity.

This relationship is most clearly illustrated by Well 1C, which simultaneously recorded the highest mean groundwater level and the lowest mean conductivity across all monitored wells (Table 7). These results reinforce the spatial patterns identified in Objectives 1 and 2 and demonstrate that geomorphic setting exerts a persistent influence on groundwater salinity dynamics over time.

Table 7). *Average Conductivity & Water Level in Wells and Associated Geomorphic Unit.*

Well	Average Conductivity (mS/m)	Avg Water Level (m)	Geomorphic Unit
3E	17257.99	0.27	Sound Coast
2B	4926.54	0.53	Vegetated Flats
1D	2446.83	0.54	Ocean Coast
1F	1692.70	0.50	Vegetated Flats
2A	1169.20	0.56	Vegetated Flats
2C	579.28	0.68	Dunes
3C	568.23	0.51	Vegetated Flats
3D	335.93	0.51	Dunes
1C	123.80	0.78	Dunes

5.3.4 Frequency-Domain Analysis of Groundwater and Conductivity Time Series

Fast Fourier Transform (FFT) analysis of groundwater level records reveals distinct frequency-domain behavior between coastal and interior wells (Table 9; Figures 36–38). Wells located within ocean-facing and sound-side geomorphic units exhibit dominant periodicities near 12.4 hours (0.52 days), corresponding to principal tidal constituents (M2). In contrast, wells located within interior dune and central island environments exhibit much longer dominant periods on the order of 1,500–1,600 hours (60–70 days), consistent with seasonal or recharge-driven variability.

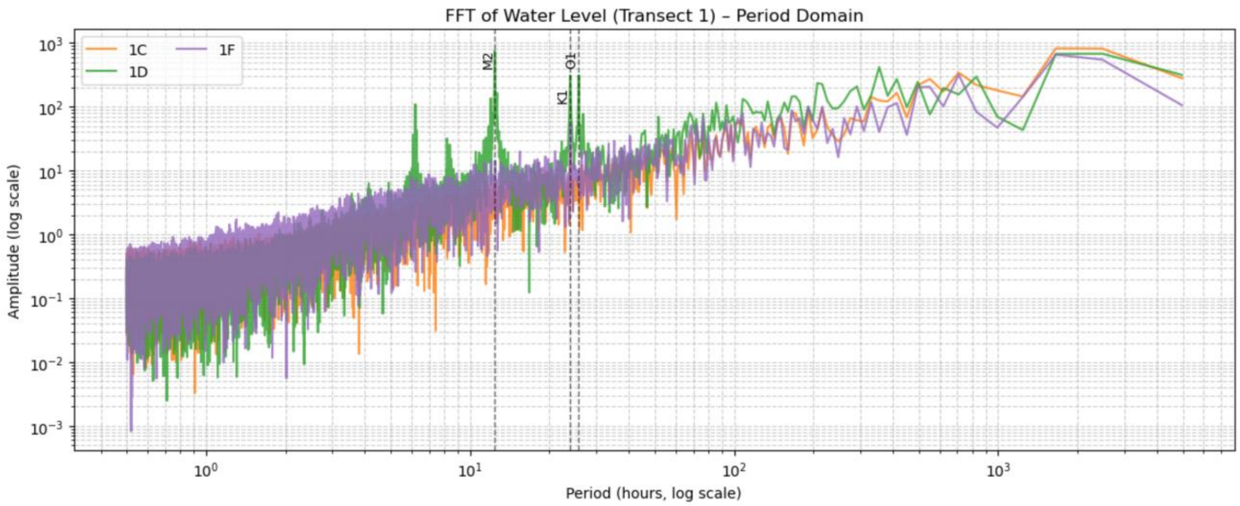

Figure 36). *Results of frequency domain (Fourier) analysis (spectral density vs. period) of water levels from wells located along Transect 1. Refer to* Figures 4-6 *for well locations.*

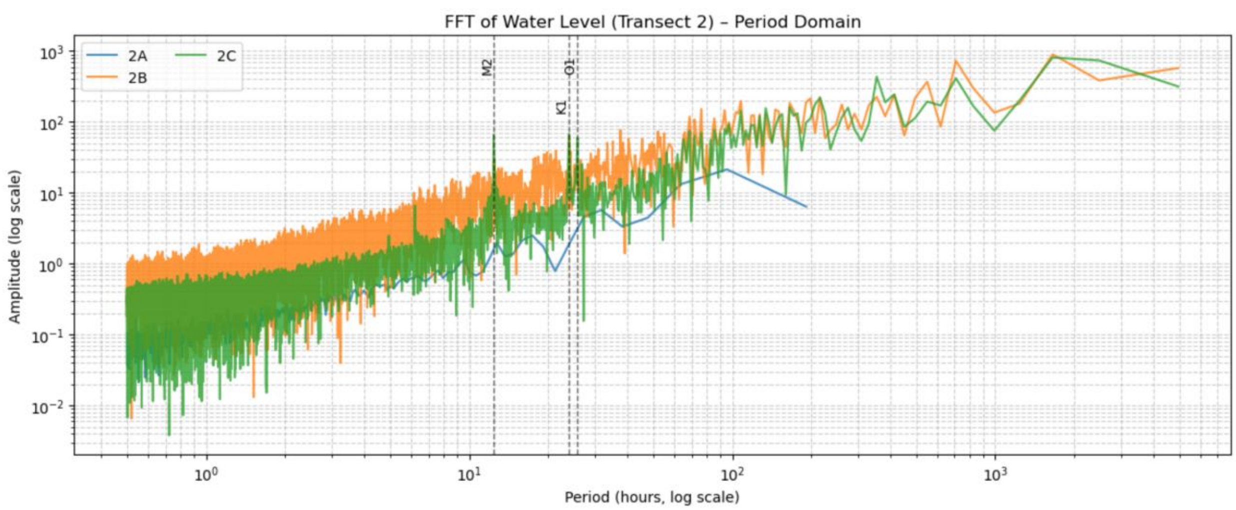

Figure 37). *Results of frequency domain (Fourier) analysis (spectral density vs. period) of water levels from wells located along Transect 2. Refer to* Figures 4-6 *for well locations.*

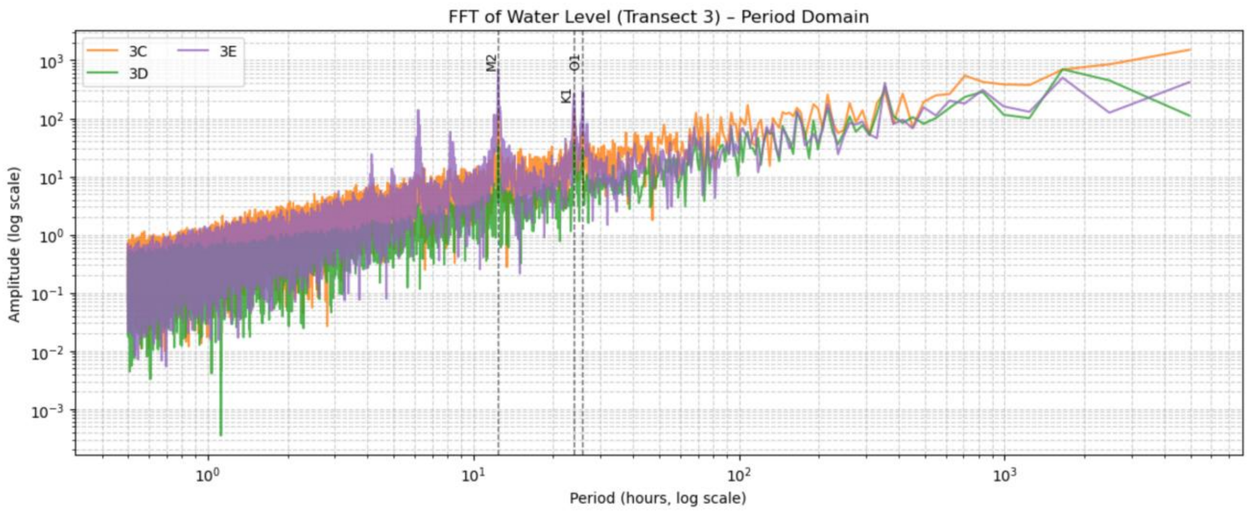

Figure 38). *Results of frequency domain (Fourier) analysis (spectral density vs. period) of water levels from wells located along Transect 3. Refer to* Figures 4-6 *for well locations.*

FFT results for electrical conductivity time series show similar spatial partitioning but with systematically longer dominant periods relative to groundwater levels (Table 8; Figures 39–41). For example, while water levels at coastal Well 1D exhibit tidal periodicity (~12.4 hours), conductivity at the same well exhibits dominant periods near 800 hours (~33 days), indicating delayed and attenuated salinity responses relative to hydraulic forcing.

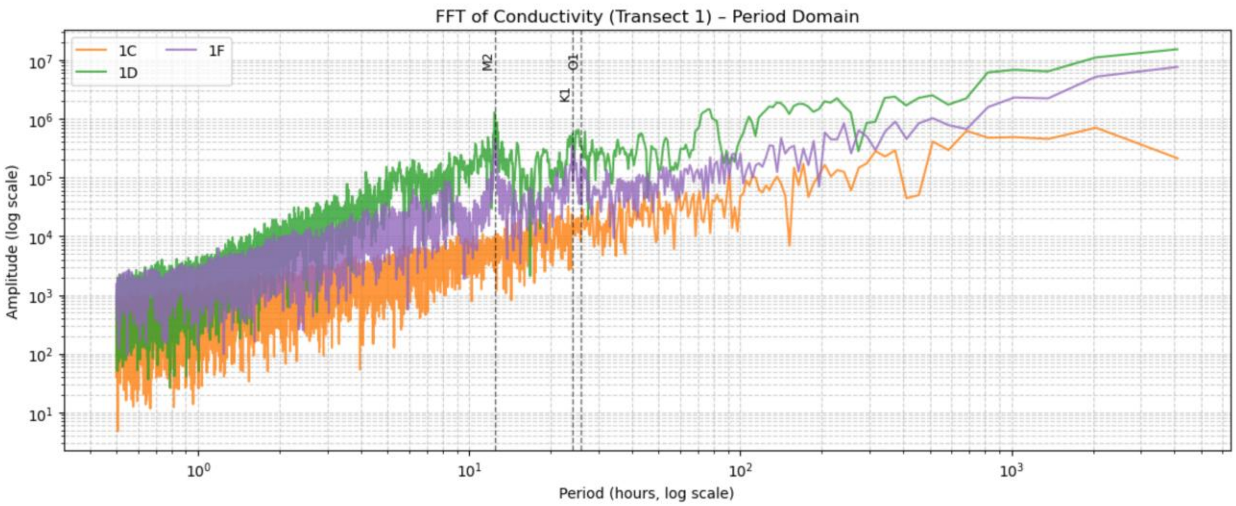

Figure 39). *Results of frequency domain (Fourier) analysis (spectral density vs. period) of conductivity readings from wells located along Transect 1. Refer to* Figures 4-6 *for well locations.*

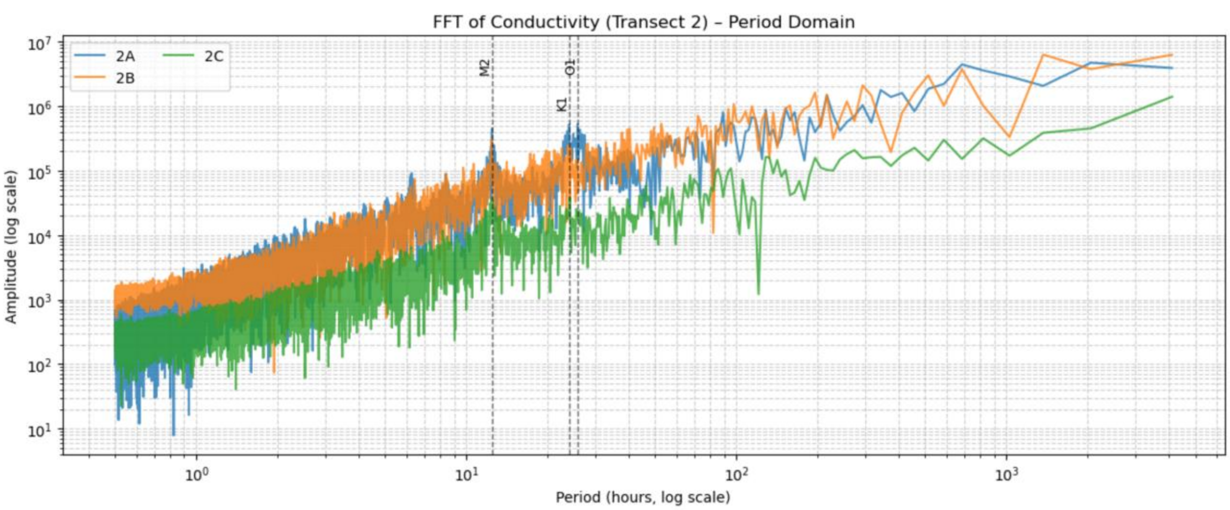

Figure 40). *Results of frequency domain (Fourier) analysis (spectral density vs. period) of conductivity readings from wells located along Transect 2. Refer to* Figures 4-6 *for well locations.*

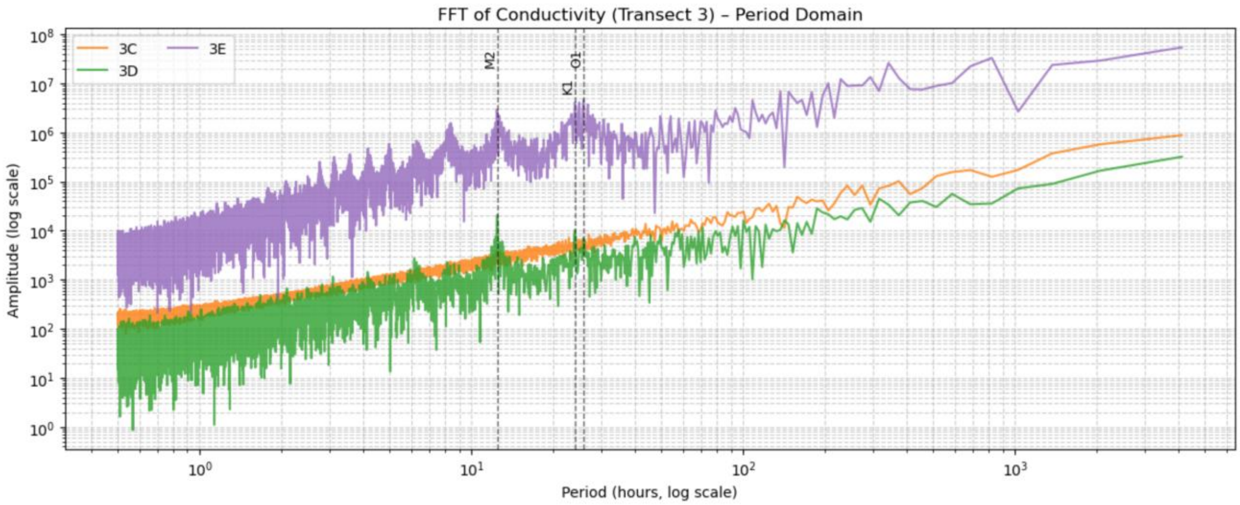

Figure 41). *Results of frequency domain (Fourier) analysis (spectral density vs. period) of conductivity readings from wells located along Transect 3. Refer to Figures 4-6 for well locations.*

Across all wells, conductivity spectra exhibit higher amplitudes than water-level spectra, reflecting the cumulative effects of storage, mixing, and diffusion processes that integrate hydrologic forcing over longer timescales.

Table 8). *Dominant Water Level and Electrical Conductivity Periods in Each Well.*

Well	Geomorphic Unit	Dominant Well Water Level Periods (hrs)	Dominant Well Water Level Periods (Days)	Dominant Well Conductivity Period (hrs)	Dominant Well Conductivity Period (Days)
1C	Dunes	1653.58	68.9	2050.62	85.44
1D	Ocean Coast	12.40	0.52	818.05	34.09
1F	Vegetated Flats	1653.42	68.89	1025.19	42.72
2A	Vegetated Flats	95.50	3.98	683.83	28.49
2B	Vegetated Flats	1652.42	68.85	1367.50	56.98
2C	Dunes	1652.25	68.84	820.70	34.20
3C	Vegetated Flats	4960.75	206.70	1368.33	57.01
3D	Dunes	1652.75	68/86	684.13	28.51
3E	Sound Coast	12.39	0.52	684.25	28.51

5.3.5 Objective 3 Summary

Temporal groundwater dynamics on Shackleford Banks during the study period were dominated by precipitation-driven recharge, with rapid water-level responses and associated conductivity dilution following major storm events. Tidal influence was detectable but spatially limited to coastal wells and diminished rapidly toward the island interior. Conductivity responses lagged hydraulic responses across all geomorphic settings, indicating that salinity dynamics are governed by storage and mixing processes rather than instantaneous forcing.

6. Discussion

This study provides a process-based evaluation of freshwater availability and salinity dynamics on Shackleford Banks using integrated hydrological monitoring, geophysical surveying, and analytical modeling. Results from all three objectives converge on a consistent finding: freshwater resources on Shackleford Banks are primarily controlled by geomorphology and island geometry, with climatic forcing modulating spatial patterns in groundwater salinity and storage.

6.1 Geomorphic Control on Freshwater Storage and Lens Geometry

Freshwater lens dimensions across Shackleford Banks exhibit a pronounced west-east gradient, with thicker and more voluminous freshwater lenses in the wider, higher-elevation western portion of the island and thinner, more constrained lenses near Barden Inlet. Analytical modeling demonstrates that island width exerts a first-order control on freshwater lens thickness and storage capacity, while recharge and hydraulic conductivity vary over comparatively smaller ranges and does not alter the spatial hierarchy of freshwater availability.

Seasonal and event-driven recharge introduces short-term variability in water-table elevation and freshwater lens thickness, particularly following large storm events. However, these fluctuations occur within geomorphologically imposed bounds. Wider island segments accommodate larger absolute changes in freshwater storage, whereas narrower segments respond proportionally but remain fundamentally limited by available accommodation space. This geometry-driven control explains why freshwater lens thinning is most pronounced near the inlet (such as site 3 on the eastern portion of the island), even during periods of elevated recharge.

Although analytical freshwater lens models assume steady-state conditions, time-series observations confirm that the freshwater system on Shackleford Banks is highly transient. Seasonal recharge pulses, storm sequencing, and drought conditions propagate rapidly through the shallow aquifer, producing measurable expansion and contraction of the freshwater lens. Nevertheless, these transient responses do not obscure the dominant spatial pattern imposed by island width.

6.2 Validity and Utility of FD-EMI for Mapping Salinity Patterns

Apparent electrical conductivity measured using FD-EMI proved to be an effective integrative proxy for near-surface salinity when interpreted within a geomorphic and hydrologic framework. Across Shackleford Banks, spatial variability in ECa strongly mirrors groundwater conductivity observations and analytical freshwater lens geometry, indicating that FD-EMI captures meaningful subsurface processes rather than superficial surface effects.

Several factors that can complicate EMI interpretation, such as sediment texture, bulk density, and soil temperature, were relatively uniform across the study area or explicitly corrected during data processing. The remaining variability in ECa is therefore best explained by differences in pore-water salinity and moisture content associated with landscape position and hydrologic connectivity.

Interior dune environments consistently exhibited low ECa values, reflecting fresh groundwater conditions, coarse-grained sediments, and limited moisture retention. In contrast, sound-side environments exhibited persistently high ECa across all seasons and frequencies, indicating chronic saline influence and strong hydraulic connectivity to marine waters. Ocean-facing coasts and vegetated flats occupied intermediate positions, reflecting mixed freshwater and marine influences.

Importantly, these geomorphic contrasts persisted across seasons, demonstrating that spatial structure in salinity patterns is stable, even as absolute conductivity values fluctuate seasonally, likely due to disturbance events that flood the interior with saltwater. Seasonal forcing modulates the magnitude of near-surface salinity but does not reorganize the spatial pattern established by geomorphology. The strongest differentiation among geomorphic units occurred at higher EMI frequencies, indicating that shallow subsurface layers are most sensitive to topographic position, surface inundation, and freshwater flushing.

6.3 Temporal Groundwater Dynamics and Dominant Forcing Mechanisms

Groundwater time-series data reveal that precipitation-driven recharge is the dominant driver of groundwater-level variability across most of Shackleford Banks. All monitored wells exhibited rapid water-level rises following major storm events, followed by gradual recessions during dry periods. These responses were coherent across the island and aligned closely with precipitation timing and magnitude.

In contrast, tidal influence on groundwater dynamics was spatially restricted. Semi-diurnal and diurnal tidal signals were detectable in wells located near the sound and ocean margins, where freshwater lenses are thin and hydraulic connectivity to marine waters is strong. However, tidal signals attenuated rapidly with inland distance and were weak or absent in mid-island and interior dune wells, indicating that tidal forcing plays a secondary role away from marine boundaries.

Electrical conductivity time series exhibited slower and more complex responses than groundwater levels. Conductivity dilution following recharge was evident in interior and central wells but muted or absent in coastal environments, where saline influence remained persistent. This lagged response reflects the influence of storage, mixing, and diffusion processes that integrate hydrologic forcing over longer timescales.

Frequency-domain analysis reinforces this interpretation. Groundwater-level spectra were dominated by low-frequency components associated with seasonal recharge and drought, while conductivity spectra exhibited dominant intermediate-frequency components reflecting episodic mixing, storm-driven flushing, and tidal pumping. The presence of tidal-frequency energy in conductivity records, even where water-level tidal signals were weak, highlights the sensitivity of salinity to short-term exchange processes in hydraulically connected coastal zones.

6.4 Integrated Conceptual Model of Salinity Dynamics

Results from all three objectives support a unified conceptual model in which geomorphology establishes the baseline structure of freshwater availability, while climatic forcing governs short-term variability within that structure. Interior dune systems function as recharge-dominated freshwater reservoirs with thick lenses and limited saline influence. In contrast, sound-side and inlet-adjacent environments are characterized by thin freshwater lenses, elevated salinity, and strong marine connectivity.

FD-EMI provides an effective spatial bridge between point-based groundwater observations and island-scale hydrologic interpretation, capturing salinity gradients that align with both analytical models and time-series behavior. Together, these methods reveal a barrier island groundwater system that is highly responsive to storms and drought yet fundamentally constrained by island geometry.

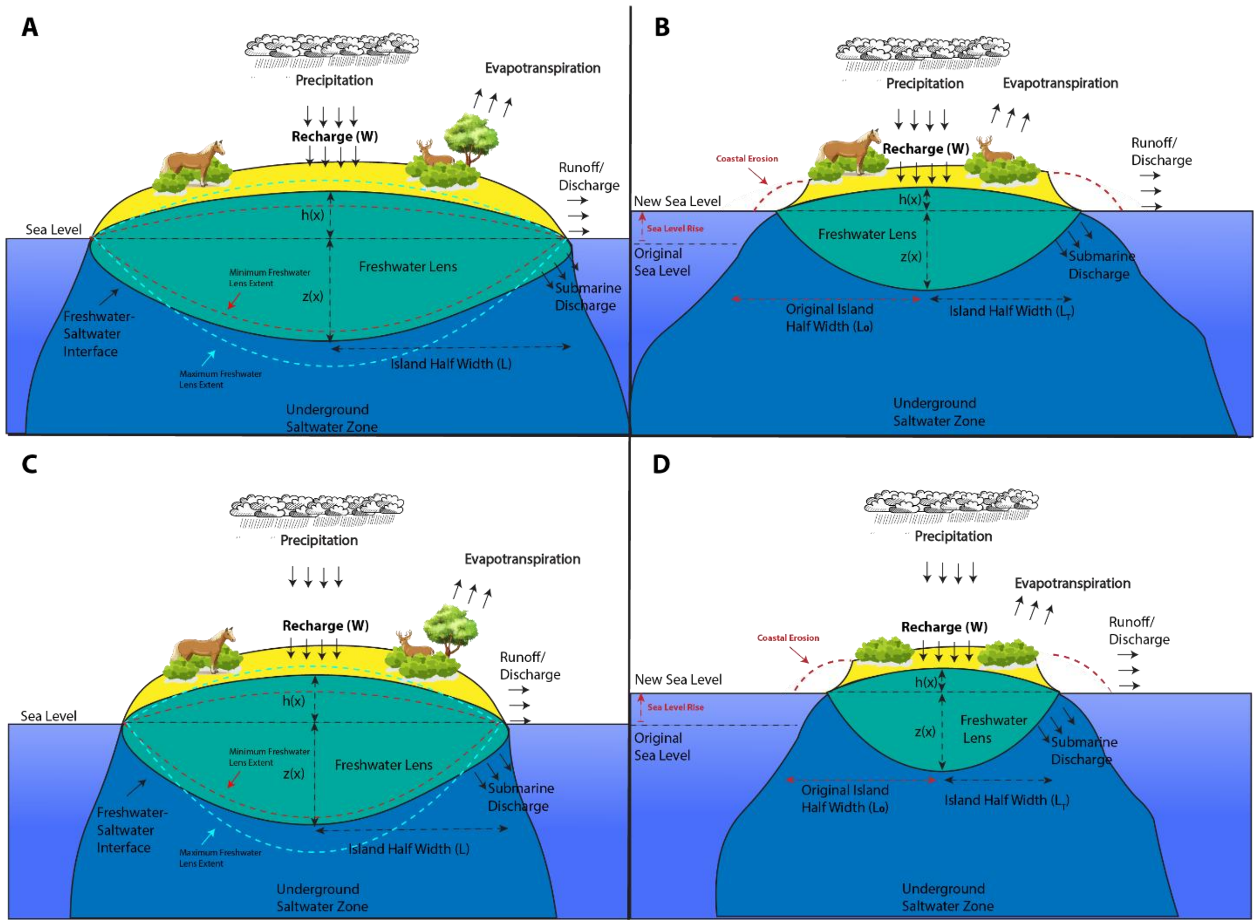

Figure 42). *Conceptual model of the hydrogeology of Shackleford Banks.* ***A)*** *A generalized model of the Shackleford Bank's freshwater lens at its widest point.* ***B)*** *A generalized model of how sea level rise and coastal erosion will affect freshwater lens thickness and volume at the island's widest point.* ***C)*** *A generalized mode of Shackleford Bank's freshwater lens at its narrowest point.* ***D)*** *A generalized model of how sea level rise and coastal erosion will affect freshwater lens thickness and volume at its narrowest point.*

6.5 Implications for Sea-Level Rise and Coastal Change

Sea-level rise projections for the Beaufort, North Carolina region (the closest long-term tide gauge to Shackleford Banks) span a wide range of plausible outcomes through the end of the century (Figure 43). Projected sea-level rise and associated coastal erosion pose a direct threat to freshwater resources on Shackleford Banks by reducing island width, elevating groundwater tables, and increasing the frequency of marine inundation (Figures 42 & 43). Even moderate shoreline retreat will preferentially impact the narrow eastern portion of the island, where freshwater lenses are already thin and hydraulically vulnerable (Figure 44).

As island width decreases, the freshwater lens will experience progressive "squeezing" between rising marine heads and reduced accommodation space, leading to decreased storage capacity and enhanced salinity intrusion. Under these conditions, seasonal recharge pulses will need to offset not only evaporative losses but also increasing marine influence to maintain freshwater quality.

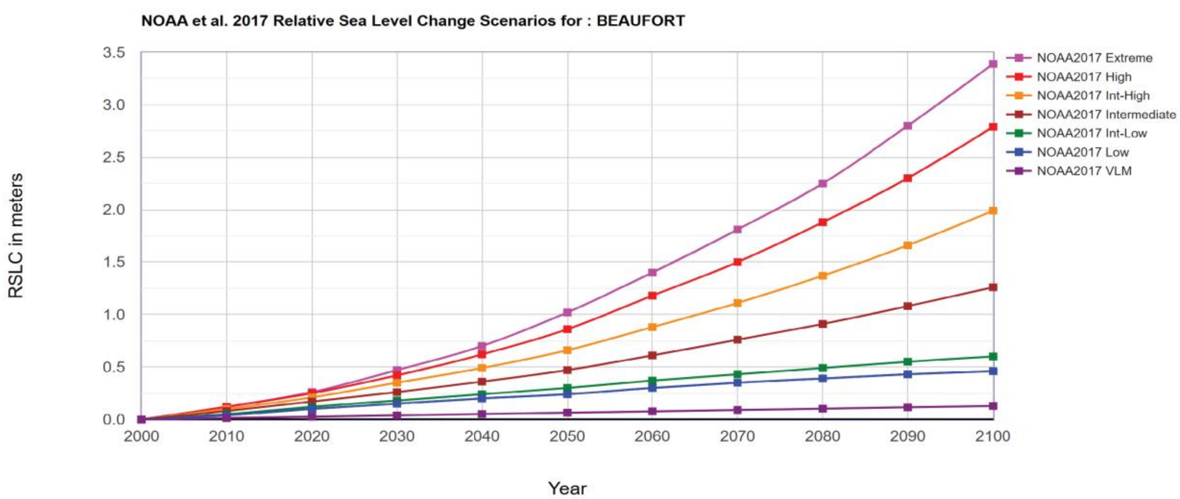

Figure 43). *Relative sea level change scenarios through the end of the century at Beaufort NC (NOAA, 2017).*

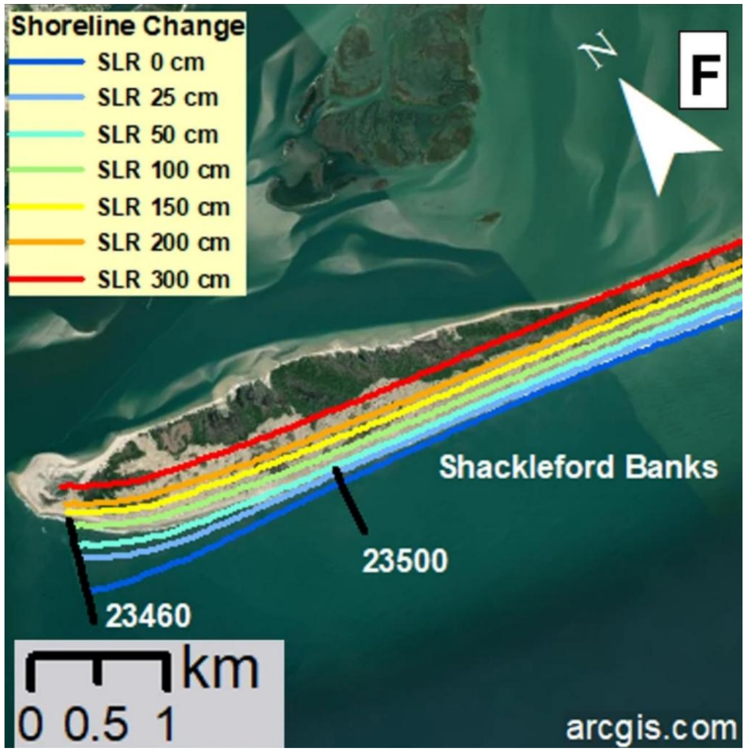

Figure 44). *Modeled shoreline change projections overlayed onto maps of western Shackleford Banks. Figure altered from Thomas (2024).*

The combined use of groundwater monitoring and FD-EMI surveys offers a powerful framework for detecting early shifts in salinity regimes associated with sea-level rise and geomorphic change. Repeated EMI surveys, in particular, provide a spatially efficient means of tracking freshwater vulnerability across undeveloped barrier islands where traditional monitoring infrastructure is limited.

6.6 Study Limitations and Future Monitoring Considerations

This study represents a one-year snapshot of groundwater and salinity dynamics under specific climatic conditions. Longer-term monitoring would improve characterization of interannual variability and extreme-event sequencing. Analytical freshwater lens models provide first-order estimates but do not capture transient three-dimensional flow processes or density-dependent mixing.

Despite these limitations, the strong convergence among independent datasets supports the robustness of the primary conclusions. Future work integrating numerical modeling, expanded monitoring networks, and repeated geophysical surveys would further refine understanding of freshwater resilience under accelerating coastal change.

7. Conclusion

This study provides a process-based assessment of freshwater lens geometry and salinity dynamics on Shackleford Banks, an undeveloped barrier island system along the North Carolina coast. By integrating analytical freshwater lens modeling, groundwater-level and conductivity monitoring, frequency-domain electromagnetic induction (FD-EMI) surveys, and geospatial analysis, this work establishes a baseline understanding of how geomorphology, recharge, and marine forcing interact to control freshwater availability in a dynamic coastal environment.

Results demonstrate that island geomorphology, particularly island width , is the dominant control on freshwater lens thickness and storage capacity. Analytical modeling shows a systematic decrease in freshwater lens thickness and volume from west to east across the island, with wider interior dune systems supporting thicker and more resilient freshwater lenses, and narrower inlet-adjacent regions exhibiting thin, hydraulically vulnerable lenses. Seasonal and event-driven recharge introduces short-term variability in freshwater lens dimensions but does not override the spatial pattern imposed by island geometry.

FD-EMI surveys reveal persistent spatial organization of near-surface salinity patterns, with apparent electrical conductivity strongly structured by geomorphic setting. Interior dune environments consistently exhibit low conductivity indicative of fresh groundwater conditions, while sound-side and ocean-adjacent environments show elevated conductivity reflecting chronic marine influence. Although seasonal forcing modulates conductivity magnitude, particularly during summer months, the relative ranking of geomorphic units remains stable, indicating that spatial salinity patterns are not transient artifacts of individual surveys but reflect underlying hydrologic connectivity and freshwater lens structure. However, episodic storm-surge flooding and overwash events have the potential to locally modify these patterns by introducing saline water into previously fresh environments. Such events may produce longer-term salinity anomalies that persist beyond individual survey periods and represent an important mechanism for localized departures from the broader geomorphically controlled conductivity structure.

Groundwater time-series analyses further demonstrate that precipitation-driven recharge is the primary driver of groundwater-level variability across most of the island, while tidal influence is spatially limited to wells located near marine boundaries. Interior wells remain recharge-dominated and persistently fresh even during drought conditions, whereas coastal wells exhibit elevated salinity and greater sensitivity to tidal and storm-driven exchange. Frequency-domain analyses reinforce this distinction, showing that groundwater levels primarily respond to low-frequency, seasonal-scale forcing, while salinity dynamics reflect shorter-term mixing, storage, and exchange processes.

Together, these findings support an integrated conceptual model in which geomorphology establishes the baseline framework for freshwater availability, and climatic forcing governs variability within that framework. FD-EMI surveys provide an effective spatial bridge between point-based groundwater measurements and island-scale freshwater vulnerability, offering a practical tool for monitoring salinity dynamics in remote, undeveloped barrier island systems.

This study represents a one-year observational record and therefore captures freshwater system behavior under a specific set of climatic conditions. Longer-term monitoring would improve characterization of interannual variability and extreme-event sequencing, while additional geophysical methods could further refine subsurface salinity resolution. Nevertheless, the strong convergence among analytical modeling, geophysical surveys, and groundwater observations supports the robustness of the primary conclusions.

As sea level continues to rise and coastal erosion accelerates, freshwater lenses on barrier islands such as Shackleford Banks are likely to experience progressive thinning, increased salinity intrusion, and reduced storage capacity, particularly in narrow island segments. The baseline established by this study provides a critical reference point for detecting future change and highlights the importance of integrated hydrologic and geophysical monitoring for managing freshwater resources that support sensitive coastal ecosystems and dependent wildlife.

References

Abdelrehim R, Mohamed Ahmed, Mark E. Everett. (2025). Hydrogeologic controls on barrier island geomorphology: Insights from electromagnetic surveys. *Hydrology*; 661. doi: https://10.1016/j.jhydrol.2025.133627

Boaga, J. (2017) The use of FDEM in hydrogeophysics: A review: Journal of Applied Geophysics, v. 139, p. 36-46, https://doi.org/10.1016/j.jappgeo.2017.02.011.

Bracewell, R. N. (2000). The Fourier Transform & Its Applications. McGraw-Hill, 3rd edition.

Brock, J.C., Krabill, W.B., & Sallenger, A.H. (2004). *Barrier island morphologic classification based on LiDAR metrics for north Assateague Island, Maryland. Journal of Coastal Research*, 20(2), 498–509. https://doi.org/10.2112/1551-5036(2004)020[0498:BIMCBO]2.0.CO;2

Cantelon, J. A., Guimond, J. A., Robinson, C. E., Michael, H. A., & Kurylyk, B. L. **(**2022**)**. Vertical saltwater intrusion in coastal aquifers driven by episodic flooding: A review. Water Re**source**s Research, 58, e2022WR032614. https://doi.org/10.1029/2022WR032614

Cantelon, J. A., LeRoux, N. K., Mulligan, R. P., Swatridge, L., & Kurylyk, B. L. **(**2024**)**. Interrelated coastal flooding, erosion, and groundwater salinization on a barrier island during Hurricane Fiona. *Journal of Geophysical Research: Earth Surface*, 129, e2023JF007551. https://doi.org/10.1029/2023JF007551

Cantelon, J. A., Robinson, C. E., & Kurylyk, B. L. **(**2023**)**. Morphologic, atmospheric, and oceanic drivers cause multi-temporal saltwater intrusion on a remote, sand island. Water Resources Research, 59, e2023WR035820. https://doi.org/10.1029/2023WR035820

Chesnaux R (2016). Closed-form analytical solutions for assessing the consequences of sea-level rise on unconfined sloping island aquifers. Glob Planet Chang 139:109–115

Chesnaux, R., Marion, D., Boumaiza, L. *et al.* (2021). An analytical methodology to estimate the changes in fresh groundwater resources with sea-level rise and coastal erosion in strip-island unconfined aquifers: illustration with Savary Island, Canada. *Hydrogeology J* 29, 1355–1364. https://doi.org/10.1007/s10040-020-02300-0

Collenteur, R.A. (2025). gwtf: Python implementation of the Water Table Fluctuation (WTF) Method. Zenodo. https://doi.org/10.5281/zenodo.XXXXXXX

Correll, M.D., Elphick, C.S., Hantson, W. *et al.* (2019). A multi-scale comparison of elevation measurement methods in northeastern tidal marshes of the United States. *Wetlands* **39**, 633–643. https://doi.org/10.1007/s13157-018-1110-x

Corwin, D. L. (2005). Geospatial measurements of apparent soil electrical conductivity for characterizing soil spatial variability. In J. Álvarez-Benedí & R. Muñoz-Carpena (Eds.), *Soil-water-solute characterization: An integrated approach* (pp. 640–672). Boca Raton, FL: CRC Press.

Crosbie, R. S., Binning, P. J., & Kalma, J. D. (2005). A time series approach to inferring groundwater recharge using the water table fluctuation method. *Water Resources Research*, *41*, W01008/1-9. https://doi.org/10.1029/2004WR003077

Dean, W. E. Jr. (1974). Determination of carbonate and organic matter in calcareous sediments and sedimentary rocks by loss on ignition: Comparison with other methods. *Journal of Sedimentary Research*, 44(1), 242–248. https://doi.org/10.1306/74D729D2-2B21-11D7-8648000102C1865D

Devlin, J.F. (2015). HydrogeoSieveXL: an Excel-based tool to estimate hydraulic conductivity from grain-size analysis. *Hydrogeology J* 23, 837–844. https://doi.org/10.1007/s10040-015-1255-0

Eaton, T.T., 2020. Episodic and continuous recharge estimation from high-resolution well records. Groundwater 58 (4), 511–523. https://doi.org/10.1111/gwat.12950.

El-Mowafy, A. (2012). Precise Real-Time Positioning Using Network RTK. InTech. doi: 10.5772/29502

Fetter, C.W. (2001) Applied Hydrogeology. 4th Edition, Prentice Hall, Upper Saddle River.

Fetter, C. W. (1972). Position of the saline water interface beneath oceanic islands. *Water Resources Research*, 8(5), 1307–1315. https://doi.org/10.1029/WR008i005p01307

Fiori, N. Anderson jr., W. **(**2022**)**. The impact of sea-level rise on saltwater intrusion for barrier-island aquifers in North Carolina. Continental Shelf Research. https://doi.org/10.1016/j.csr.2022.104789

Freeze, R.A., Cherry, J.A. 1979. Groundwater. Prentice Hall, Englewood Cliffs, New Jersey.

Friedman, S. P. (2005) Soil properties influencing apparent electrical conductivity: a review/ *Computers and Electronics in Agriculture,* v. 46, p. 45-70. https://doi.org/10.1016/j.compag.2004.11.001.

Geophex Ltd. (2015). Gem-2 – How it works – Detailed – geophex.com. Retrieved from https://geophex.com/gem-2-how-it-works-detailed/

Ghyben, W. B. (1888). *Nota in verband met de voorgenomen putboring nabij Amsterdam* [Note on the probable results of well drilling near Amsterdam]. Unpublished manuscript, Royal Institute of Engineers, The Hague, Netherlands.

Haehnel, P., Rasmussen, T. C., and Rau, G. C. (2024) Technical note: Removing dynamic sea-level influences from groundwater-level measurements, *Hydrology and Earth System Science*., 28, 2767–2784, https://doi.org/10.5194/hess-28-2767-2024

Hazen, A. (1892). *Some physical properties of sands and gravels, with special reference to their use in filtration*. **Massachusetts State Board of Health Annual Report, 24**, 539–556.

Healy, R.W., Cook, P.G. (2002). Using groundwater levels to estimate recharge. *Hydrogeology Journal* **10**, 91–109. https://doi.org/10.1007/s10040-001-0178-0

Healy, R. W., & Scanlon, B. R. (2010). *Estimating Groundwater Recharge*. Cambridge: Cambridge University Press.

Heath, R. C. (1994). Ground-Water Recharge in North Carolina. Groundwater Section Division of Environmental Management North Carolina Department of Environment, Health, and Natural Resources. Ground-Water Recharge in North Carolina

Heiri, O., Lotter, A. F., & Lemcke, G. (2001). Loss on ignition as a method for estimating organic and carbonate content in sediments: Reproducibility and comparability of results. *Journal of Paleolimnology*, 25(1), 101–110. https://doi.org/10.1023/A:1008119611481

Heppner, C. S., & Nimmo, J. R. (2005). A computer program for predicting recharge with a master recession curve (Scientific Investigations Report 2005–5172). U.S. Geological Survey. https://doi.org/10.3133/sir20055172

Heron, S. D. Jr., Moslow, T. F., Berelson, W. M., Herbert, J. R., Steele, G. A., IIISusman, K. R. (1984). Holocene sedimentation of a wave-dominated barrier-island shoreline: Cape Lookout, North Carolina. Hydrodynamics and Sedimentation in Wave-Dominated

Coastal Environments. *Marine Geology.* 60, 413–434. https://doi.org/10.1016/0025-3227(84)90160-9

Herzberg, A. (1901). *Die Wasserversorgung einiger Nordseebäder* [The water supply of several North Sea resorts]. Journal für Gasbeleuchtung und Wasserversorgung, 44, 815–819.

Hiscock, K. M., Bense, V. F. (2021). Hydrogeology: Principles and practice (3rd ed.). Wiley-Blackwell.

Housego, R., Raubenheimer, B., Elgar, S., Cross, S., Legner, C., & Ryan, D. (2021). Coastal flooding generated by ocean wave- and surge-driven groundwater fluctuations on a sandy barrier island. Journal of Hydrology, 603, 126920. https://doi.org/10.1016/j.jhydrol.2021.126920

Huber, P. J., & Ronchetti, E. M. (2009). Robust statistics. New York, NY: Wiley.

Kooi, H., Groen, J., & Leijnse, A. (2000). Modes of seawater intrusion during transgressions. Water Resources Research, 36(12), 3581–3589. https://doi.org/10.1029/2000WR900243

Kurylyk, B. L., Lin, Y., Cristina Solórzano-Rivas, S., Werner, A. D. (2024). Analytical methodology for determining the extent of pumped freshwater lenses in recharge-limited, circular islands, *Advances in Water Resources*, Volume 187, 104692. https://doi.org/10.1016/j.advwatres.2024.104692.

Mariotti, G., Hein, C.J. (2022). Lag in response of coastal barrier-island retreat to sea-level rise. *Nat. Geosci.* **15**, 633–638. https://doi.org/10.1038/s41561-022-00980-9

Maronna, R. A., Martin, R. D., Yohai, V. J., & Salibián-Barrera, M. (2019). Robust statistics: Theory and methods (with R). New York, NY: Wiley.

Masterson, J.P., Fienen, M.N., Thieler, E.R., Gesch, D.B., Gutierrez, B.T. and Plant, N.G. (2014), Effects of sea-level rise on barrier island groundwater system dynamics –

ecohydrological implications. *Ecohydrol*., 7: 1064-1071.
https://doi.org/10.1002/eco.1442

McKinney R, Hanson A, Johnson R, Charpentier M. (2019) Seasonal variation in apparent conductivity and soil salinity at two Narragansett Bay, RI salt marshes. PeerJ. Nov 27;7:e8074. doi: 10.7717/peerj.8074. PMID: 31799073; PMCID: PMC6884989.

McNeill, J. D., (1994). Principles and applications of time domain electromagnetic techniques for resistivity sounding: Geonics Ltd. Technical Note TN-27, 15 p

Mew, H. E., Hirth, D. K., Daniels, R. B., Keyworth, A. J. (2002). Methodology for compiling ground-water recharge maps in the Piedmont and Coastal Plain provinces of North Carolina: Internal report. https://digital.ncdcr.gov/Documents/Detail/methodology-for-compiling-ground-water-recharge-maps-in-the-piedmont-and-coastal-plain-provinces-of-north-carolina-internal-report/3692472

Moslow, T.F., Heron Jr, S.D., (1989). Outer Banks depositional systems, North Carolina: Amer. Geophysics. Union, Field Trip Guidebook T171, 28 the International Geological Congress, 28 pp.

Morris, D.A. and A.I. Johnson, 1967. Summary of hydrologic and physical properties of rock and soil materials as analyzed by the Hydrologic Laboratory of the U.S. Geological Survey, U.S. Geological Survey Water-Supply Paper 1839-D, 42p.

NC OneMap (2019). North Carolina Department of Information Technology, Government Data Analytics Center, Center for Geographic Information and Analysis. Available at www.nconemap.gov.

Nielsen, L., Moller, I., Nielsen, L.H., Johannessen, P.N., Pejrup, M., Anderson, T.J., Korshoj, J.S. (2009). Integrating ground-penetrating radar and borehole data from a Wadden Sea barrier island. *Journal of Applied Geophysics* 68 (2009) 47–59. https://doi.org/10.1016/j.jappgeo.2009.01.002

Nimmo, J.R., Horowitz, C., Mitchell, L., (2015). Discrete-storm water-table fluctuation method to estimate episodic recharge. Groundwater 53 (2), 282–292. https://doi.org/10.1111/gwat.12177.

NOAA. **(**2017**)**. Global and Regional Sea Level Rise Scenarios for the United States. NOAA Technical Report. NOS CO-OPS 083. Retrieved from CO-OPS Technical Report (noaa.gov)

NOAA. (2022). Global and Regional Sea Level Rise Scenarios for the United States: Updated Mean Projections and Extreme Water Level Probabilities Along U.S. Coastlines. NOAA Technical Report. Retrieved from Global and Regional Sea Level Rise Scenarios for the United States (windows.net)

North Carolina State Climate Office, NC State University. (2024). Cardinal [data retrieval interface] available at https://products.climate.ncsu.edu/cardinal/request. Accessed June 01, 2024.

O'Connell MJ, Shugart HH, Okin GS. **(**2012**)** Measurement and monitoring of barrier island forest sensitivity to ecohydrological change using LIDAR remote sensing. *Journal of Coastal Research* 28: 793–810.

Office of Coast Survey, 2025: Vertical Datum Transformation, https://www.fisheries.noaa.gov/inport/item/39987

Paine, J., White, W., Smyth, R., Andrews, J., Gibeaut, J. (2005). Combining Em and Lidar To Map Coastal Wetlands: An Example From Mustang Island, Texas. European Association of Geoscientists & Engineers. https://doi.org/10.3997/2214-4609-pdb.183.745-756

Paldor, A., Frederiks, R. S., & Michael, H. A. (2022). Dynamic steady state in coastal aquifers is driven by multi-scale cyclical processes, controlled by aquifer storativity. *Geophysical Research Letters*, 49, e2022GL098599. https://doi.org/10.1029/2022GL098599

Panthi, J., Boving, T., Pradhanag, S., Russoniello, C., Kang, S. **(**2024**)**. The contraction of freshwater lenses in barrier island: A combined geophysical and numerical analysis. Journal of Hydrology, 637, https://doi.org/10.1016/j.jhydrol.2024.131371

Parsekian, A. D., K. Singha, B. J. Minsley, W. S. Holbrook, and L. Slater **(**2015**)**, Multiscale geophysical imaging of the critical zone. Rev. Geophys., 53, 1–26. doi: 10.1002/2014RG000465.

Rawls, W.J., Nemes, A., Pachepsky Ya. (2004) Effect of soil organic carbon on soil hydraulic properties, *Developments in Soil Science, v.* 30, p. 95-114 https://doi.org/10.1016/S0166-2481(04)30006-1.

Riggs, S. R., Ames, D. V., Mallinson, D. J. (2015). Environmental and geological evolution of Shackleford Banks, Cape Lookout National Seashore North Carolina. A report to NPS. Department of Geological Sciences, East Carolina University, Greenville, North Carolina

Riggs, S. R., Ames, D. V., Mallinson, D. J. (2016). "Updated Chapter: Geological Evolution of Shackleford Banks and Back Sound." Environmental and geological evolution of Shackleford Banks, Cape Lookout National Seashore North Carolina. A report to NPS. Department of Geological Sciences, East Carolina University, Greenville, North Carolina.

Rogers, J.N.; Parrish, C.E.; Ward, L.G., and Burdick, D.M., (2016). Assessment of elevation uncertainty in salt marsh environments using discrete-return and full-waveform lidar. *Journal of Coastal Research*, Special Issue, No. 76, pp. 107–122. doi: https://doi.org/10.2112/SI76-010

Schupp, C. 2017. Cape Lookout National Seashore: Geologic resources inventory report. Natural Resource Report NPS/NRSS/GRD/NRR—2017/1491. National Park Service, Fort Collins, Colorado.

Sheets, K.R. and Hendrickx, J.M.H., (1995). Non-invasive soil water content measurement using electromagnetic induction, Water Resour. Res., 31, 2401–2409.

Sisco, M. S. (2013). Assessing the shallow groundwater system as a potential factor in generating storm-water runoff on a North Carolina barrier island. Master's thesis, East Carolina University. The Scholarship, East Carolina University Institutional Repository. http://hdl.handle.net/10342/4225

Sneddon, I.N. (1951). Fourier Transforms. McGraw-Hill.

Stringer, C.E., Rains, M.C., Kruse, S. *et al.* (2010). Controls on Water Levels and Salinity in a Barrier Island Mangrove, Indian River Lagoon, Florida. *Wetlands* **30**, 725–734. https://doi.org/10.1007/s13157-010-0072-4

Susman, K. R., Heron, D. (1979). Evolution of a barrier island, Shackleford Banks, Carteret County, North Carolina. Geological Society of America Bulletin, v. 90, 205-215.

Thomas, J.A., Barnard, P.L., Vitousek, S. *et al.* The projected exposure and response of a natural barrier island system to climate-driven coastal hazards. *Sci Rep* **14**, 25814 (2024). https://doi.org/10.1038/s41598-024-76749-4

U.S. Salinity Laboratory Staff. 1954. Diagnosis and Improvement of Saline and Alkali Soils, USDA Handbook 60. U.S. Government Printing Office, Washington, DC. p1–160.

Viberg, Andreas. (2012). Remnant Echoes of the Past. Geophysical Archaeological Prospection in Sweden.

Werner, A. D., Bakker, M., Post, V. E. A., Vandenbohede, A., Lu, C., Ataie-Ashtiani, B., et al. (2013). Seawater intrusion processes, investigation, and management: Recent advances and future challenges. Advances in Water Resources, 51, 3–26. https://doi.org/10.1016/j.advwatres.2012.03.004

Woessner, W.W. & Poeter, E.P. (2020). *Hydrogeologic Properties of Earth Materials and Principles of Groundwater Flow*. The Groundwater Project. https://doi.org/10.21083/978-1-7770541-2-0.

Yan, M., Solórzano-Rivas, S.C., Werner, A.D. Lu, C. (2024). Analytical estimation of sea-level rise impacts on the freshwater lenses of elliptical islands with sloping shorelines J. Hydrol., 629 (2024), Article 130511, 10.1016/j.jhydrol.2023.130511

Appendices

Appendix A). Average ECa reading for each geomorphic unit and season by frequency band.

Season	Geomorphic Unit	Frequency Band (Hz)	Mean ECa (mS/m)
winter	Dunes	Econd_63030Hz__mS_m_	6.21
spring	Dunes	Econd_63030Hz__mS_m_	8.14
spring	Dunes	Econd_1530Hz__mS_m_	8.39
winter	Dunes	Econd_18210Hz__mS_m_	11.43
winter	Dunes	Econd_5010Hz__mS_m_	14.21
spring	Dunes	Econd_18210Hz__mS_m_	15.89
spring	Dunes	Econd_5010Hz__mS_m_	18.29
winter	Dunes	Econd_1530Hz__mS_m_	20.69
summer	Dunes	Econd_63030Hz__mS_m_	21.43
spring	Vegetated Flat	Econd_1530Hz__mS_m_	24.89
summer	Dunes	Econd_1530Hz__mS_m_	26.67
summer	Dunes	Econd_18210Hz__mS_m_	28.04
spring	Vegetated Flat	Econd_63030Hz__mS_m_	29.55
winter	Vegetated Flat	Econd_63030Hz__mS_m_	29.66
summer	Dunes	Econd_5010Hz__mS_m_	29.68
winter	Vegetated Flat	Econd_18210Hz__mS_m_	39.62
spring	Vegetated Flat	Econd_18210Hz__mS_m_	40.01
spring	Vegetated Flat	Econd_5010Hz__mS_m_	42.70
winter	Vegetated Flat	Econd_5010Hz__mS_m_	45.76
spring	Vegetated Flat	Econd_450Hz__mS_m_	46.35
winter	Vegetated Flat	Econd_1530Hz__mS_m_	52.49
spring	Dunes	Econd_450Hz__mS_m_	54.72
summer	Vegetated Flat	Econd_63030Hz__mS_m_	62.91
summer	Vegetated Flat	Econd_1530Hz__mS_m_	65.08
summer	Vegetated Flat	Econd_18210Hz__mS_m_	71.31
summer	Vegetated Flat	Econd_5010Hz__mS_m_	72.19
winter	Dunes	Econd_450Hz__mS_m_	84.83
spring	Ocean Coast	Econd_63030Hz__mS_m_	87.63
winter	Ocean Coast	Econd_63030Hz__mS_m_	98.29
summer	Ocean Coast	Econd_63030Hz__mS_m_	113.03
spring	Ocean Coast	Econd_18210Hz__mS_m_	125.04
winter	Vegetated Flat	Econd_450Hz__mS_m_	134.07
spring	Sound Coast	Econd_63030Hz__mS_m_	137.21
winter	Ocean Coast	Econd_18210Hz__mS_m_	137.85
spring	Ocean Coast	Econd_5010Hz__mS_m_	153.65
spring	Sound Coast	Econd_18210Hz__mS_m_	154.55

summer	Dunes	Econd_450Hz__mS_m_	155.14
spring	Ocean Coast	Econd_1530Hz__mS_m_	157.39
summer	Ocean Coast	Econd_18210Hz__mS_m_	162.96
winter	Ocean Coast	Econd_5010Hz__mS_m_	163.54
spring	Sound Coast	Econd_5010Hz__mS_m_	168.162
winter	Ocean Coast	Econd_1530Hz__mS_m_	173.19
spring	Sound Coast	Econd_1530Hz__mS_m_	176.10
summer	Vegetated Flat	Econd_450Hz__mS_m_	181.08
winter	Sound Coast	Econd_1530Hz__mS_m_	188.18
summer	Ocean Coast	Econd_5010Hz__mS_m_	201.29
winter	Sound Coast	Econd_5010Hz__mS_m_	201.56
summer	Ocean Coast	Econd_1530Hz__mS_m_	207.81
spring	Sound Coast	Econd_450Hz__mS_m_	220.90
winter	Sound Coast	Econd_18210Hz__mS_m_	221.94
spring	Ocean Coast	Econd_450Hz__mS_m_	223.50
winter	Sound Coast	Econd_63030Hz__mS_m_	225.26
winter	Sound Coast	Econd_450Hz__mS_m_	235.23
winter	Ocean Coast	Econd_450Hz__mS_m_	253.86
summer	Sound Coast	Econd_63030Hz__mS_m_	336.49
summer	Ocean Coast	Econd_450Hz__mS_m_	340.94
summer	Sound Coast	Econd_5010Hz__mS_m_	344.03
summer	Sound Coast	Econd_1530Hz__mS_m_	346.27
summer	Sound Coast	Econd_18210Hz__mS_m_	354.53
summer	Sound Coast	Econd_450Hz__mS_m_	413.04

Appendix B). Recharge from RISE, MCR, and MCR-BOTH methods from 07/2024-07/2025

Table B1) Recharge results from RISE, MCR, and MCR-BOTH methods from 7.23.24-8.12.25

WELL	Cumulative Precipitation Since Start of Log (m)	Recharge Calculated Using RISE (m)	Recharge Calculated Using MCR-RISE (m)	Recharge Calculated Using MCR-BOTH (m)	Percentage of Precipitation as Recharge - RISE (%)	Percentage of Precipitation as Recharge - MCR-RISE (%)	Percentage of Precipitation as Recharge - MCR-BOTH (%)
1A	0.6732	0.201	0.231	0.231	30	34	34
1B	1.4642	0.483	0.563	0.564	33	38	39
1C	1.4642	0.562	0.647	0.650	38	44	44
1D	0.6732	0.259	0.290	0.293	38	43	44
1E	0.6732	0.316	0.360	0.360	47	53	53
1F	1.4642	0.297	0.337	0.338	20	23	23
2A	1.3804	0.823	0.904	0.904	60	66	66
2B	1.3804	0.716	0.785	0.790	52	57	57
2C	1.3804	0.889	1.012	1.019	64	73	74
3A	0.7719	0.481	0.540	0.540	62	70	70
3C	0.7917	0.501	0.565	0.566	63	71	72
3D	0.7917	0.408	0.444	0.446	52	56	56
3E	0.7457	0.272	0.314	0.314	36	42	42
3F	0.7917	0.352	0.403	0.403	44	51	51

Table B2) Recharge from RISE, MCR, and MCR-BOTH methods from 7.23.24-8.12.25

Site	Average Percentage of Precipitation as Recharge - RISE (%)	Average Percentage of Precipitation as Recharge - MCR-RISE (%)	Average Percentage of Precipitation as Recharge - MCR-BOTH (%)
1	0.34	39	0.40
2	0.59	65	0.66
3	0.52	58	0.58
Total	0.46	52	0.52

Appendix C). Table of samples, median grain size, % organic material if applicable, and K.

Sample #	Median Grain Size (φ)	Organic Material (%)	Hydraulic Conductivity (m/s)
1B (0-0.5')	2.50	4.4	.388E-03
1B (1.5')	2.5	-	.346E-03
1B (2.5')	2.5	-	.343E-03
1B (3.5')	2.5	9.2	.445E-03
1B (4')	2.5	-	.369E-03
1B (5')	2.5	1.8	.373E-03
1B (5.5')	2.5	1.5	.386E-03
1B (6')	2.5	1.6	.386E-03
1B (6.5-7')	2.5	3.0	.358E-03
1B (7-7.5')	2.5	-	.367E-03
1B (8')	2.5	-	.351E-03
1B (8-8.5')	2.5	-	.327E-03
1C 0-1'	2.5	-	.405E-03
1C 1-2'	2.5	-	.389E-03
1C 2-3'	2.5	-	.421E-03
1C 3-4'	2.5	-	.379E-03
1C 4-5'	2.5	-	.418E-03
1D 0-1'	2.5	-	.410E-03
1D 1-2'	2.5	-	.387E-03
1D 2-3'	2.5	-	.410E-03
1D 3-4'	2.5	-	.405E-03
1D 4-5'	2	-	.400E-03
1D 5-6'	2.5	-	.709E-03
1D (6-7')	2.5	-	.478E-03
1E (0-1')	2.5	13.3	.376E-03
1E (1-2')	2.5	6.9	.302E-03
1E (2-3')	2.5	0.9	.334E-03
1F (0-0.5')	2.5	-	.568E-03
1F (0-1')	2	-	.379E-03
1F (1-2')	2.5	-	.490E-03
1F (2-3')	2.5	-	.481E-03
1F (3-4')	2.5	-	.404E-03
1F (4-5')	2.5	-	.432E-03
1F (5-6')	2.5	-	.487E-03
2A (0-1')	2.5	1.1	.400E-03
2A (1-2')	2.5	-	.377E-03
2A (2-3')	2.5	-	.424E-03
2B (0-1')	2.5	1.4	.504E-03
2B (1-2')	2	-	.358E-03
2B (2-3')	2	-	.589E-03
2C 0-1'	2	-	.505E-03

2C 1-2'	2	-	.720E-03
2C 2-3'	2	-	.619E-03
2C 3-4'	2	-	.120E-02
2C 4-5'	2	-	.629E-03
2C 5-6'	2	-	.455E-03
2C 6-7'	2	-	.461E-03
3A (0-1')	2	2.6	.482E-03
3A (1-2')	2	-	.461E-03
3A (2-3')	2	-	.528E-03
3C (0-1')	2	5.9	.668E-03
3C (1-2')	2	-	.761E-03
3C (2-3')	2	-	.797E-03
3D 0-1'	0.5	-	.670E-03
3D 1-2'	1	-	.521E-03
3D 2-3'	1	-	.563E-03
3D 3-4'	2	-	.665E-03
3D 4-5'	2	-	.655E-03
3E (0-1')	2	1.1	.937E-03
3E (1-2')	2	3.1	.698E-03
3E (2-3')	2	1.0	.662E-03
3E (3-4)	2	0.9	.703E-03
3E (4-5')	2	1.5	.618E-03
3F (0-1')	2	-	.499E-03
3F (1-2')	2	-	.575E-03
3F (2-3')	2	-	.826E-03

Appendix D). Induction numbers for the maximum and minimum ECa value of each frequency.

Frequency	Minimum ECa Induction Number	Maximum ECa Induction Number
450	0.00058	0.0899
1530	0.00058	0.00058
5010	0.00056	0.00056
18210	0.00058	0.3111
63030	0.00058	0.5916

Appendix E). Seasonal transect FD-EMI data across all frequency bands.

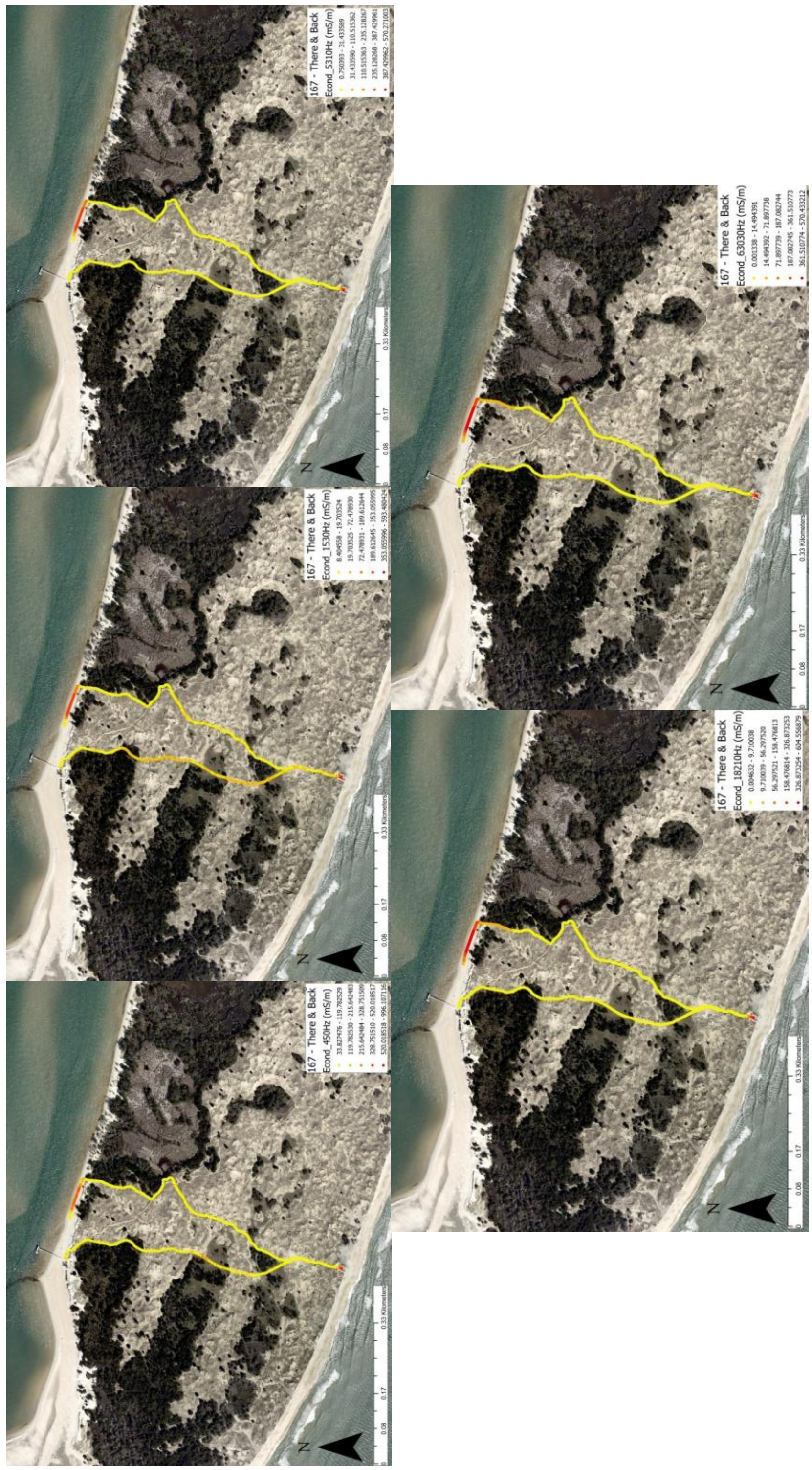

Figure E1). Transect 1 FD-EMI readings during winter.

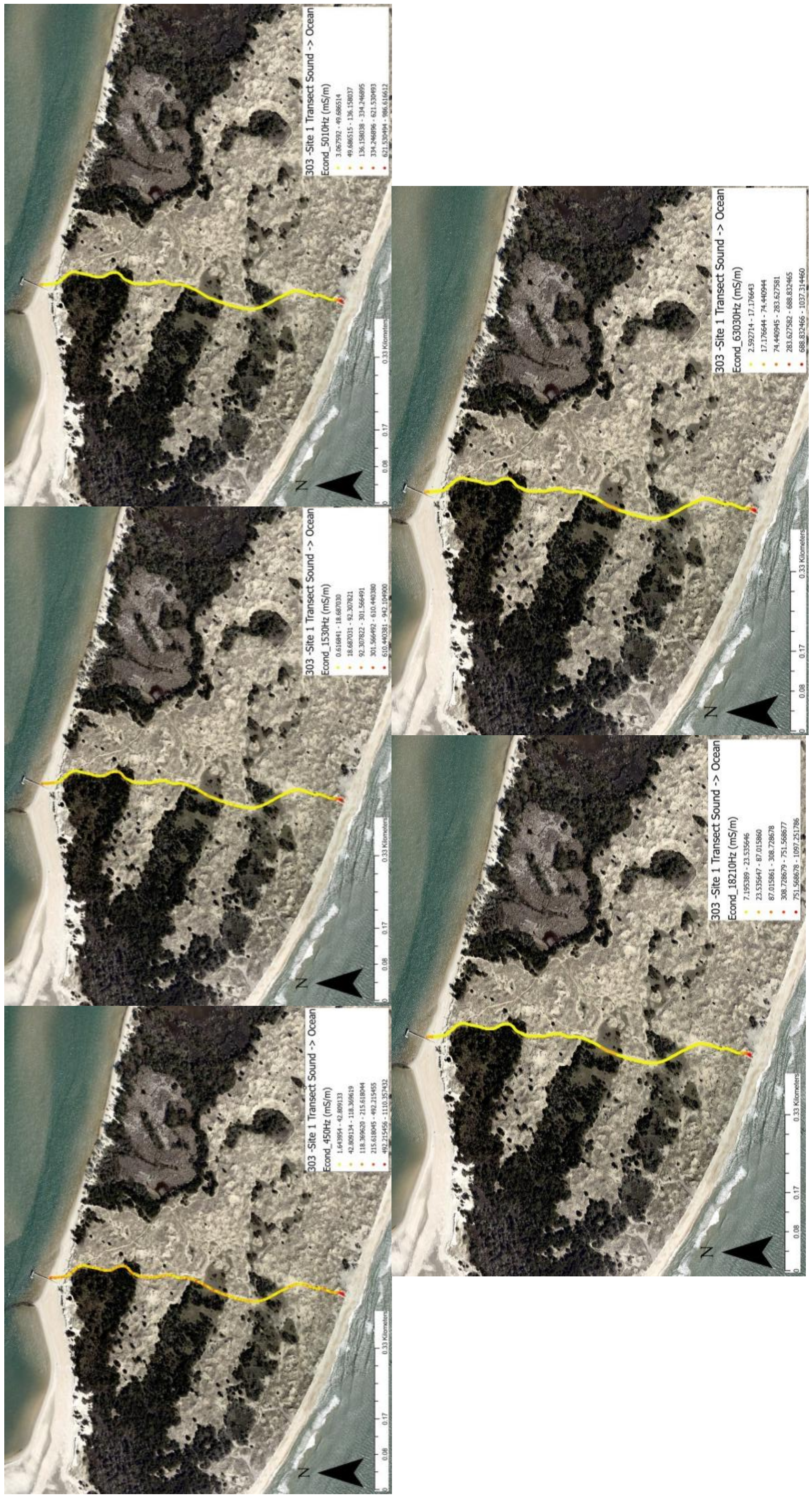

Figure E2). Transect 1 FD-EMI readings during spring.

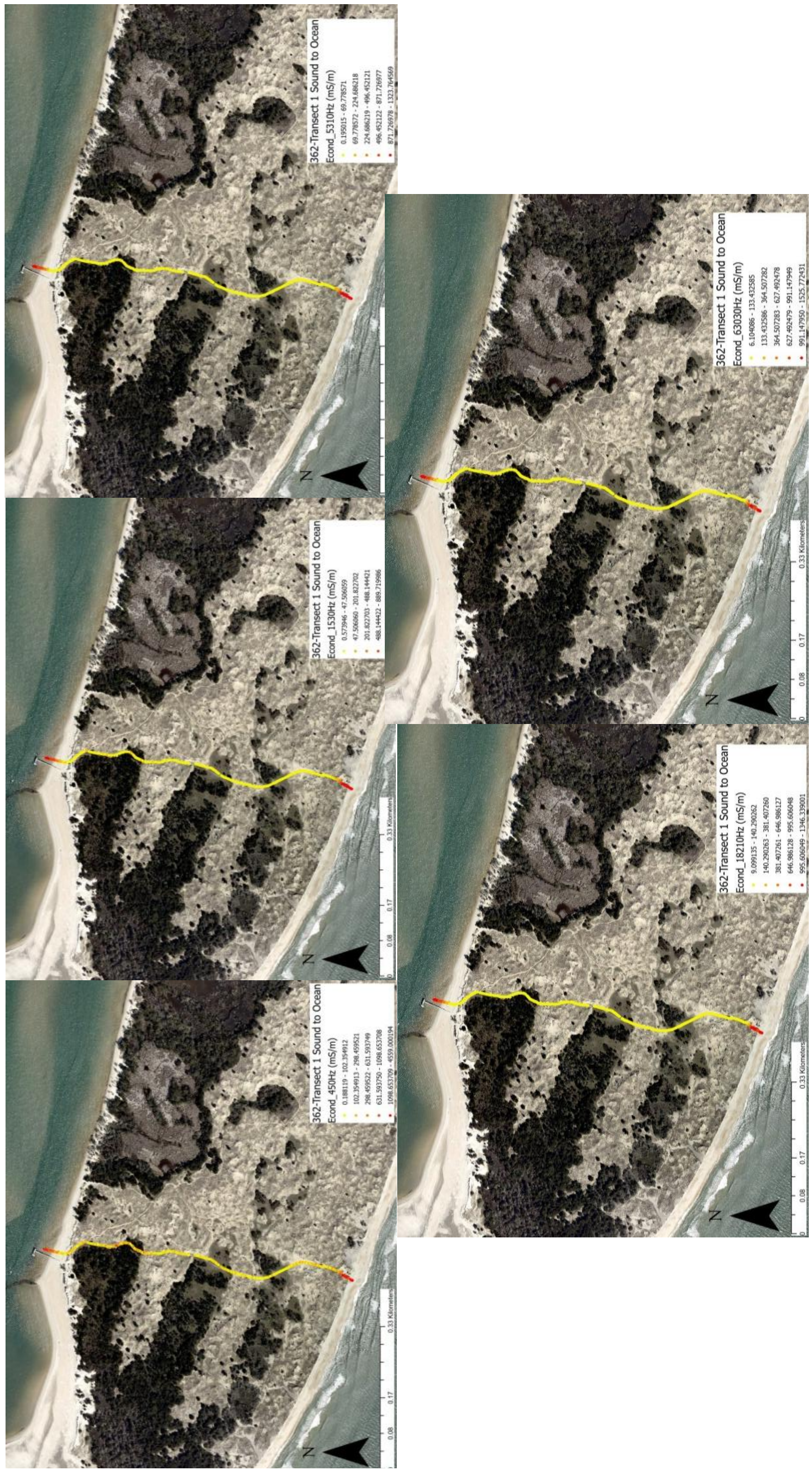

Figure E3). Transect 1 FD-EMI readings during summer.

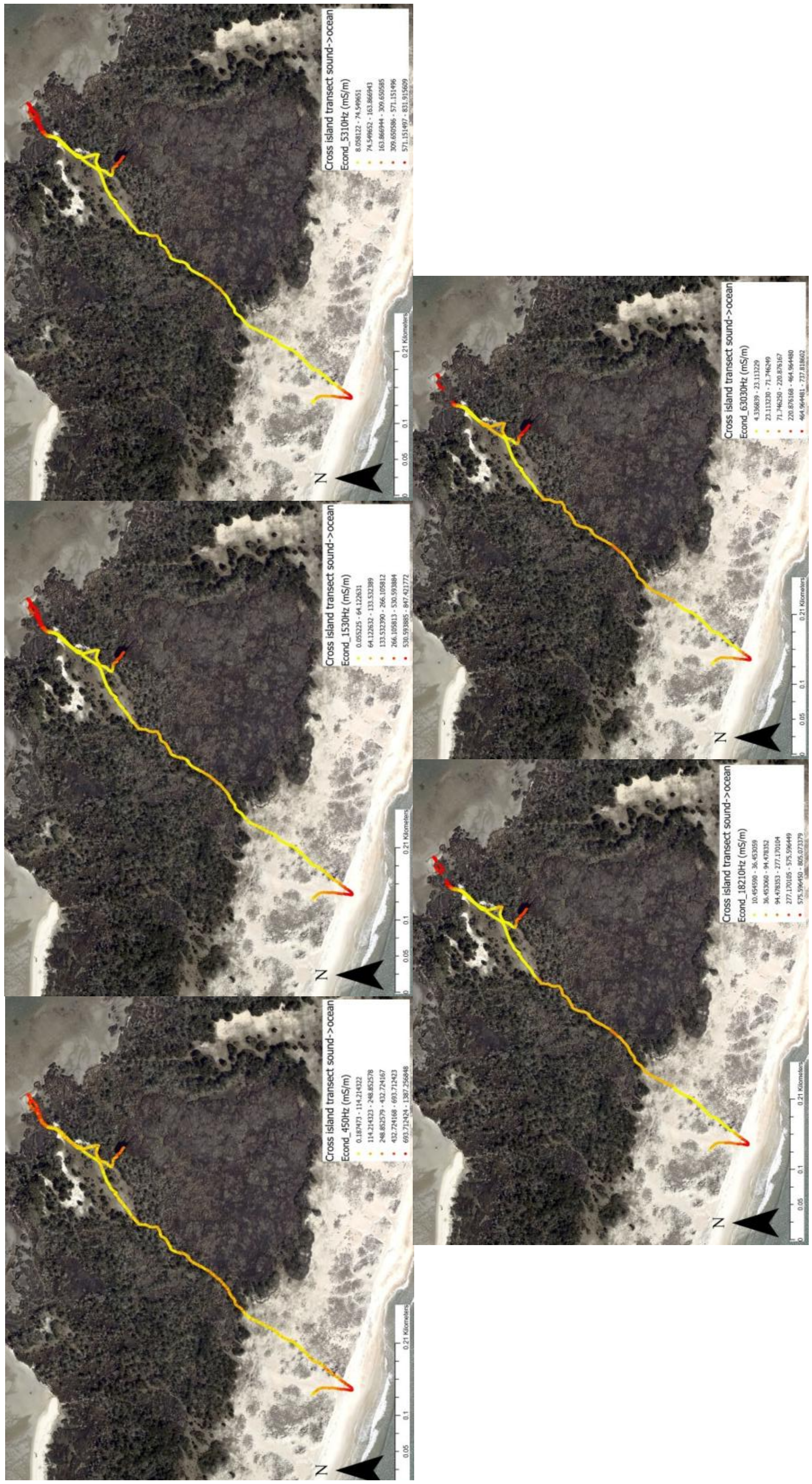

Figure E4). Transect 2 FD-EMI readings during winter.

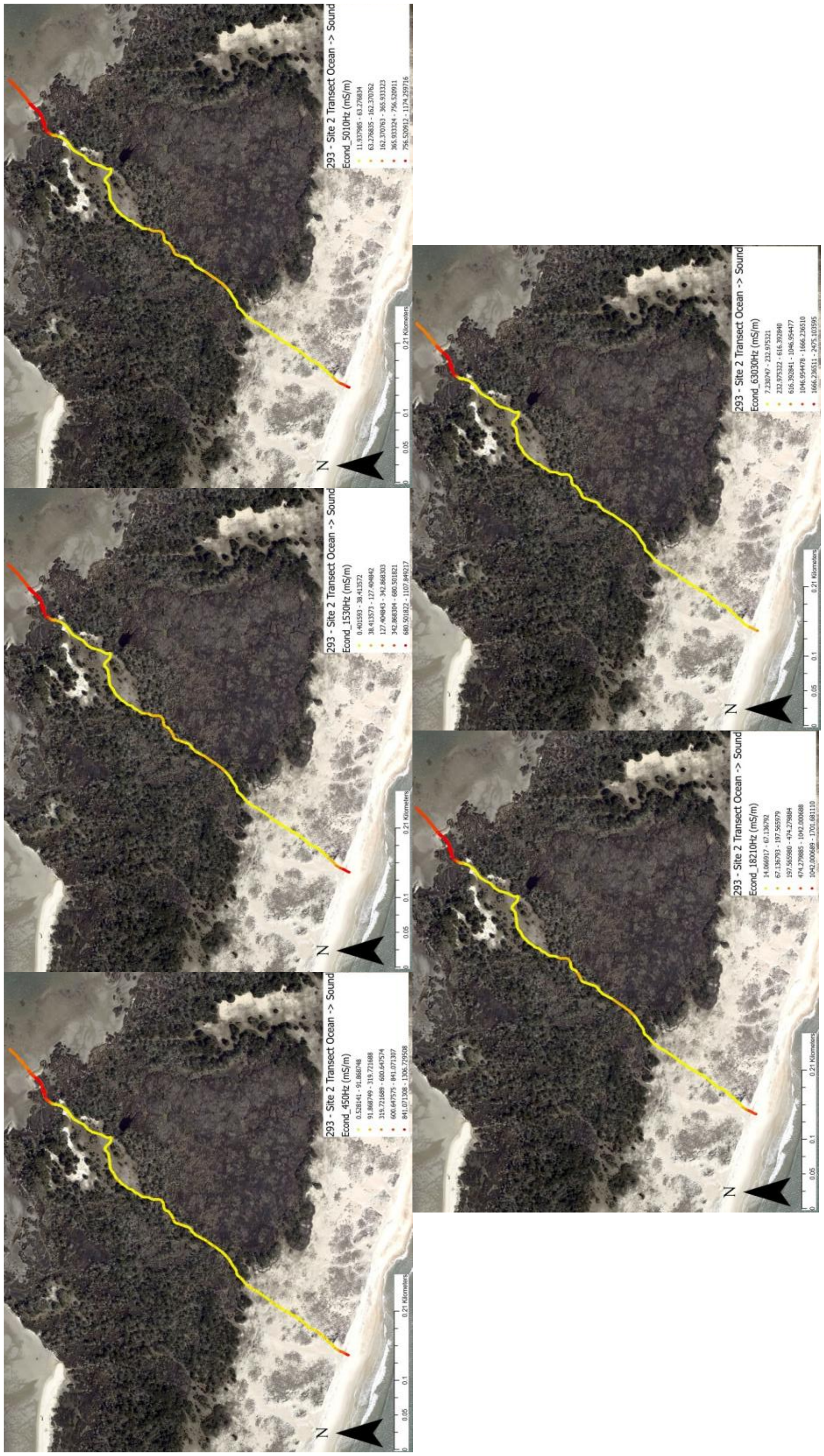

Figure E5). Transect 2 FD-EMI readings during spring.

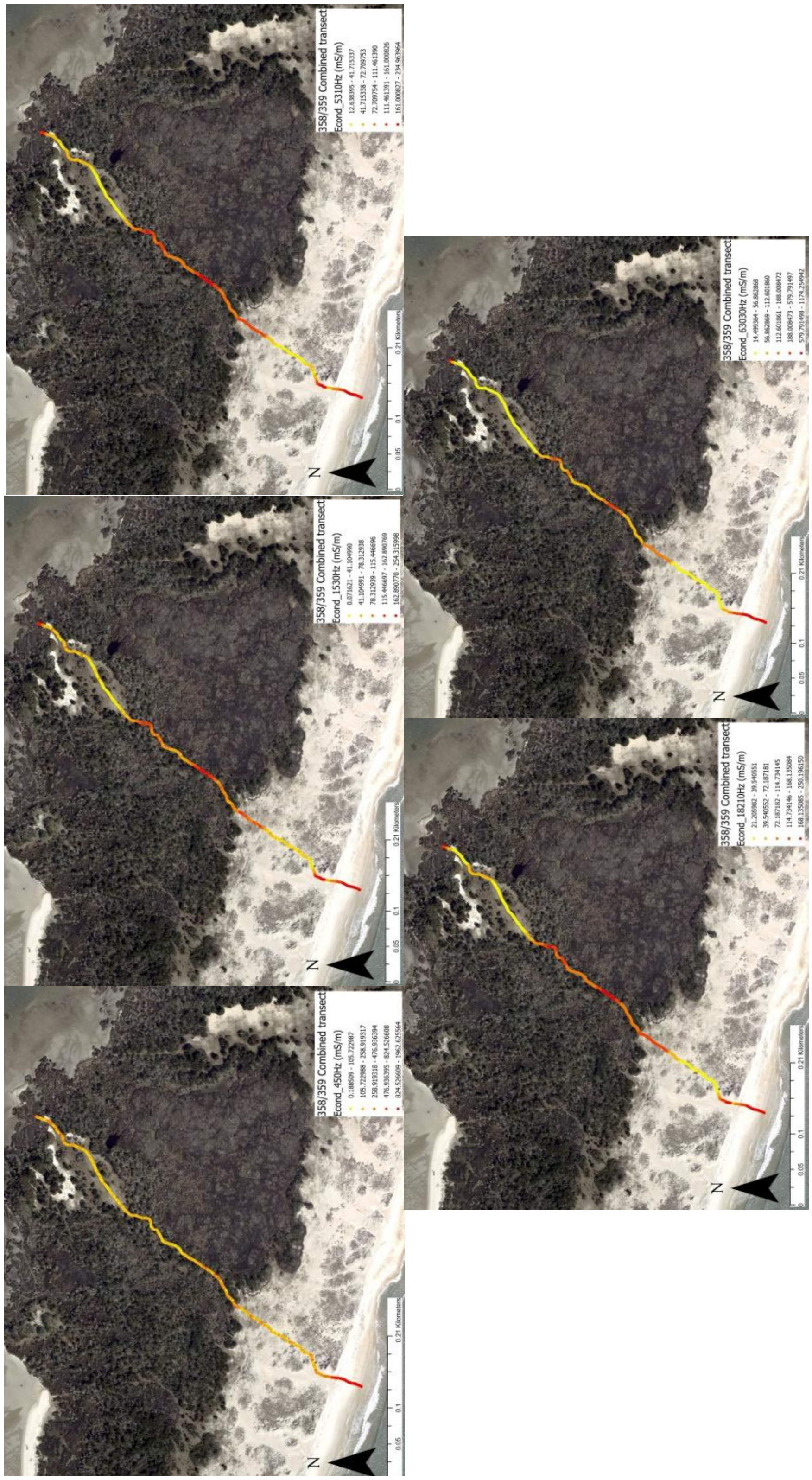

Figure E6). Transect 2 FD-EMI readings during summer.

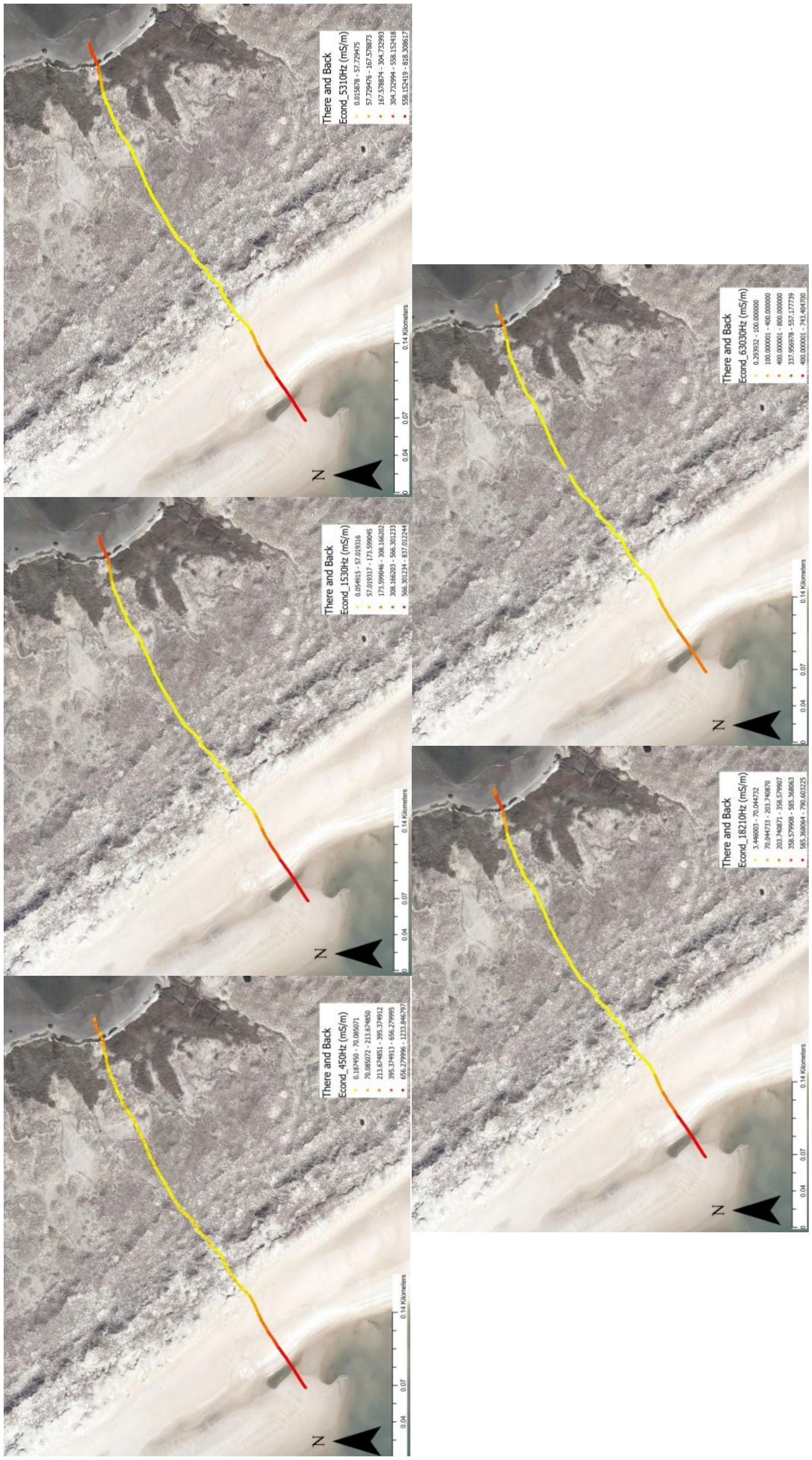

Figure E7). Transect 3 FD-EMI readings during winter.

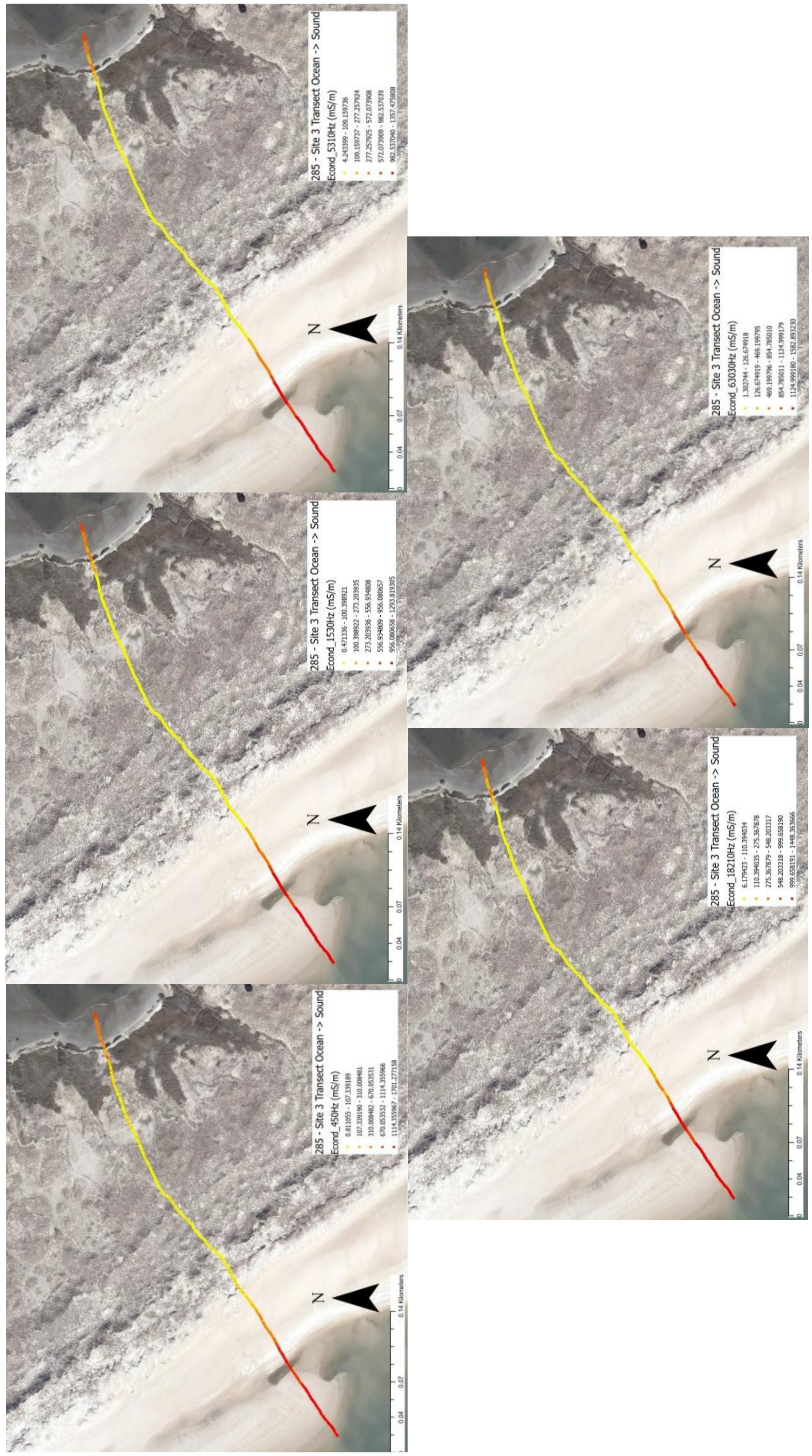

Figure E8). Transect 3 FD-EMI readings during spring.

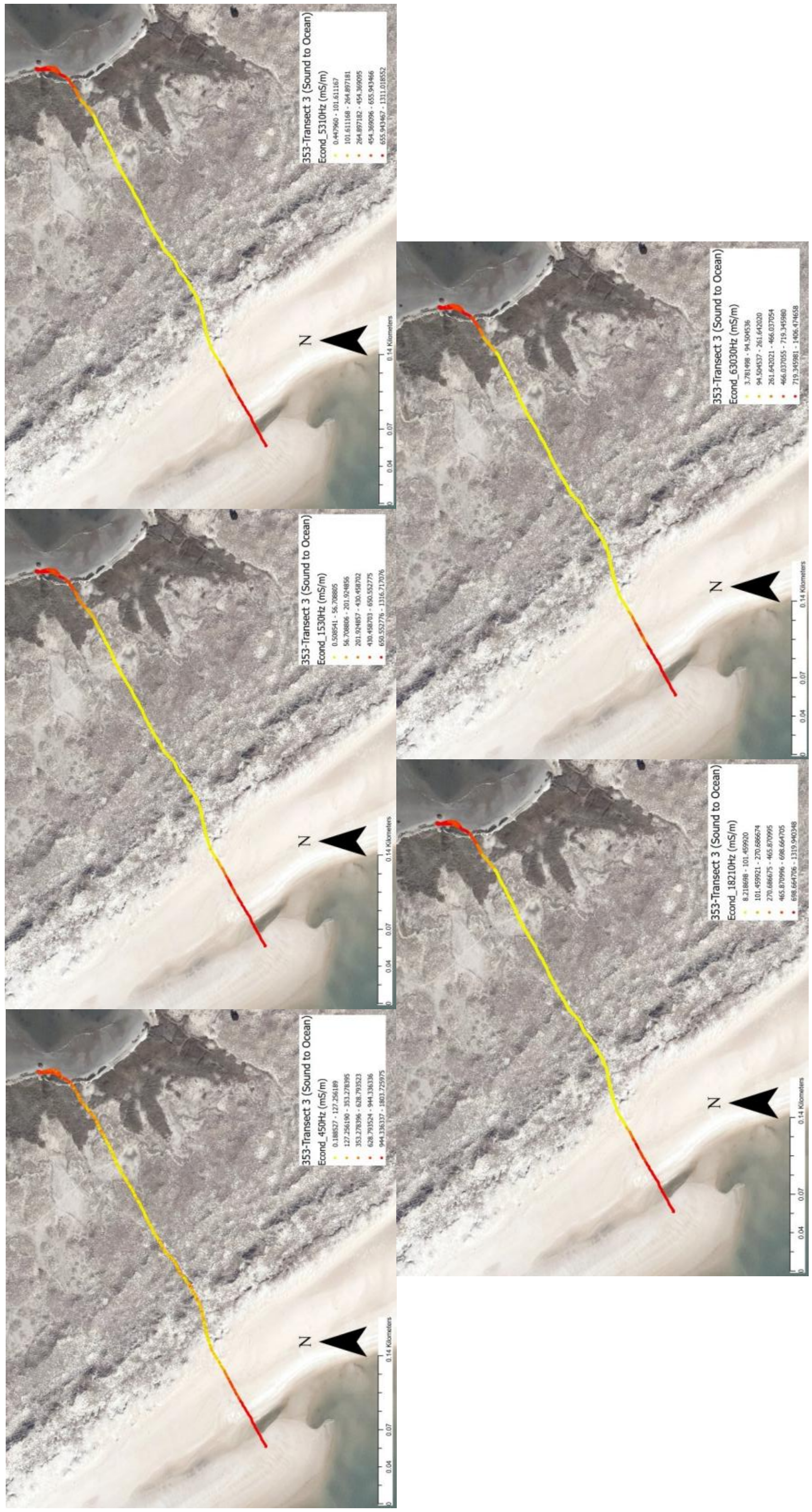

Figure E9). Transect 3 FD-EMI readings during summer.